

INVESTIGATION AND CHARACTERIZATION OF COMPOSITE SILICA
AEROGEL NANOSTRUCTURES OBTAINED VIA MAGNETRON
SPUTTERING

AMANDA CAPACCHIONE

A THESIS SUBMITTED TO THE FACULTY OF GRADUATE STUDIES
IN PARTIAL FULFILMENT OF THE REQUIREMENTS
FOR THE DEGREE OF
MASTER OF APPLIED SCIENCE

GRADUATE PROGRAM IN MECHANICAL ENGINEERING
YORK UNIVERSITY
TORONTO, ONTARIO

DECEMBER 2023

© Amanda Capacchione, 2023

Abstract

This study explores the deposition of Copper (Cu) onto hydrophilic Silica Aerogel (SA) monoliths using magnetron sputtering, with Cu thicknesses of 20 nm, 50 nm, and 100 nm. Leveraging the mesoporous nanostructure of SA, a Cu-sputtered SA nanocomposite was fabricated, creating a non-homogeneous nanocomposite material. Trace amounts of Cu penetrate up to 10 μm into the SA structure, as revealed by SEM-EDS analysis. The resulting nanocomposite, characterized by spectrophotometric examination, exhibited UV scattering, high transmittance, and absorption in the visible range. FTIR spectra revealed reduced transmission in the near-infrared (NIR) and mid-infrared (MIR) regions with increasing Cu thickness. Infrared imaging showed a photothermal effect. The temperatures of samples comprising 100 nm of Cu sputtered onto Silica aerogels reached 94.8°C under solar-simulated irradiation at an intensity of 100 mW/cm². These findings provide fundamental context to an under explored area, laying the groundwork for alternative thin-film deposition techniques like magnetron sputtering deposition for the fabrication of metallic, nanocomposite Silica aerogel supports.

Acknowledgements

I express my gratitude to my co-supervisors, Dr. Marina Freire-Gormaly and Dr. Paul G. O'Brien; and my supervisory committee member, Dr. Thomas Cooper, for granting me the privilege to pursue my Master's Degree. I am fortunate to have studied under their mentorship, providing an environment conducive to the refinement of my mechanical engineering education.

My thanks extend to the lab members and faculty whose invaluable support has been instrumental in the completion of this work. A special appreciation goes to the AM-SET lab members and the MFG lab members, as well as the dedicated technicians who generously shared their time to assist me in understanding complex equipment.

I want to express my profound appreciation to my dearest friends, who stood by my side throughout this journey, offering their unwavering support and care. To my partner and best friend, Kymani, your gentleness, love, and support have been a constant source of strength and joy. Thank you for always making me smile and laugh.

Lastly, I reserve my deepest acknowledgment for my parents, Bruna and Steve, and my brother Bowen. Their continuous, unconditional support and belief in my abilities have been the bedrock of my journey. Thank you for standing by me every step of the way, never doubting my capabilities, and fostering an environment where I could achieve my aspirations.

Table of Contents

Abstract	ii
Acknowledgements	iii
Table of Contents	iv
List of Tables	vii
List of Figures	viii
Abbreviations	xiii
Nomenclature	xiv
1 Introduction	1
1.1 Motivation	2
1.1.1 Immediate Motivation for this Thesis	2
1.2 Literature Review	4
1.2.1 The Application of Current Nanocomposites	4
1.2.2 Nanocomposites Formed via Deposition Techniques	5
1.2.3 PVD Techniques & Sputtering Used on Aerogels	6
1.3 Research Goals and Gaps in Current Literature	8
1.4 Thesis Objectives	9
1.5 Thesis Outline	11
2 Background	12

2.1	Introduction to Aerogels	12
2.1.1	Types of Aerogels	13
2.2	Aerogel Fabrication	13
2.2.1	Supercritical Drying	15
2.2.2	Limitations of Sol-Gel Fabrication Techniques	16
2.3	Physical Vapor Deposition Techniques	18
2.3.1	Sputtering	18
2.3.1.1	Evaporative Sputtering	19
2.3.1.2	Magnetron Sputtering	19
2.3.2	Thin Film Structure	22
2.3.2.1	Parameters Affecting Deposition	23
2.3.2.2	Geometry & Thin Film Growth	24
2.4	Computationally Modelling Aerogel Nanostructure	24
2.4.1	Aerogel Nanostructure	25
2.4.2	RLA and DLCA Modelling	25
2.5	Aerogel Characterization	28
2.5.1	Metal Selection for Deposition	28
2.5.2	Morphological Characterization Techniques	28
2.5.3	Optical Characterization Techniques	29
2.5.4	Thermal Characterization Techniques	31
3	Experimental Methodology	33
3.1	Sputtering and Silica Aerogel Preparation	36
3.2	Morphological Characterization	40
3.3	Spectrophotometric Characterization	41
3.3.1	UV-Visible Spectroscopy	41
3.3.2	Fourier Transform Infrared Spectroscopy	43
3.4	Thermal Imaging Characterization	46
4	Experimental Results	48
4.1	Physical Appearance of Silica Aerogels with Copper Thin Films	48
4.2	Morphological Characterization Results	49
4.2.1	Top-View SEM Results	50
4.2.2	Cross-Sectional SEM Results	53

4.2.3	Energy Dispersive Spectroscopy Results	54
4.3	Spectrophotometric Characterization Results	56
4.3.1	UV-Visible Spectroscopy	57
4.3.1.1	Transmission Results	57
4.3.1.2	Reflection Results	60
4.3.1.3	Absorption Results	62
4.3.2	Fourier Transform Infrared Spectroscopy	64
4.4	Thermal Imaging Results	67
4.4.1	Lateral Imaging Results	70
4.4.2	Thermal Imaging Summary of Results	74
5	Conclusion	75
5.1	Discussion of Results	75
5.1.1	Morphology of Nanocomposite Silica Aerogel Samples	75
5.1.2	Metallic-Coating Thickness & Silica Aerogel Properties	76
5.1.3	Computational Model for Aerogels	77
5.2	Thesis Summary Statement	77
5.3	Future Work	78
	Bibliography	91
	Appendix	92
A	Langevin & Brownian Motion	92
B	Matlab Simulation: Sol-gel Aggregation	94

List of Tables

2.1	The corresponding wavelength values (in nm) with their respective ranges. The spectrum starts at UV wavelengths and moves into far-infrared wavelengths.	31
3.1	List of precision Silica aerogel properties as found from Aerogel Technologies LLC [42].	34
3.2	Categorization of samples listed in each batch (B1, B2, B3, and B4) with their corresponding contents. Each batch contains one bare Silica aerogel (BSA) sample, one BSA with 20 nm, 50 nm, and 100 nm deposited on top (denoted as Cu20@BSA, Cu50@BSA, and Cu100@BSA).	36
3.3	Deposition thickness calculation (nm) given the deposition time (s) and deposition rate (nm/s) from the magnetron sputtering machine.	38
4.1	EDS elemental composition results.	54
4.2	The calculated average maximum direct transmission and hemispherical transmission across each batch for the BSA, Cu20@BSA, Cu50@BSA, and Cu100@BSA samples.	59
4.3	Average deviation (%) between each batch of measurements in the NIR and MIR range. A smaller average deviation between measurements implies experimental reproducibility.	66

List of Figures

1.1	Schematic illustrating experimental outcome, displaying sputtered particles approaching the Silica aerogel matrix. The concept involves applying a thin film on top while maintaining insulative properties on the bottom. This new structure features a top coating that is distinct from the bottom layer, introducing a non-homogeneous composite.	10
2.1	Schematic illustrating the triple point.	15
2.2	SEM images of blisters on the surface of sputter-deposited Cadmium Telluride (CdTe) at a scale of 100 μm and 20 μm , respectively [53].	19
2.3	Schematic of magnetron sputtering process.	21
2.4	Light transmission through a SA. Some light is either absorbed or passes through, labeled as "direct transmittance." The remaining light undergoes redirection at particle-pore interfaces, resulting in multiple scattering events before emerging as "diffuse reflectance" or "diffuse transmittance," depending on the exit surface [86].	30
3.1	Precision Silica aerogel bar, measuring 14 cm in length, 2.5 cm in width, and 1.0 cm in thickness, purchased from Aerogel Technologies LLC [42].	34
3.2	Schematic of cut silica aerogel samples with dimensions of 2.0 cm in length, 2.5 cm in width, and 1.0 cm in thickness. A.) Depicts the cut silica aerogel structure with no Cu deposited, and B.) depicts the cut silica aerogel structure with dimensions outlining the deposited area of Cu, with dimensions of 1.2 cm by 1.2 cm.	35

3.3	Sample batch of the as-prepared Silica aerogel samples with varying thicknesses of Cu deposited on the surface. Here A.) contains 20 nm (Cu20@BSA), B.) 50 nm (Cu50@BSA), and C.) 100 nm (Cu100@BSA) of Cu ascribed to an area of 1.2 cm by 1.2 cm.	35
3.4	A.) Aluminum mask (1.2 cm by 1.2 cm) placed atop Silica aerogel (SA) samples during sputtering and B.) substrate holder with SA samples held in place with Kapton tape and the aluminum masks on top.	38
3.5	Inside of the Amod Angstrom Engineering magnetron sputtering machine with substrate holder mounted in place. The shutters and the magnetrons that encase the Cu target material are displayed. The QCM thickness detector is positioned out of the frame to the left of the working area. . . .	39
3.6	Schematic of the Shimadzu UV-2600 spectrophotometer integrating sphere (ISR-2600 Plus) attachment. The diagram outlines the spectral layout of light transmission, along with indicating SA positions for data acquisition. Position 1 is used for hemispherical transmittance and position 2 is used for relative total reflectance.	42
3.7	Silica aerogel sample placed within the 4.0 cm by 4.0 cm holder, situated inside of the Bruker Vertex 70 machine, used to facilitate direct transmission FTIR measurements.	45
3.8	Experimental setup of Xenon arc lamp. A schematic of the layout is depicted in A.) while B.) represents the physical laboratory setup, including labels.	47
3.9	Lateral positioning of the thermal imaging camera including experimental laboratory setup of the Xenon arc lamp.	47
4.1	Cylindrical Silica aerogel sample (1.5 cm in diameter) displaying internal structural collapse from a droplet of water placed atop its surface.	50
4.2	SEM images of a BSA sample taken at 2.00 kV and varying magnifications. The image seen at (a) is taken at 10,000x magnification with a scale of 10 μm , (b) is taken at 25,000x magnification with a scale of 4 μm , (c) is taken at 50,000x magnification with a scale of 2 μm , and (d) is taken at 100,000x magnification with a scale of 500 nm.	51

4.3	SEM images taken at 2.00 kV. Images seen at (a)–(c) are taken at 10,000x magnification with a scale of 10 μm . Images seen at (d)–(f) are taken at 25,000x magnification with a scale of 4 μm . Images seen at (g)–(i) are taken at 50,000x magnification with a scale of 2 μm . Finally, images seen at (j)–(l) are taken at 100,000x magnification with a scale of 500 nm.	52
4.4	Cross-sectional images of two different Cu@100BSA samples. In (a), the Cu100@BSA sample displays Cu meshed within the silica aerogel matrix. Whereas (b), represents a lateral view of the BSA on the left, and another Cu100@BSA sample on the right–Cu clustering can be seen.	55
4.5	EDS images of Cu100@SA sample at a 5 μm scale. A.) Displays the SEM image that was analyzed, B.) and C.) display colorations of the elemental distribution, green referring to Cu and pink to Si. D.) Represents a line scan of the SEM image seen in A.) (the scale is 20 μm).	56
4.6	Direct percent-transmission (DT) plots of the bare Silica aerogel (BSA), bare Silica aerogel with 20 nm deposited (Cu20@BSA), bare Silica aerogel with 50 nm deposited (Cu50@BSA), and bare Silica aerogel with 20 nm deposited (Cu100@BSA) samples in the UV-Vis-NIR range (220 nm to 1400 nm).	57
4.7	Hemispherical percent-transmission (HT) plots of the bare Silica aerogel (BSA), bare Silica aerogel with 20 nm deposited (Cu20@BSA), bare Silica aerogel with 50 nm deposited (Cu50@BSA), and bare Silica aerogel with 20 nm deposited (Cu100@BSA) samples in the UV-Vis-NIR range (220 nm to 1400 nm).	58
4.8	Comparison of direct and hemispherical percent-transmission plots of the BSA, Cu20@BSA, Cu50@BSA, and Cu100@BSA samples in the UV-Vis-NIR range (220 nm to 1400 nm).	59
4.9	Reflection plots in the UV-Vis-NIR range (220 nm to 1400 nm) of the BSA, Cu20@BSA, Cu50@BSA, and Cu100@BSA samples.	61
4.10	Calculated percent-absorption spectra (1-T-R) in the UV-Vis range (220 nm to 1400 nm) of the BSA, Cu20@BSA, Cu50@BSA, and Cu100@BSA samples.	63

4.11	FTIR direct transmittance spectra containing plots of the BSA, Cu20@BSA, Cu50@BSA, and Cu100@BSA samples across the full wavelength spectra (1000 nm to 25,000 nm), particularly split into the NIR (1000 nm 2500 nm) region, and MIR to FIR regions (2500 to 25000 nm).	64
4.12	Close-up of FTIR direct transmittance spectra containing plots of the BSA, Cu20@BSA, Cu50@BSA, and Cu100@BSA samples in the NIR (1000 nm 2500 nm) and MIR regions (2500 to 7000 nm). Dashed (- -) black lines indicate absorption dips, with the dotted dashed (.-) black lines indicating a transmission band, indicative of water absorption.	65
4.13	Lateral infrared images of BSA sample at 1 minute after the solar simulator is turned on, followed by images taken at five 5-minute intervals from 1 to 26 minutes after the solar simulator was turned on. A schematic of the setup is seen in the top right corner.	68
4.14	Lateral infrared images of a BSA sample, with another BSA placed on, at 1 minute after the solar simulator is turned on, followed by images taken at five 5-minute intervals from 1 to 26 minutes after the solar simulator was turned on. A schematic of the setup is seen in the top right corner.	68
4.15	Lateral infrared images of a Cu100@BSA sample at 1 minute after the solar simulator is turned on, followed by images taken at five 5-minute intervals from 1 to 26 minutes after the solar simulator was turned on. A schematic of the setup is seen in the top right corner.	69
4.16	Lateral infrared images of a BSA@Cu100@BSA sample, at 1 minute after the solar simulator is turned on, followed by images taken at five 5-minute intervals from 1 to 26 minutes after the solar simulator was turned on. A schematic of the setup is seen in the top right corner.	69
4.17	Plots of the BSA, Cu20@BSA, Cu50@BSA, and Cu100@BSA samples recorded temperature versus time of irradiation period. Samples with Cu are placed down with the deposition side facing the solar simulator. Dashed lines represent temperature values that were recorded with a BSA placed on top of the Cu-sputtered sample, and solid lines represent temperatures recorded with no BSA on top.	71

4.18	The temperature profiles with depth are illustrated for bare Silica aerogel (BSA), depicted by the solid line, and BSA@BSA, shown by the dashed line. Panel A.) presents a schematic of BSA@BSA, where a datum reference point establishes that the top of the SA sample is x equal to 0 cm, with the value increasing as one progresses through the depth of the SA, reaching the bottom at x equal to 1 cm.	72
4.19	The temperature profiles with depth, recorded at 15 minutes, are presented for Cu20@BSA, Cu50@BSA, and Cu100@BSA samples, alongside an identical set of measurements for each case with a BSA on top.	73
A.1	3D (a) and 2D (b) DLCA simulation results, which are used to simulate the sol-gel mechanisms of creating a silica aerogel.	93

Abbreviations

ALD	Atomic Layer Deposition
BSA	Bare Silica Aerogel
CVD	Chemical Vapor Deposition
Cu20@BSA	20 nm Cu on Bare Silica Aerogel
Cu50@BSA	50 nm Cu on Bare Silica Aerogel
Cu100@BSA	100 nm Cu on Bare Silica Aerogel
DT	Direct Transmission
FTIR	Fourier Transform Infrared
HT	Hemispherical Transmission
IS	Integrating Sphere
MS	Magnetron Sputtering
NP	Nanoparticle
PVD	Physical Vapor Deposition
SEM	Scanning Electron Microscopy
TR	Total Reflection
TEOS	Tetraethyl Orthosilicate
TMOS	Tetramethyl Orthosilicate
UV-Vis	Ultra-Violet Visible
UV	Ultra-Violet

Nomenclature

Chemical Formulae

Al₂O₃ Aluminum Oxide (Alumina)

Ar Argon

CO₂ Carbon Dioxide

Cu Copper

Cu₂O Copper (I) Oxide

CuO Copper (II) Oxide

Au Gold

Pt Platinum

SiO₂ Silicon Dioxide

Ag Silver

TiO₂ Titanium Dioxide

W Tungsten

Xe Xenon

ZnO Zinc Oxide

Chapter 1

Introduction

Nanocomposite materials are characterized as multi-component materials consisting of multiple distinct (non-gaseous) phase domains. In these materials, at least one phase domain functions as a continuous phase, and at least one of the phases exhibits at least one dimension on the order of nanometers. Porous nanocomposite materials, on the other hand, incorporate voids or interconnected pores, resulting in an augmented surface area. These materials feature a porous matrix infused with nanoscale additives, showcasing distinctive architectural characteristics defined by a lightweight yet durable scaffold dictated by the internal geometry of their structure. Understanding the internal structure of porous materials is crucial for optimizing their properties, developing applications tailored to specific needs, and ultimately creating new composite materials that utilize the porous network. The nanoscale structure can offer tailored properties, such as low density and thermal conductivity, high surface area, and controlled permeability [1]. For instance, a porous matrix (bulk material) with carbon nanotubes (nanoscale additive) reinforced into the nanostructure constitutes a nanocomposite material [2].

Silica aerogels possess an exceptionally porous matrix, rendering them highly promising for the development of innovative nanocomposite structures. Despite serving as an unconven-

tional support, these aerogels provide an ideal environment. Renowned for their exceptional characteristics, bare Silica aerogels exhibit an exceptionally high porosity of 90% to 99%, with most of their pore sizes residing in the mesopore regime, ranging between 2 nm to 50 nm, as well as low thermal conductivity, low density, and high surface area [3]. While silica aerogels have a highly porous and open-cell structure, their geometry is uniquely not typically characterized by elongated or significantly extended dimensions. They are often considered materials with a three-dimensional nanoporous network, where the structure is more uniform and interconnected throughout their volume.

Silica aerogels, with the incorporation of dispersed metal nanoparticles (NPs), graphene fibers, or carbon nanotubes within the silica matrix, are a type of nanocomposite. The incorporation of metal NPs, for instance, into the Silica aerogel matrix can enhance certain characteristics, such as catalytic activity, electrical conductivity, or magnetic properties, depending on the type of metal nanoparticles used in the Silica aerogel matrix [4, 5]. These nanocomposite aerogels are useful as catalysts, electrodes for fuel cells and batteries [6, 7], vibration and acoustical damping devices, semiconductor materials [8], and desiccant materials [5]. Recently, researchers have tailored aerogel materials to demonstrate the photothermal effect for applications such as interfacial water evaporation and sterilization [9–11]. The versatility of nanocomposites arises from their ability to manipulate material properties at the nanoscale, paving the way for innovations across a diverse set of industries.

1.1 Motivation

1.1.1 Immediate Motivation for this Thesis

This research is primarily motivated by the aspiration to create a nanocomposite silica aerogel. The approach involves employing physical vapor deposition (PVD) techniques, specifically magnetron sputtering, to apply thin films of metallic material onto the surface of

silica aerogel supports, and characterize the newly created nanostructure. Currently, the use of PVD methods for creating composite aerogel nanostructures remains an underexplored area in the existing literature. The remarkable porosity of silica aerogel material can provide an unconventional substrate for thin film deposition. Making use of the aerogel's inherent nanoporosity enables the deposited material to potentially permeate into the silica aerogel matrix, integrating into the nanoporous structure. This approach harnesses the nanoporous characteristics of Silica aerogels to craft a distinctive type of nanocomposite aerogel, where the upper surface of the aerogel material is different from that on the bottom. As a result, a non-homogenous nanocomposite silica aerogel material can be achieved.

In general, this study aims to provide an understanding of the physical phenomena associated with sputtering Copper (Cu) onto aerogel structures. The central research inquiries revolve around investigating morphological changes in the Cu layer resulting from sputtering. Additionally, the study aims to determine the depth to which the sputtering process effectively permeates these porous materials, and it explores methods to control the sputtering process on Cu. The fundamental research aspect of this study gains significance due to the scarcity of existing literature analyzing the impact of PVD techniques specifically on Cu within Silica aerogel nanostructures. This study is also motivated by the compelling drive to explore alternative thin-film deposition techniques like magnetron sputtering deposition for composite aerogel fabrication. The magnetron sputtering deposition method not only enables variable control over thin film thickness within the aerogel pores but also ensures the purity of the sputtered material. Employing thin film deposition methods such as magnetron sputtering, not only offers precise control over material thickness but also creates a conducive environment for pristine fabrication.

In addition, traditional methods for fabricating composite aerogels through the sol-gel route necessitate meticulous attention to detail to ensure thorough precursor integration before drying [12]. Addressing the limitations of sol-gel synthesis for composite aerogel fabrication is a pivotal focus for advancing the versatility of composite aerogels in a wide range of

industries. It has been identified that some of the underlying drawbacks of this method include complex chemistry regarding the compatibility of the precursors and interfacial interactions. It is especially difficult when suspending nanoparticles within the gelation matrix since it is prone to agglomeration and losing control over the nanoparticle size and distribution [4]. Hence, research into the analysis of deposited materials within the aerogel's nanostructure holds critical importance for both academia and industry professionals, aiming to enhance and expand the performance and applications of nanocomposite aerogel materials.

1.2 Literature Review

1.2.1 The Application of Current Nanocomposites

Aerogel nanocomposite materials represent a class of materials characterized by the integration of nanoparticles into a matrix, creating unique properties unattainable in traditional materials. For instance, carbon nanotube composites exhibit remarkable strength and electrical conductivity, making them valuable in applications like lightweight structural materials and conductive films. Graphene-based nanocomposites boast exceptional mechanical, thermal, and electrical properties, finding utility in fields ranging from electronics to energy storage [13, 14]. Nanocomposites play a crucial role in advancing water and air purification technologies due to their unique properties at the nanoscale. For water purification, nanocomposite materials like graphene oxide or carbon nanotube-based composites are employed in filtration membranes [13, 15–17]. These materials offer high surface areas, mechanical strength, and chemical stability, enhancing the removal efficiency of contaminants, including heavy metals and organic pollutants [18]. Additionally, silver nanoparticle-loaded composites exhibit antimicrobial properties, aiding in the disinfection of water [19]. In air purification, nanocomposites are utilized in filters and adsorbents to capture particulate matter and harmful gases [20]. Metal-organic frameworks (MOFs) and zeolite-based nanocomposites

are noteworthy examples, offering large surface areas and tunable pore sizes for effective gas adsorption [21–23]. Titanium dioxide NPs are incorporated into air purification systems for their photocatalytic properties, which can degrade volatile organic compounds and microbial contaminants when exposed to light [13, 14, 24]. The porous framework inherent in nanocomposite materials offers a distinctive avenue for further exploration and innovation.

Aerogels can be manufactured in various forms, including beads, cylinders, and monoliths, expanding their application potential. Among the spectrum of inorganic aerogels, Silica aerogels have received considerable attention owing to their well-established sol-gel chemistry [4]. However, the introduction of metallic precursors in the sol-gel route can potentially yield undesirable pore properties, impacting the polymerization pathways and overall structure [25]. Despite being a straightforward method that allows for precise control over loading and composition, the incorporation of preformed NPs may lead to challenges such as aggregation and sedimentation, hindering the achievement of a homogeneous dispersion within the gels [25, 26]. Zhi et al.’s [26] recent work underscores the critical need for the development of novel synthesis methods. As mentioned earlier, the conventional aerogel synthesis processes face challenges stemming from intricate procedures and chemistry, resulting in time-consuming production. This section delves into the existing literature that utilizes various deposition techniques that will provide context to this thesis work. Furthermore, this section seeks to explore relatively current developments in this field of work, including potential avenues of applications such as photocatalysis, driven by the use of composite aerogels.

1.2.2 Nanocomposites Formed via Deposition Techniques

The literature encompasses various deposition techniques employed to coat or fill porous solids, including methods such as electrodeposition, spin-coating, electron beam deposition, and atomic layer deposition (ALD). Physical vapor deposition (PVD) techniques, like sputtering, have received relatively little to no attention in comparison. The aforementioned

techniques, aside from sputtering, are a form of chemical vapor deposition (CVD). Various advantages are associated with CVD, like excellent homogeneity or favorable thickness accuracy [27, 28]. There have been only a few reports that have discussed employing sputtering as a method of depositing material into highly porous solids [29]. Depositing material into porous solids is a topic that has garnered popularity over time. Yuan et al. [30] coated Alumina (Al_2O_3) aerogels with Zinc Oxide (ZnO) for 6, 12, or 25 cycles via atomic layer deposition. It was observed that the porosity of the aerogel samples decreased, implying that ZnO began filling the pores. This study further states that the penetration of ZnO surpassed several layers of the material from preferential sputtering. Similarly, Bakos et al. [31] reports a “blockage” of micropores and mesopores as a result of ALD of ZnO in Carbon aerogel samples after 60 cycles. It is inferred that deposited material penetrates the substrate surface. While ALD can be utilized for depositing thin films, thicknesses of up to 100 nm and beyond will often require significantly more time to execute and are challenging to control precisely [27]. Additionally, ALD may pose limitations in terms of controlling pore size, as the initial deposition cycles can lead to the clogging of the surface layer of the aerogel matrix, hindering further penetration into the nanostructure. These factors collectively contribute to the complexity and constraints associated with employing ALD for composite aerogel fabrication. Nonetheless, the available literature on ALD and other deposition techniques for composite aerogels still remains limited.

1.2.3 PVD Techniques & Sputtering Used on Aerogels

Typically, the deposition of NPs onto an aerogel substrate occurs unintentionally, often as a byproduct of unrelated processes. For instance, sputtering Platinum (Pt) to mitigate charging in scanning electron microscopy (SEM) imaging. This incidental occurrence is seldom the primary focus of analysis and is not deliberately pursued for the purpose of studying the resulting interactions or effects. A study performed by Park et al. [29] utilizes DC magnetron sputtering to fabricate highly porous pure ZnO films. However, their study

is concerned with the growth of porous ZnO films, rather than the penetration depth of ZnO in the porous solid. Insights from two notable studies, specifically those conducted by Kim et al. [19] and the other from Juhasz et al. [32] shed light on the structural modifications induced by using PVD techniques to sputter material onto Silica aerogels.

The latter study mentions that ion-bombardment during sputtering could affect the aerogel structures. Juhasz et al. [32] proved that gold sputtering changes the native morphologies of several different types of Silica-based aerogels. Furthermore, they go on to say that even a thin, 5 nm gold layer modifies the morphology of the aerogel nanostructure. Anything larger than that, and the initial pristine network within the Silica aerogel begins to disappear. Juhasz et al. [32] describe the Au coating to appear "globular," as during the second round of sputtering the Au particles become considerably larger due to nucleation. Here, nucleation marks the initial condensation of atoms or molecules on a substrate, forming small nuclei. Clustering follows, involving the growth of these nuclei into larger groups, while agglomeration sees the merging of clusters into larger, interconnected structures. In the former study, Kim et al. [19] found nanogaps that formed within the deposited metallic film. In their study, they deposited 30 nm and 60 nm of Ag onto Silica-based aerogel substrates via electron beam evaporative processing. Through SEM imaging, they found that beneath the Ag thin film, sputtered Pt penetrated into the Silica aerogel matrix, but did not conclude the exact depth of the Pt.

The nanoscale surface roughness inherent in aerogels significantly influences the deposition of thin films on their surfaces, presenting both advantages and challenges. The rough and irregular surface enhances the adherence of thin films by providing increased surface area and multiple anchor points, promoting better mechanical bonding [33]. This characteristic is advantageous in applications where enhanced adhesion is desired, contributing to the photothermal effect [10]. However, achieving uniform film coverage becomes challenging due to variations in surface irregularities, leading to thickness discrepancies across the aerogel. Despite this challenge, researchers have harnessed these features to tailor aerogel

composites for specific applications, such as TiO₂-Carbon hybrid aerogels [34]. These engineered aerogels exhibit increased radiative absorption capacities, proving effective in applications like interfacial water evaporation and sterilization. Their versatility extends to pollution remediation, by facilitating the necessary chemical transformations that aid in removing various contaminants like dyes, oils, solvents, heavy metals, and radioactive elements. Li et al. [35] successfully facilitated the removal of silver ions from water using polydiaminonaphthalene (PDAN) polymer aerogel samples. Additionally, aerogels used in catalysis experiments show promise in mitigating harmful aerosols and purifying gases in the atmosphere [25].

1.3 Research Goals and Gaps in Current Literature

The primary goal of this work is to produce nanocomposite metallic-Silica aerogel samples using magnetron sputtering—a physical vapor deposition (PVD) technique. Normally, the sol-gel process is used to form nanocomposite Silica aerogels by embedding nanoparticles within the synthesis process. However, this research aims to avoid such a process. Instead, the approach involves applying a thin layer of metallic material by using magnetron sputtering. This unconventional method aims to create a new nanocomposite material, combining silica aerogel supports, fabricating traditionally through sol-gel synthesis with deposited metallic material through PVD.

Consequently, the current research gap centers on the limited understanding of the nanocomposite structure formed when metal is sputtered onto the Silica aerogel surface. Key unknowns include the Silica aerogel structure’s resulting morphology, the thin film’s characteristics, and the depth to which the metal penetrates the porous structure. Addressing these uncertainties is essential for characterizing the optical or thermal properties of the novel nanocomposite architecture. The review of existing literature reveals that only minimal amounts of metallic nanoparticles are typically deposited onto Silica aerogel surfaces. This

work seeks to bridge this gap by depositing tens, if not hundreds, of nanometers of metallic thin film onto the surface of Silica aerogel substrates. Thus, the question this thesis aims to address is the extent to which sputtering can impact the optical and morphological properties of a highly porous material such as a Silica aerogel.

1.4 Thesis Objectives

This thesis delineates a systematic exploration with three distinct objectives, collectively aimed at advancing our understanding and capabilities in the field of aerogel research. Positioned as a fundamental and exploratory study, the deposition of thin metallic films onto porous substrates like Silica aerogels represents a novel approach. The schematic in Figure 1.1 visualizes the anticipated outcome, depicting sputtered particles interacting with the Silica aerogel matrix. The innovative concept involves the application of a distinct top coating while preserving insulative properties on the bottom, creating a non-homogeneous nanocomposite. This approach allows for the exploration of diverse outcomes without pre-defined boundaries. Measurements throughout the study will be interpreted as they emerge, devoid of specific expectations. These objectives collectively align with the overarching aim of deepening our comprehension of Silica aerogels and their versatile potential. The anticipated outcomes are expected to not only contribute to existing knowledge but also offer practical insights for optimizing composite aerogel materials across various applications.

1.) **Investigate the morphology of metal-sputtered Silica aerogel samples**

The first objective of this study is to examine the morphological intricacies of nanocomposite materials comprised of thin metal films sputtered onto Silica aerogels. By employing a series of characterization techniques, this study seeks to elucidate the nanostructural properties and surface characteristics of these materials. This objective serves as a crucial foundation, providing insights into the fundamental structure of aerogels. Here, this can uncover whether the deposited metallic film causes any pore-clogging at the surface, or if the material

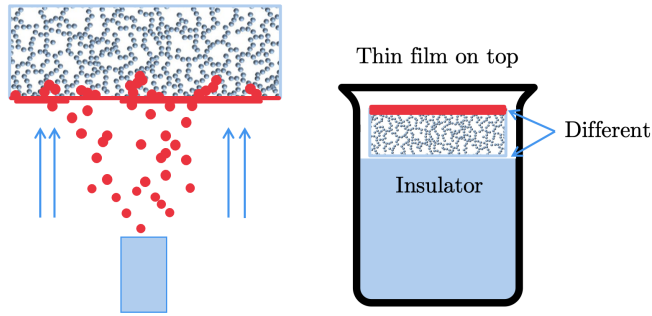


Figure 1.1: Schematic illustrating experimental outcome, displaying sputtered particles approaching the Silica aerogel matrix. The concept involves applying a thin film on top while maintaining insulative properties on the bottom. This new structure features a top coating that is distinct from the bottom layer, introducing a non-homogeneous composite.

penetrates the Silica aerogel nanostructure.

2.) Examine the metallic coating thickness on Silica aerogel properties

The second objective of this research is to investigate the influence of varying the thickness of metallic coatings applied to Silica aerogels. Specifically, this thesis aims to assess how alterations in coating thickness affect the transmissive, reflective, and photothermal properties of these aerogels. This analysis is instrumental in understanding the interplay between structural modifications and optical-thermal performance, furthering the practical applicability of Silica aerogels in various fields.

3.) Establish a foundational computational model for aerogels

The third objective encompasses the development of a rudimentary yet fundamental computational model for aerogels. This model integrates critical parameters, including the fractal dimension and aerogel properties, to lay the groundwork for future, more intricate simulations. By doing so, this study aims to provide researchers with a tool to facilitate accurate representation and prediction of aerogel behaviors, thereby supporting innovative computational applications in the future.

1.5 Thesis Outline

Chapter 1 conducts an examination of current literature on porous nanocomposite materials, existing nanocomposite aerogel structures, and physical vapor deposition (PVD) techniques used in the creation of nanocomposite aerogels. This is followed by the current gaps in the literature and the thesis objectives.

Chapter 2 introduces Silica aerogels (SA) and their diverse compositions as a distinct class of materials. The emphasis is on their exceptional properties and potential applications. The section explores traditional methods for fabricating aerogels and then investigates PVD techniques, such as magnetron sputtering, as a promising avenue for creating nanocomposite aerogel materials. Furthermore, an examination of the SA nanostructure, along with an overview of characterization techniques for SAs is discussed.

Chapter 3 outlines the experimental methodology utilized in the production and analyses of the new nanocomposite SAs. It details the methodology for scanning electron microscopy (SEM) for morphological analysis, UV-visible (UV-Vis) spectroscopy and Fourier transform infrared (FTIR) spectroscopy for spectrophotometric assessment, and thermal imaging to capture the photothermal behavior in SAs containing deposited metallic thin films.

Chapter 4 delivers the results related to each characterization method. Within this chapter, discussions and detailed records of each characterization method, including SEM, UV-Vis spectroscopy, FTIR spectroscopy, and photothermal measurements, are presented and analyzed.

Finally, Chapter 5 provides a summary of the thesis work and offers insights into potential future endeavors in this field.

Chapter 2

Background

2.1 Introduction to Aerogels

In 1931, an American chemical engineer, Dr. Samuel Stephens Kistler published an article in *Nature*, titled "*Coherent Expanded Aerogels and Jellies*" [36] in which he details the development of the first gel-like solid structure. Dr. Kistler was the first to invent the aerogel by effectively removing the liquid from the solid structure. Aerogels are recognized as the least dense solid materials globally and are renowned for their exceptional characteristics. These encompass a remarkably high specific surface area, low thermal conductivity, and their ultra-low density. Aerogel materials can attain densities as minimal as 0.16 mg/cm^3 [37], exhibit surface areas exceeding $1000 \text{ m}^2/\text{g}$ [37], and demonstrate thermal conductivity as low as approximately $20 \text{ mW/m}\cdot\text{K}$ [38]. Kistler achieved this breakthrough by replacing the liquid component in a gel through a thorough washing process. By substituting water with easily evaporable ethanol, the gel's liquid phase, typically an aqueous solution, was effectively exchanged. The crucial step involved using an autoclave for supercritical drying, facilitating the removal of the alcohol solution and leaving behind only the silicon dioxide material. This innovative approach allowed for the elimination of the liquid content while preserving the solid structure of the gel.

2.1.1 Types of Aerogels

Aerogels can be broadly classified into three main categories, although they share a common technical definition as open-celled, mesoporous (pores ranging from 2 to 50 nm in diameter), solid foam with interconnected porous nanostructures and a material that is 90-99% air by volume [39]. They can be categorized into 1) inorganic, 2) organic, and 3) composite aerogels. Inorganic aerogels consist of oxide materials like silicon dioxide (SiO_2) or titanium dioxide (TiO_2). On the other hand, organic aerogels, like resorcinol-formaldehyde aerogels, are composed of organic polymers or carbon-based compounds. Organic aerogels are known for their high surface area, which makes them useful for applications in supercapacitors, oil spill cleanup, and even as lightweight materials for advanced composites [40]. Composite aerogels are advanced materials formed by combining aerogels with other substances, such as polymers or nanoparticles, to enhance or tailor their properties for specific applications. For example, silica aerogels can be reinforced with polymer matrices to create flexible and mechanically robust composite aerogels. This thesis will solely focus on the use of inorganic aerogels, such as Silicon Dioxide (SiO_2) aerogels.

2.2 Aerogel Fabrication

Sol-gel synthesis is the go-to fabrication method for all types of aerogels, including composite aerogels. This method is widely regarded as the conventional choice due to its simplicity and widespread usage. The procedure entails the transformation of monomers into a colloidal solution (sol), which serves as the precursor for forming an interconnected network, known as a gel. While the sol-gel method stands as the primary approach for aerogel production, other techniques like emulsion, self-assembly, and additive manufacturing, including 3D printing, have gained recognition for crafting various aerogel types, including inorganic oxide aerogels, metallic aerogels, and composite aerogels (in no particular order) [4, 41]. This work,

however, does not center on the synthesis of Silica aerogels or any aerogels. Experimental samples for this study are procured externally from Aerogel Technologies LLC [42], meaning that the aerogels utilized in this research are not fabricated in-house.

To produce an aerogel, the initial step involves creating a hydrogel, characterized as a biphasic material. The establishment of the aerogel network consists of two crucial stages: precursor hydrolysis and the condensation of primary nanoparticles. Hydrolysis can be acid or base-catalyzed. Acid-catalyzed hydrolysis employs a strong acid, like hydrochloric acid, to facilitate the hydrolysis of silicon alkoxides in the precursor solution. In contrast, base-catalyzed hydrolysis uses a base, such as ammonia or sodium hydroxide. The precursor materials such as TMOS (tetramethyl orthosilicate) or TEOS (tetraethyl orthosilicate), undergo hydrolysis and polymerization processes, leading to the formation of a gel network [43]. In the initial phase of the sol-gel process for creating a Silica aerogel, precursor molecules facilitate the creation of bonds between siloxane and silicon atoms through a polymerization mechanism. This results in the formation of dispersed solid colloidal Silica particles or linear oligomers [6]. Subsequently, in the second stage, these elementary units interconnect within the solvent medium. The solvent aids in the ongoing polymerization of the sol into a gel until a three-dimensional open network structure, until a gel is eventually established. This phase is commonly referred to as the gelation process, and the transition from a liquid to a solid state is termed the sol-gel transition.

It is emphasized throughout the literature that one of the main disadvantages found with the sol-gel method is the lack of control over the rate of hydrolysis and condensation, which can result in less-than-ideal results for aerogel creation, especially for composite aerogels. Silica aerogels with metal NPs suspended in the gel, often require an aging treatment post-drying. The aging step involves mechanically reinforcing the solid skeleton of the Silica gel. Aging, as a result, only contributes to the already lengthy process which is the sol-gel process. Typically, sol-gel processes for composite aerogel fabrication can take anywhere between days to weeks at a time depending on the type of material and equipment used, as well as

the sample size, temperature, and pH [6, 44]. Following the hydrogel creation, supercritical drying is applied to eliminate the solvent, ultimately yielding a porous aerogel structure.

2.2.1 Supercritical Drying

Drying constitutes a critical stage in aerogel production, as it is during this phase that capillary stresses emerge when gas-liquid menisci form at the pore boundaries while the liquid is removed [40, 44]. Silica aerogels are commonly dried using supercritical drying, bypassing the critical point, seen in Figure 2.1. The three-dimensional structure of the gel network formed by hydrolysis and condensation needs to be preserved after drying. The most important step is to remove the liquid component from the network without substantially shrinking it. Hence, the key to maintaining pore wall recession is to ensure that liquid is not removed sporadically. Supercritical drying is the most common technique used to remove the liquid from the hydrogel while minimizing the capillary forces acting on the pore walls [5, 45].

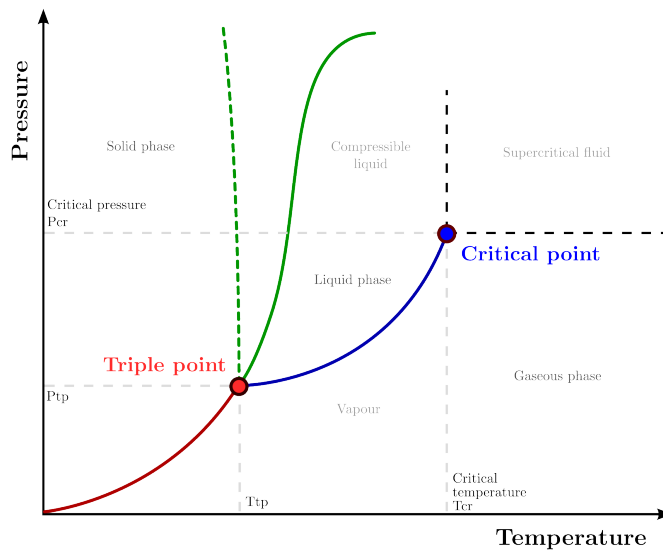


Figure 2.1: Schematic illustrating the triple point.

Alwin and Shajan [5] clarify that the porous network structure is often preserved during

supercritical drying, as the capillary forces tend to be less influential [44]. Specifically, the use of supercritical CO₂ drying is more prevalent, given the relatively lower critical point of liquid CO₂. Supercritical CO₂ is used to displace the solvent in the aerogel, and then the supercritical CO₂ is removed selectively as a gas later by modifying temperature pressure accordingly. However, despite supercritical drying having the ability to minimize shrinkage, the process is time-consuming, hazardous, and challenging to precisely control. Typically, industries, research facilities, or companies with high-end, costly equipment tend to favor supercritical drying.

2.2.2 Limitations of Sol-Gel Fabrication Techniques

Within the wide spectrum of fabrication techniques, inorganic aerogels, particularly Silica aerogels, have predominantly been produced using the sol-gel method. This can be attributed to the extensive research and standardization of sol-gel chemistry, which has contributed to its widespread adoption in the field of aerogel production [25]. However, the sol-gel method utilized in the production of mono- or bi-metallic embedded NP aerogel supports is accompanied by several limitations, which may potentially be addressed through the adoption of alternative fabrication methods. Despite the standardized sol-gel recipes, the sol-gel reaction remains inherently unstable due to its catalytic nature [46]. According to Pajonk et al. [45], despite the use of autoclave and supercritical drying, aerogels are susceptible to shrinkage and cracking, a phenomenon that can be exacerbated in the presence of suspended NPs, which typically originate from micro-cracks. The presence of NPs within the solvent can impede permeability and may interact with the delicate pore walls during formation, leading to their collapse. The sol-gel process is recognized for its time-consuming nature, particularly when attempting to incorporate NPs into the solution, leading to a host of additional challenges and intricacies. Traditionally, composite aerogel structures are formed within the gel itself which can increase gelation time and affect the drying or aging process. Dagan and Tomkiewicz [24] claim that gelling can take between 1 minute to

4 days depending on the materials used. Wen et al. [47] claim that it took their metallic NP solution 2 days to realize into a hydrogel. Furthermore, they found that aerogel supports containing gold (Au) NPs that were pre-aggregated extended gelation time to 1 week. Sol-gel reactions are generally followed by a thermal treatment which will differ depending on the precursor molecules and overall chemical composition of the final product. For example, in a study by Ferreira-Neto et al. [12], the Silica wet gels were soaked in a precursor solution for 24 hours, which were subsequently kept at 80°C for an additional 24 hours in an oven. After several wash-throughs of ethanol and acetone, the now-prepared wet gels were ready for supercritical drying at 1500 psi and 50°C. Subsequently, the monolithic aerogel samples were then heat treated up to 1000°C for 2 hours with increasing temperature at a rate of 10°C/min.

A pertinent example from the work of Shao et al. [14], focusing on composite carbon TiO₂ samples, highlights the time-consuming aspects of the sol-gel process. The samples were subjected to a water bath at 70°C for 5 days to form the wet gel structure. Subsequently, they underwent supercritical drying in an autoclave at 240°C and 6 MPa for 1 hour. Depressurization was conducted at a rate of 0.1 MPa/min until atmospheric pressure was achieved, after which the samples were cooled to room temperature. Lastly, the dried aerogels were carbonized at 800°C for 3 hours to achieve the composite material [48]. All in all, the process lasted one week to complete. Metallic aerogels are those that when created via sol-gel synthesis, require another level of complexity and attention to detail. There involves a careful selection of the size, shape, and composition of presynthesized nanostructures and the controlling of the gelation process is essential for the self-assembly method, which can produce aerogels with high crystallinity and controllable building-block dimensions. A study by Lázár et al. [49] highlights the challenging nature of synthesizing Silica aerogels with Au NPs, attributed to the difficulties in controlling the process consistently. They reported that the variability in solvents used and the composition of gases during the aging and drying stages led to non-reproducible results. It quickly becomes apparent that fabricating

composite aerogel structures is time-consuming, complex in nature, and not entirely a reproducible (standardized) procedure.

2.3 Physical Vapor Deposition Techniques

Thin film technology has demonstrated its utility in augmenting material properties and, in certain cases, conferring entirely new attributes to materials. Within this context, a thin film refers to a layer of material ranging from fractions of a nanometer to several micrometers in thickness [50]. As the deposition time progresses, the thin film undergoes growth, wherein an increase in the number of deposited particles contributes to the expansion of the film, primarily driven by particle clustering or nucleation. A particle is identified as a cluster when it comprises 2 to 10^n atoms, where n can reach up to 7 [51]. These clusters serve as the fundamental building blocks in thin films, by facilitating the growth mechanism described earlier. The appropriateness of this thickness range will be determined based on the user's application and specific design requirements. To obtain a thin film, the material must be deposited into a substrate. This can be accomplished by utilizing physical vapor deposition (PVD) techniques.

2.3.1 Sputtering

Within the realm of PVD techniques, there are two main categories, namely evaporative sputtering and magnetron sputtering. In general, sputtering is a thin film deposition method that utilizes an electric field to bombard a substrate with an ionized gas (usually Argon), such that clusters of atoms are ejected from the substrate. Magnetron sputtering is utilized in this thesis work, however, a brief background is provided regarding evaporative sputtering to provide context.

2.3.1.1 Evaporative Sputtering

Evaporative sputtering, also referred to as DC sputtering, is a PVD technique where the process takes place in a vacuum chamber (typically within the range of 10^{-6} to 10^{-4} Torr) containing a cathode (the target material) and a grounded anode. Argon gas is introduced into the chamber, and a DC voltage is applied between the cathode and the anode, creating an electric field that ionizes the argon gas, forming a plasma. The positively charged argon ions are accelerated toward the cathode, leading to sputtering, where atoms are dislodged from the target. These atoms then condense onto a substrate, producing a thin film. In evaporative sputtering methods, like electron beam evaporation, the heating circuit often becomes hotter than the source pellet, resulting in resistively heated evaporation. This phenomenon may lead to the formation of blisters on the substrate surface, as depicted in Figure 2.2. Blistering in thin film deposition is undesirable as it creates voids or gas-filled pockets beneath the film surface, weakening adhesion to the substrate and reducing long-term reliability due to an increased susceptibility to delamination and other forms of degradation [52].

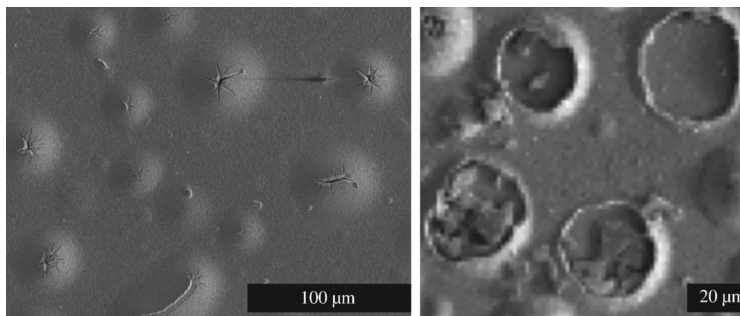


Figure 2.2: SEM images of blisters on the surface of sputter-deposited Cadmium Telluride (CdTe) at a scale of $100\ \mu\text{m}$ and $20\ \mu\text{m}$, respectively [53].

2.3.1.2 Magnetron Sputtering

While evaporative sputtering tends to produce dense and well-adhered films, magnetron sputtering offers better control over film properties and higher deposition rates. Evaporative

sputtering relies on a DC voltage for ionization, whereas magnetron sputtering employs a magnetic field to increase ionization efficiency. Magnetron sputtering often results in better target utilization, meaning a higher percentage of the target material is utilized in the deposition process [54]. Under the influence of magnetic fields, electrons experience altered trajectories due to the Lorentz force, causing them to be confined near the target [55]. This confinement persists until the electrons lose most of their energy through collisions with the argon atoms in the chamber, achieving thermalization. The incorporation of magnetic enhancement involves maintaining pressures between 1 mTorr to 10 mTorr and applying high voltage values to the cathode, ranging from 400 V to 600 V [55–57]. Magnetron sputtering devices utilize electromagnets or permanent magnets to generate strong magnetic fields, carefully oriented parallel to the target surface to ensure an optimal deposition rate by enhancing particle entrapment [55–57]. This principle is commonly referred to as the "Hall effect," where electron movement is influenced by a drift force $\bar{\mathbf{E}} \times \bar{\mathbf{B}}$, also acting on secondary electrons in the ionization vicinity.

The fabrication process using magnetron sputtering involves several key steps conducted within an evacuated chamber, effectively creating a vacuum space to minimize the partial pressures of any background gases or contaminants. This can effectively be seen in Figure 2.3. To initiate the process, a sputtering gas, typically an inert gas like argon or xenon, is introduced into the chamber via a pressure control system. Subsequently, plasma is generated by applying a high voltage between the cathode and the anode. The cathode, situated behind the target, and the anode, connected to the chamber as the electrical ground, play critical roles in the ionization process. The sputtering gas's electrons are accelerated away from the cathode and collide with nearby atoms of the sputtering gas, facilitating ionization. Positively charged sputtering gas atoms are then accelerated towards the negatively charged cathode, leading to high-energy collisions with the target's surface. These collisions can cause atoms at the target's surface to be ejected into the vacuum space, with sufficient kinetic energy to reach the surface of the substrate. This intricate interplay

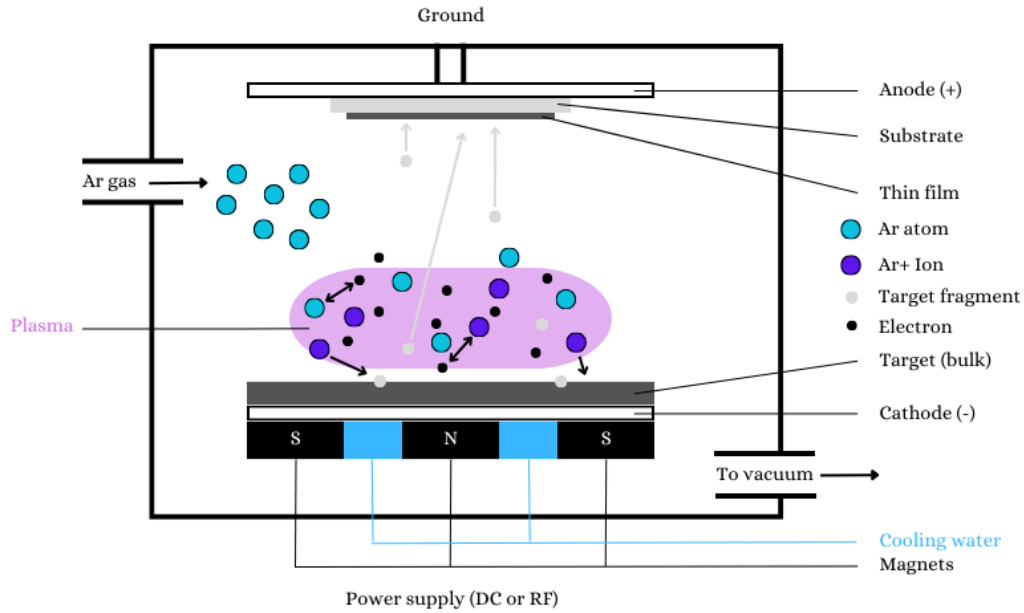


Figure 2.3: Schematic of magnetron sputtering process.

between the sputtering gas, the cathode, and the target surface forms the basis of the magnetron sputtering process. As particles of the target material collide with the substrate surface, a cluster begins to form, stemming from a nucleus or nucleation center [51].

Magnetron sputtering machines are highly regarded for their adaptability, attracting users with the ability to adjust several parameters. These adjustments include controlling chamber pressure and temperature, regulating power requirements, and selecting the rotation and shape of the substrate holder, whether spherical or planar. Additionally, users can determine the amount of material to be deposited on the substrate. One of the main advantages of magnetron sputter deposition is its avoidance of the need to melt and evaporate the source material, providing distinct benefits over other physical vapor deposition (PVD) technologies. This method allows for the deposition of almost all materials, regardless of their melting temperatures. Furthermore, sources can be scaled and positioned anywhere in the chamber, catering to the specific requirements of the substrate and coating. Magnetron sputtering enables the deposition of films composed of alloys and compounds while maintaining a

composition similar to that of the source material.

There are two primary types of magnetron sputtering, distinguished by their power sources: direct current (DC) and radio frequency (RF) magnetron sputtering. While RF magnetron sputtering employs AC current, DC magnetron sputtering, as the name suggests, utilizes DC current. However, RF magnetron sputtering generally exhibits slower deposition rates and higher power costs, rendering it more suitable for smaller substrates. On the other hand, DC magnetron sputtering is associated with increased deposition rates due to the ionization of the working gas, making it more conducive to larger substrate sizes. DC magnetron sputtering is typically used for electrically conductive targets, while RF magnetron sputtering is more commonly employed for thick, electrically non-conductive targets.

2.3.2 Thin Film Structure

In materials science, the representation of polycrystalline microstructures in metallic alloys often relies on the use of Voronoi tessellations. These tessellations are utilized in island growth to approximate the growth rate of individual islands [58]. This approach is particularly valuable, especially when simulating processes like thin film growth on a substrate surface [58]. While several studies have predicted thin film growth on different substrates, minimal attention has been given to aerogels. Barna and Adamik [59] reported a general model of film growth, encompassing nucleation, island growth, coalescence, and the formation of polycrystalline islands. The development of metallic nanoparticles involves stages such as nucleation, diffusion, and growth, regulated by kinetic phenomena. The characteristics and segregation extent of nanoparticles are influenced by the kinetics of nucleation and growth, making the method and conditions of nanoparticle generation crucial factors.

In magnetron sputtering, issues related to the quality of deposition in target materials can arise due to a phenomenon known as arcing. Arcs, characterized as low-voltage, high-current discharges, have the potential to cause damage to the surface [60, 61]. The

high-energy particles sputtered from the target onto the substrate can result in physical damage, commonly known as "pinholes" [62]. This type of damage is especially problematic for soft organic layers at the surface, as it can significantly impact the overall performance of the device [63]. Increasing the voltage supply amount poses the risk of contaminating the substrate [56]. Other topological irregularities, contaminations, and general defects such as nodular, pinholes, pores, and coating discontinuities on the substrate surface can be described as growth defects [53, 64]. Ion-bombardment during sputtering can also have a significant effect on the structures of aerogels [65]. During the initial stages of deposition, a discontinuous layer of atoms, appearing as small "islands," will nucleate rather than a continuous film developing [66]. This is sometimes referred to as "island pooling."

2.3.2.1 Parameters Affecting Deposition

Ideally, the goal of sputtering technology is to aptly deposit target material uniformly on a substrate. There are important parameters that play a necessary role in the growth of thin film thickness, from chamber pressure and substrate temperature, substrate-to-target distance, to the collisions between each atom on a molecular scale (mean free path). In the event of analyzing the sputtering process, researchers are usually concerned with what occurs on the target and the substrate, after all, sputtering performance is highly characterized by a sputter yield, which is the ratio of the number of particles emitted to the number of projectiles. Sputter yield is by far one of the most important areas of analysis, as it encompasses a wide range of parameters. Bouazza and Settaouti [67] state that sputter yield changes with the energy and nature of the incident ion (i.e., specie of material), the orientation of its trajectory relative to the target, the nature and the crystallographic state of the target, its temperature, the magnetic field and the pressure.

2.3.2.2 Geometry & Thin Film Growth

Wang et al. [68] further describe that film thickness uniformity is affected by the substrate geometry, the distance between the substrate and the target, as well as the motion between the substrate and the target. The pressure in the sputtering chamber can range from 0.1 Pa to 10 Pa and affects both the deposition rate and the uniformity of the deposition, a similar claim can be made for the power applied to the cathode [69–71]. Furthermore, by largely increasing power to the cathode, there results in an increase in temperature as well, causing sputtered atoms to stick to the target material, slightly reducing the deposition rate [60]. The substrate-to-target distance can impact how deep particles penetrate the material, as well as how well the particles deposit on the surface. When a particle undergoes sputtering, there are three main pathways it endures depending on the mean free path and the particles' energy. Particles with high energy will deposit onto the substrate, while particles with near thermal energy have a lower probability of deposition and will continue to collide with other high-energy particles. Finally, thermalized particles are unlikely to be deposited onto the substrate, as they are a result of experiencing numerous collisions until they reach equilibrium with the surroundings and blend in with the background gas [54, 66, 72].

2.4 Computationally Modelling Aerogel Nanostructure

It is well-established that simulation software for sputtering enjoys extensive communities offering updated tutorials and procedures. In contrast, the same cannot be said for sol-gel synthesis, a process that, if comprehensively modeled, could prove to be an immensely powerful tool in the study of aerogels. The third objective of this thesis aimed to develop a computational silica aerogel model that could serve as a tool for studying the gelation process, porosity, and its interaction with particle transport phenomena. While this objective

was not fully realized, the thesis provides a baseline model and a literature review detailing the silica aerogel nanostructure, along with methods for its modeling.

2.4.1 Aerogel Nanostructure

Ghafar et al. [40] conducted an extensive study of the porosity of composite polysaccharide aerogels and highlighted the challenges associated with characterizing the intricate 3D structure of these materials, including the connectivity of pores and the distribution of pore sizes. The nanoporous structures of aerogels, while captivating, also present one of their most intricate aspects. It is widely acknowledged that the early stages of the sol-gel reaction exhibit unstable non-linear oscillations in the size of the sol particles, attributed to instabilities in the chemical process resulting from the catalytic nature of the reaction, where water acts as both a reactant and a product [46]. These unstable structures exhibit a fractal nature, formed through a reaction-limited aggregation (RLA) mechanism, particularly during the initial phase of the sol-gel reaction, characterized by high concentrations of reactants. Mandelbrot's concept of fractals, used to describe complex shapes with non-integer (fractal) dimensionality, aptly applies to these intricate and irregular aerogel structures. The fractal network of aerogels, often resembling a random "jungle gym" arrangement, represents a branched-polymer-like structure that emerges during the sol-gel synthesis process [73].

2.4.2 RLA and DLCA Modelling

Schaefer and Keefer [73] investigated the fractal geometry of silica aerogels and deemed that low-density aerogel has purely mass-fractal characteristics, as illustrated in Equation 2.1. This section serves as a modeling methodology for objective three, as stated in Chapter 1, section 1.4.

$$M(R) \sim R^D \tag{2.1}$$

Where D is the fractal dimension, M is the mass, and R is the length. Objects that obey this equation are called mass or volume fractals. Examples of objects doing such include polymers, diffusion-limited aggregates, and percolation clusters. Schaefer and Keefer [73] also classified aerogel porosity as a branched-polymer-like structure, which is identical to a colloidal aggregate grown in a solution precursor. They conclude that the observed fractal behavior appears inconsistent at varying length scales and aggregation solutions. As a result, they could not definitively categorize the aerogel structure as entirely fractal. However, they claim that, during polymerization, the chainlike branched polymer backbone of the aerogel forms fractally rather than the overall pore space. The uniform nature of the pore space within the aerogel implies that any snapshot taken from various points within the nanostructure is likely to display considerable resemblance, indicating the uniform and consistent characteristics of the aerogel's pore network. The fractal exponent, D , which is used to determine the dimension of a fractal object, can be reduced to values less than one. This suggests that the structure being described exhibits a form of self-similarity but with a decreasing complexity as you zoom in [46, 74–76].

In more recent studies, the fractality debate of aerogel structure has grown. A study published in 2021 by Abdusalamov et al. [77], over a decade since Schaefer and Keefer's publication, has extensively reviewed fractal behavior in aerogels. It is known that aerogels exhibit random network connectivity, however, they do not boast a perfect (fully) connected network structure. In the realm of porous media, aerogels are classified as open-celled foam models. Abdusalamov et al. [77] further explain that, on a macro-scale at certain lengths, aerogels are known to have mass distributions that are fractal. Using computational modeling, we can create a fractal network that forms by mimicking the sol-gel process. Such a process can be modeled by means of the aggregation mechanism. While several aggregation algorithms exist and can model this clustering process, it is generally found that diffusion-limited cluster aggregation (DLCA) modeling best agrees with the scattering data of silica aerogels.

Initially, the silica particles in the sol formation are primarily influenced by the reaction-limited aggregation (RLA) process, leading to structures with fractal exponents less than 1, akin to Cantor's sets, owing to the inherent instability of these formations. This value implies that the structure is becoming more and more space-filling, eventually approaching a set of mathematical points without any discernible structure. Cantor's set, for example, is a classic example of a fractal structure that exhibits self-similarity and has a fractal dimension that is a non-integer. As the aggregates grow and attain sizes comparable to or greater than the wavelength of light, the fractal exponent approaches 1.7, signifying a shift toward the diffusion-limited aggregation (DLA) process. In diffusion-limited cluster aggregation (DLCA) modeling, Brownian motion is used to model the random walks of particles that lead to the formation of clusters and in turn, form the aggregates. This phenomenon follows a similar process of clustering observed in the sol-gel process.

A basic MATLAB script was developed and can be found in Appendix (A). This type of modeling utilizes the Langevin equation (Equation A.1) which is a part of a set of stochastic differential equations (SDE). Moving from left to right, this process begins by setting the number of seed points and walker particles. Here, the red points represent seed particles, and the blue are walker particles. Walker particles are those that can move freely and will circumvent branching, eventually supporting the conglomeration of clusters with other walker and seed particles. Their interactions will soon develop into aggregates, and so on. In general, various literature is in favor of the fractality of aerogels. Some additional studies provide further support for this idea including publications from Babu et al. [78], Woignier et al. [79], Pajonk et al. [45], Hermann and Elsner [80].

2.5 Aerogel Characterization

2.5.1 Metal Selection for Deposition

Copper (Cu) is chosen over commonly used Carbon or Carbon-composite aerogels due to its cost-effectiveness, ready availability, large surface area, and electrically conductive properties [81–83]. However, at the nanoscale, Cu exhibits distinctive behaviors that deviate from its typical bulk characteristics, with the traditional reddish-brown color becoming less apparent [84]. This color deviation, shared with other noble metals like Gold (Au) and Silver (Ag), suggests that the nanoscale introduces unique optical properties. Plasmonic NPs, known for supporting localized surface plasmon resonances (SPR), are intriguing for manipulating light at the nanoscale. While Cu’s plasmonic properties are not as extensively explored as those Ag and Au, its selection offers an opportunity to explore relatively uncharted territory.

2.5.2 Morphological Characterization Techniques

Comprehending the nanostructures of SA samples is crucial, although they typically exhibit consistency from one sample to another, leveraging imaging techniques like scanning electron microscopy (SEM) and transmission electron microscopy (TEM) enables a more detailed examination of the internal and external nanostructure. Hence, this study utilizes SEM imaging techniques for this purpose. A study conducted by Kim et al. [19] presented an insightful examination of imaging Silica aerogels (SA) coated with thin layers of Ag NPs at 30 nm and 60 nm. The thin film growth of Ag was fabricated by placing the SA samples in an electron beam (E-beam) evaporation machine. The researchers obtained cross-sections using a focused ion-beam (FIB) SEM system. To prevent damage to the thin film during FIB-SEM measurements, a thin protective layer of Pt was deposited onto the Ag layers via E-beam evaporation. Subsequent cross-sectional imaging disclosed nanogaps and silica chain networks in the Ag films. Additionally, the Pt NPs were observed to penetrate through the

nanogaps and into the nanopores of the SA beneath the metal film, leading to a reduction in the porosity of the SA substrate. This crucial insight should be taken into account during the imaging process, as this may drastically mask (or even alter) the intrinsic porous properties of the SA [85].

2.5.3 Optical Characterization Techniques

Optical analysis is critical in evaluating and enhancing the performance of monolithic and composite SAs. By depositing thin metal films onto the aerogel structure, it is possible to impart additional optical functionalities or properties to the aerogel. In general, spectrophotometry serves as a fundamental analytical tool for characterizing the optical properties of aerogels. Employing a spectrophotometer, the transmittance of the aerogel samples is determined by measuring the fraction of the incident light beam that passes through the sample, controlled by wavelength, from a light source and dispersion grating. The interplay of the sample with the incident light results in a combination of light absorption, reflection, and scattering phenomena, ultimately influencing the amount of light transmitted through the sample.

Recall that scattering is a phenomenon in which light deviates from its straight-line path due to interactions with particles or irregularities in a medium, this is depicted in Figure 2.4. SAs being nanoporous materials with a highly dispersed structure, coupled with a low refractive index (close to that of air) exhibit Rayleigh scattering, especially in the UV range [19]. Rayleigh scattering is more pronounced at shorter wavelengths and occurs when the size of the scattering particles is much smaller than the wavelength of light, and its intensity is inversely proportional to the wavelength, as seen in Equation 2.2.

$$I \propto \frac{1}{\lambda^4} \tag{2.2}$$

Subsequently, a light receiver positioned on the opposing side of the aerogel captures the

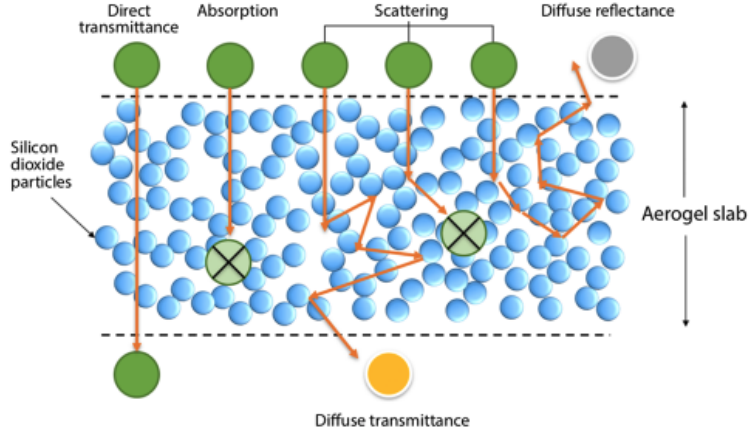


Figure 2.4: Light transmission through a SA. Some light is either absorbed or passes through, labeled as "direct transmittance." The remaining light undergoes redirection at particle-pore interfaces, resulting in multiple scattering events before emerging as "diffuse reflectance" or "diffuse transmittance," depending on the exit surface [86].

transmitted light. This data is juxtaposed against a reference dataset obtained under identical conditions, albeit without the presence of the aerogel sample, allowing for precise baseline measurement comparisons. Mathematically, this can be observed in Equation 2.3, as transmittance at varying wavelengths (τ_λ) is calculated as the ratio of transmitted light intensity (I_t) to the incident light intensity (I_0), expressed as percent transmittance.

$$\tau_\lambda = \frac{I_t}{I_0} \quad (2.3)$$

UV-Vis and FTIR spectrophotometers cover specific wavelength (λ) ranges, as delineated in Table 2.1. The UV range analyzed in this work spans from approximately 200 nm to 400 nm, while the visible range stretches from 400 nm up to 750 nm. Following the visible range, the near-infrared (NIR) and mid-infrared (MIR) regions are introduced. The NIR range extends from around 750 nm to 2500 nm, while the MIR range ranges from 2500 nm to 50,000 nm. Subsequently, wavelengths beyond the MIR region are classified as far-infrared (FIR) and can reach values of 1 mm. FTIR spectroscopy is effective in identifying the

Table 2.1: The corresponding wavelength values (in nm) with their respective ranges. The spectrum starts at UV wavelengths and moves into far-infrared wavelengths.

Range	Wavelength (nm)
UV-Vis Range	> 200 – 400
Visible	400 – 750
NIR Range	750 – 2500
MIR Range	2500 – 50,000
FIR Range	>50,000

chemical composition of sample analysis. Furthermore, FTIR provides information about the transparency, reflectance, absorption, and emissivity of the samples, particularly in longer wavelength ranges.

2.5.4 Thermal Characterization Techniques

The black-grey color of aggregated Cu at the nanoscale, as well as the chemical composition, suggests that thin Cu films could provide a reliable and potentially equally effective alternative to creating carbon-based composite aerogels. This alternative can replace existing ones that might be costly or challenging to procure, especially in applications such as solar-driven water heating or devices for water and air purification [87–91]. These aerogels, such as the previously mentioned ones, can effectively absorb and convert light energy into heat. The unique porous structure of aerogels will trap light, generating plasmons and enhancing plasmon resonance, thereby amplifying the photothermal effect [19]. This property enables them to generate localized heating when exposed to light, facilitating the photothermal effect. Plasmon resonance is a collective oscillation of electrons in a material that occurs when it interacts with the light of a specific wavelength [30]. This resonance phenomenon can enhance the light absorption and scattering properties of the material. In plasmonic materials like noble metal nanoparticles (e.g., Au or Ag), plasmon resonance is harnessed to enhance the photothermal effect. When these NPs are exposed to light matching their plasmon resonance frequency (e.g., Cu at 500 to 600 nm), they efficiently absorb and convert electromagnetic energy into heat [19, 30]. Using low-refractive index materials such as SAs as

substrates can intensify the electric field at the sensing area, thereby influencing the overall efficiency. This phenomenon can offer certain advantages as well as drawbacks. The uneven clustering on the SA surface or within the pores may correspond to the formation of "hot spots," or clustering, where measurements taken at slightly different positions yield varying results [19, 92]. These hot spots can generate additional heat and may also contribute to reduced optical transparency.

Chapter 3

Experimental Methodology

This chapter describes the experimental methodology used in the preparation of Silica aerogel (SA) samples, which utilizes magnetron sputtering as a means to deposit thin Cu films atop their surface. It provides an analysis of the samples' morphological characteristics, employing scanning electron microscopy (SEM) to unveil the intricate nanostructure. UV-Visible spectroscopy and Fourier transform infrared (FTIR) spectroscopy are carried out to reveal the optical properties of the SA samples with metallic thin films deposited atop their surface. The SA bars were stored in their designated boxes, within ambient conditions, following their shipment and were removed before sputtering. In addition, this chapter provides the methods used to conduct thermal imaging experiments on the SA samples, with and without Cu atop their surfaces, to analyze the photothermal effect. Several hydrophilic precision Silica aerogel bars, measuring 14 cm in length, 2.5 cm in width, and 1 cm in thickness, were procured from Aerogel Technologies LLC for use in all of the experimental investigations (Figure 3.1) [42]. The properties of these SA samples are provided in Table 3.1.

The 1.0 cm thick SA bars were sectioned using a thin, stainless steel razor blade, into 2.0 cm by 2.5 cm squares, with any excess material reserved for backup purposes. The SAs were

Table 3.1: List of precision Silica aerogel properties as found from Aerogel Technologies LLC [42].

Property	Value
Density (bulk)	0.09 g/cm ³
Mean pore diameter	20 nm
Thermal conductivity (in air)	0.015 - 0.020 W/m·K
Porosity	>80%
Refractive index	1.0 – 1.05

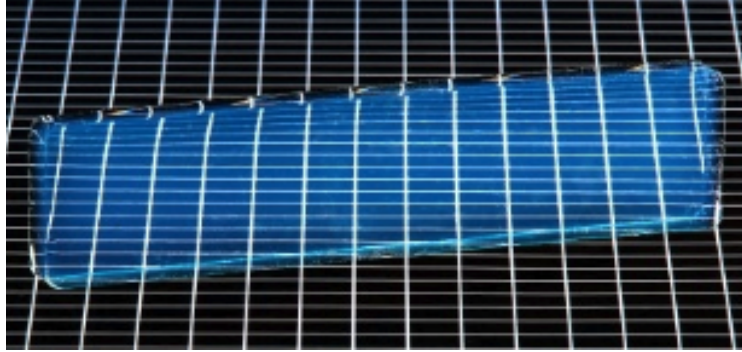


Figure 3.1: Precision Silica aerogel bar, measuring 14 cm in length, 2.5 cm in width, and 1.0 cm in thickness, purchased from Aerogel Technologies LLC [42].

scored on each surface at the desired length, and then carefully snapped, yielding a usable sample. Figure 3.2 depicts a schematic representing the aerogel dimensions. Each bar was capable of yielding up to seven pieces, provided the integrity of the samples was maintained during the cutting procedure. Three samples were allocated for UV-Visible spectroscopy (UV-Vis) experiments, three for Fourier transform infrared (FTIR) spectroscopy experiments, three for photothermal experiments, and several smaller pieces (0.7 cm thick, 1 cm in length, 1 cm in width) for scanning electron microscopy (SEM). Additional samples were procured to account for any potential compromise to the silica aerogel structure during the preparation or experimental phases.

Therefore, in total, 12 hydrophilic SA samples were prepared with thin metallic films deposited on their surface. Specifically, the chosen thicknesses included 20 nm, 50 nm, and 100 nm, all uniformly distributed within a confined 1.2 cm by 1.2 cm area on the surface of

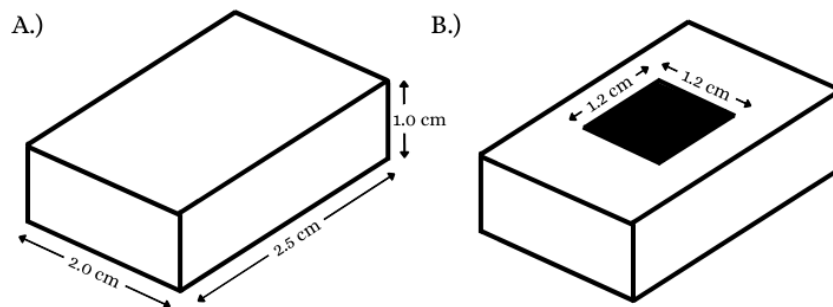


Figure 3.2: Schematic of cut silica aerogel samples with dimensions of 2.0 cm in length, 2.5 cm in width, and 1.0 cm in thickness. A.) Depicts the cut silica aerogel structure with no Cu deposited, and B.) depicts the cut silica aerogel structure with dimensions outlining the deposited area of Cu, with dimensions of 1.2 cm by 1.2 cm.

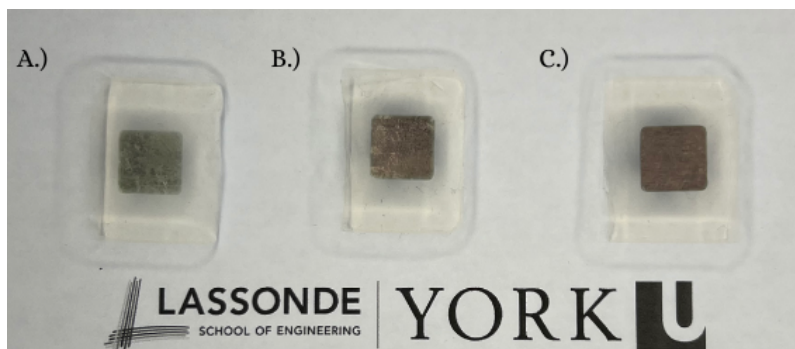


Figure 3.3: Sample batch of the as-prepared Silica aerogel samples with varying thicknesses of Cu deposited on the surface. Here A.) contains 20 nm (Cu20@BSA), B.) 50 nm (Cu50@BSA), and C.) 100 nm (Cu100@BSA) of Cu ascribed to an area of 1.2 cm by 1.2 cm.

the SA sample, as seen in Figure 3.2B. Table 3.2 displays the sample organization, where a total of 4 distinct "batches" were compiled. Each batch comprises 3 Silica aerogel samples, with each batch containing one 20 nm sample, one 50 nm sample, and one 100 nm sample. Therefore, a standard naming convention is assigned as Cu20@BSA, Cu50@BSA, and Cu100@BSA. This notation signifies the quantity of Cu deposited onto a bare Silica aerogel (BSA). Out of these four batches, three were exclusively designated for optical measurements, while the remaining fourth batch was allocated for photothermal experiments. Thus, these batches were identified as batch 1 (B1), batch 2 (B2), batch 3 (B3), and batch 4 (B4). The as-prepared silica aerogels with varying thicknesses of Cu layers can be seen in Figure 3.3.

Table 3.2: Categorization of samples listed in each batch (B1, B2, B3, and B4) with their corresponding contents. Each batch contains one bare Silica aerogel (BSA) sample, one BSA with 20 nm, 50 nm, and 100 nm deposited on top (denoted as Cu20@BSA, Cu50@BSA, and Cu100@BSA).

Batch 1 (B1)	Batch 2 (B2)	Batch 3 (B3)	Batch 4 (B4)
BSA x1	BSA x1	BSA x1	BSA x1
Cu20@BSA x1	Cu20@BSA x1	Cu20@BSA x1	Cu20@BSA x1
Cu50@BSA x1	Cu50@BSA x1	Cu50@BSA x1	Cu50@BSA x1
Cu100@BSA x1	Cu100@BSA x1	Cu100@BSA x1	Cu100@BSA x1
4 samples	4 samples	4 samples	4 samples

In addition, several silica aerogels without Cu deposited on the surface were included in the study as well.

3.1 Sputtering and Silica Aerogel Preparation

Once samples were properly cut and organized into their respective categories for characterization, they were brought into the York Microfabrication (YMF) laboratory to be sputtered. The Angstrom Engineering Amod magnetron sputtering machine is employed to apply three Cu thicknesses onto the SA samples, specifically at 20 nm, 50 nm, and 100 nm. The magnetron sputtering machine, equipped with both RF and DC settings for the sputtering process, features automated shutters that facilitate the initiation and termination of the deposition process. Additionally, the magnetron sputtering machine incorporates Aeres, Angstrom’s advanced process control software, offering an interface to configure specific functionalities tailored to the experimental objectives. The incorporation of shutters is crucial for calibrating the deposition rate, a standard procedure in the operation of the magnetron sputtering machine. These shutters effectively block debris, contaminants, and any previously deposited metal that may re-emerge during each process. This would cause the quartz crystal microbalance (QCM) to inaccurately detect the deposited thickness of the material. Once the pre-conditions within the sputtering machine are successfully executed,

the deposition process is initiated. This initiation is contingent upon ensuring that all user-defined settings are met. Only then, the shutters are retracted when the operator initiates the deposition onto the substrate or by a pre-set recipe. However, the placement of the shutters, positioned less than 1 cm from the substrate holder, posed a challenge for the proper mounting of the 1 cm thick SA samples.

In response, a customized process code was collaboratively devised with Angstrom technicians to prevent the shutters from obstructing the substrate holder and damaging the SA samples. While this adjustment allowed for the samples to be mounted to the sample holder, and not interfere with the shutters, it posed a challenge to the accurate measurement of the deposition process, necessitating the manual verification of deposition thicknesses using the designated parameters of the deposition process. The magnetron sputtering machine involves a series of preconditions that must be satisfied before initiating the deposition process. At this stage, it is determined whether the shutters should be closed or opened. An additional precondition step was introduced to prevent inadvertent shutter closure. Throughout each step in the process code (e.g., precondition steps, deposition steps, and post-condition steps), the machine continuously times these steps, taking into account the chamber settings at each stage. For instance, during the deposition step, the graphical user interface (GUI) of the magnetron sputtering machine displays parameters such as the average deposition rate, chamber temperature and pressure, voltage, and current. By analyzing the time taken to deposit each thickness and its corresponding average deposition rate, it can be manually verified whether the intended amount of material is being deposited onto the substrate. In essence, this serves as an estimation of the thin film thickness, with the obtained values considered approximate. For instance, when targeting a deposition thickness of 100 nm, the system's automatically recorded deposition time of 6 minutes and 47 seconds, coupled with an approximate deposition rate of 0.246 nm/s, yielded a calculated thickness of nearly 100 nm, confirming the achieved deposition thickness. Table 3.3 provides the recorded values during the sputtering process for each scenario of thickness.

Table 3.3: Deposition thickness calculation (nm) given the deposition time (s) and deposition rate (nm/s) from the magnetron sputtering machine.

Scenario	Deposition time [s]	Deposition Rate [nm/s]	Deposition Thickness [nm]
1	98	0.204	20
2	215	0.233	50
3	407	0.246	100

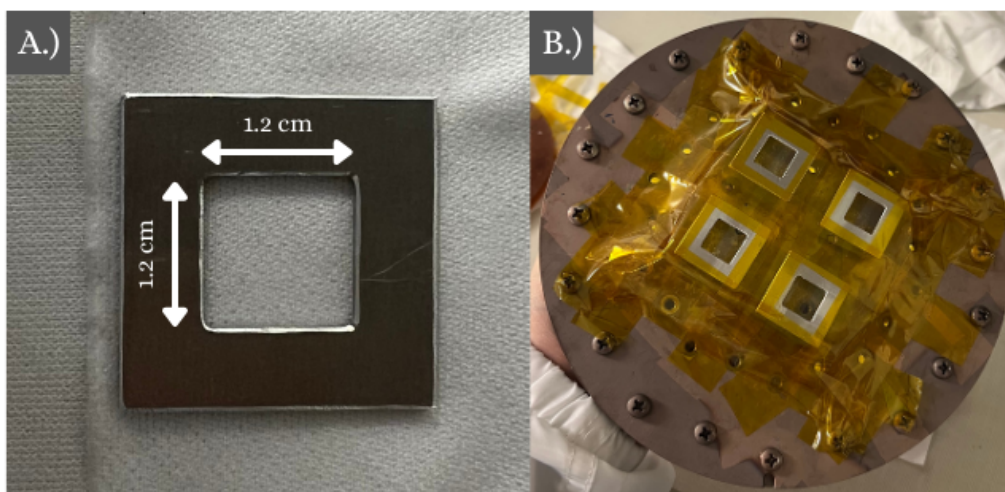


Figure 3.4: A.) Aluminum mask (1.2 cm by 1.2 cm) placed atop Silica aerogel (SA) samples during sputtering and B.) substrate holder with SA samples held in place with Kapton tape and the aluminum masks on top.

The initial step of the sputtering process involves the introduction of Argon gas into the chamber. Here, Argon gas is used as the sputter gas which facilitates ionization. Once the chamber has been vented, the SA samples are mounted onto the planar circular substrate holder, requiring the removal of the substrate holder from the chamber for this purpose. To ensure precise and accurate sputtering within the specified area (which is a square with an edge length of 1.2 cm) custom aluminum masks were machined at York University's machine shop, as illustrated in Figure 3.4A. Using a 1.2 cm x 1.2 cm square mask provided enough sample area to characterize the samples accordingly. These aluminum masks were carefully positioned atop the aerogels and gently secured in place using Kapton tape, as seen in Figure 3.4B. Subsequently, the substrate holder is reinserted into the chamber, initiating the pump-down procedure, as seen in Figure 3.5.

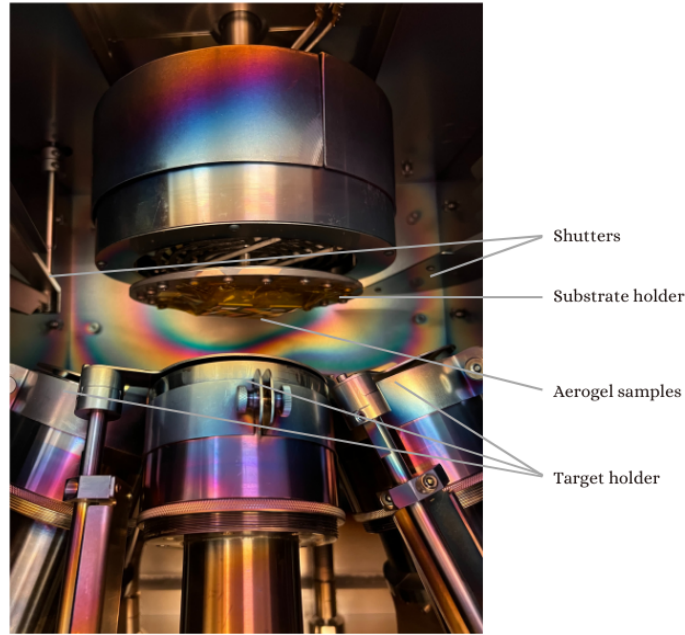


Figure 3.5: Inside of the Amod Angstrom Engineering magnetron sputtering machine with substrate holder mounted in place. The shutters and the magnetrons that encase the Cu target material are displayed. The QCM thickness detector is positioned out of the frame to the left of the working area.

The loaded process code, also known as the recipe, comprises a series of predefined steps, including the power percentage, the desired material thickness, and the type of material. Throughout the process, the power is consistently set at $\approx 33.3\%$ (200 W). The shutters remain open during the entire process. Four samples are taped to the substrate holder, for each deposition, resulting in three consecutive runs (4 samples for 20 nm, 4 for 50 nm, and 4 for 100 nm). This setup can be seen in Figure 3.4B, on the substrate holder. The QCM device (pictured off-screen to the left of the shutters in Figure 3.5) measures the thickness of Cu deposited once the deposition process commences. However, since the shutters remain open, any residual material left on the SAs before the measurement is also included in the thickness measurement, if present. The copper target is acquired with a purity of 99.995%, measuring 10 cm in diameter and 0.635 cm in thickness. To prevent obstructions to the aerogel surfaces, the substrate holder stage is elevated, and the

shutters are displaced. Following the calibration based on the user-defined settings, including the desired Cu thickness, the stage descends, allowing a substrate-to-target distance of approximately 10 cm (with the top aerogel surface positioned 10 cm from the magnetrons). Achieving a chamber pressure of 5×10^{-5} Torr is the final prerequisite for the system, as the Angstrom Amod sputtering system operates within the pressure range of 5×10^{-5} Torr to 10×10^{-5} Torr, with the upper limit set at 10×10^{-5} Torr. Lower pressures are favorable for material deposition. Simultaneously, the pressure steadily decreases to the specified set point during the process. As the chamber reaches its desired set point values, the substrate holder rotates at 10 RPM and remains at 22.2°C during the entire process until the deposition process is complete.

3.2 Morphological Characterization

Scanning electron equipment from both the Advanced Light and Electron Microscopy Facility at York University (Thermofisher Quanta 3D) and SEM instruments from the Canadian Centre for Electron Microscopy (CCEM) at McMaster University are employed to conduct imaging, as well as energy dispersive x-ray spectrometry (EDS) to analyze the nanostructure of the Cu-sputtered Silica aerogel samples, along with the bare Silica aerogel samples. Accordingly, both top-view and cross-sectional images are to be acquired. The Silica aerogels were prepared with 20 nm, 50 nm, and 100 nm of deposited Cu, with several extra 100 nm Cu samples exclusively designated for cross-sectional imaging. On the other hand, all samples, including the 20 nm and 50 nm variants, will undergo analysis through the top-view imaging method. The bare aerogel samples will only be subjected to top-view imaging techniques to provide insights into the underlying Silica matrix constituting the aerogel structure.

Top-view images were completed at McMaster University under 2.0 kV of energy, while cross-sectional images were taken at York University under varying energy settings. For

imaging purposes, smaller samples (thicknesses ≤ 0.7 cm) are prepared, varying in length from 1.0 cm to 1.2 cm. These samples undergo the same sputtering procedure as the other SA samples. However, the SA samples designated for top-view imaging have their geometry left untouched, while those intended for cross-sectional imaging are sectioned using a thin, stainless steel razor blade. The SEM samples set aside for cross-sectional imaging intentionally lack a masking device during sputtering, resulting in the entire surface area being covered in Cu. Subsequently, these Cu-coated samples are sectioned upon arrival at the SEM facility, and the freshly exposed Silica face is adorned with a thin layer of Platinum (Pt), approximately 5 nm in thickness. This additional Pt layer serves the dual purpose of minimizing charging effects and facilitating detailed imaging [93, 94]. Furthermore, it ensures that the Silica component of the aerogels retains a degree of conductivity during the imaging process. The samples were secured onto the pin mount with conductive carbon glue or conductive liquid silver paint to mitigate any form of shaking and charging.

3.3 Spectrophotometric Characterization

3.3.1 UV-Visible Spectroscopy

The direct transmittance (DT), hemispherical transmittance (HT), and total relative reflection (diffuse and specular light) of the bare and Cu-sputtered SAs were characterized through spectrophotometric measurements utilizing the Shimadzu UV-2600 Spectrophotometer. The UV-Vis instrument was used to take measurements across the spectral range of 220 nm up to 1400 nm. The procedure covered all wavelengths from the UV region to the NIR region. Hemispherical transmittance and total relative reflection were measured using an integrating sphere (Shimadzu ISR-2600 Plus integrating sphere attachment) with its integrated external detector, as can be seen in Figure 3.6. The inclusion of the integrating sphere (IS) attachment facilitated the extension into the NIR region. Direct transmittance, on the other hand, was measured without an integrating sphere, utilizing the detector

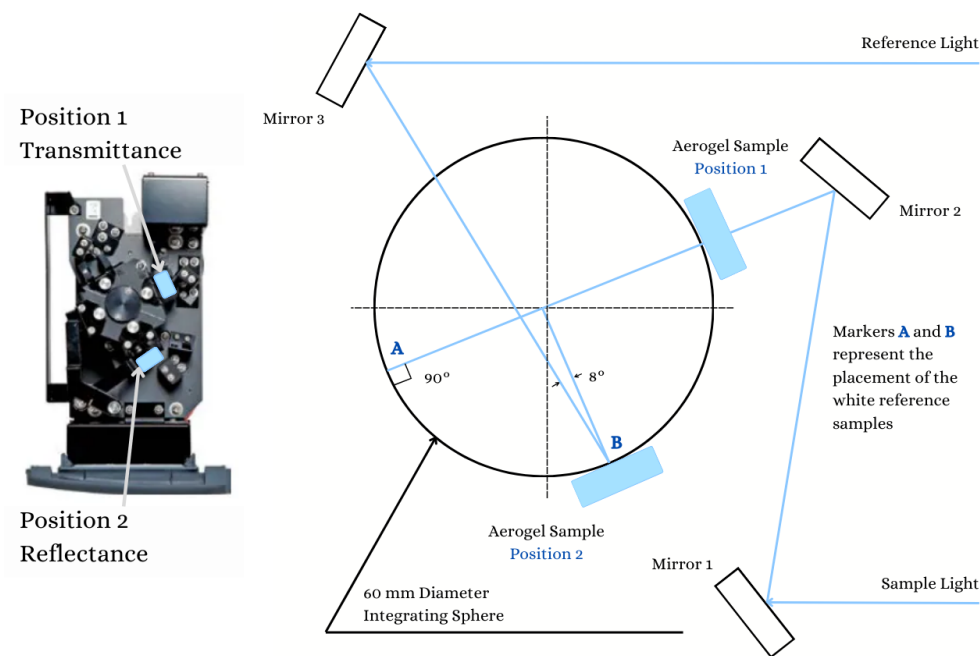


Figure 3.6: Schematic of the Shimadzu UV-2600 spectrophotometer integrating sphere (ISR-2600 Plus) attachment. The diagram outlines the spectral layout of light transmission, along with indicating SA positions for data acquisition. Position 1 is used for hemispherical transmittance and position 2 is used for relative total reflectance.

mounted on the spectrophotometer. Three batches of Cu-sputtered aerogel samples were measured, with each batch containing four SA samples. The batches contained one bare Silica aerogel (BSA), one Cu20@BSA, one Cu@50BSA, and one Cu100@BSA. Thus, UV-Vis spectroscopy measurements were performed on a total of 12 samples.

Consequently, since three measurements were taken of each sample, this led to the acquisition of 36 measurements, encompassing 12 measurements for each batch (9 for the Cu-sputtered aerogels, and 3 for the BSA samples). For instance, the direct transmittance was measured for the BSA sample, followed by the Cu20@BSA sample, the Cu50@BSA, and lastly, the Cu100@BSA sample. This process was carried out for each batch. Similar processes were followed for each type of UV-Vis measurement. The samples that were used for acquisition are seen in Figure 3.3 (recall that all samples are 1 cm thick).

Standardizing the procedural layout for each measurement process was crucial to maintaining consistency and enabling reliable data acquisition. To achieve this, the samples were consistently oriented perpendicular to the incident light, with the detector placed on the opposite side to capture the transmitted light. Consistently maintained parameters included the 5 nm slit width of the light beam, a slow scan speed, and a 2 nm sampling interval. A balance between the scan speed and sampling interval was sought to reduce noise and ensure the acquisition of visually clear and reliable data.

The sample/reference (S/R) exchange is modified according to the type of measurement. The S/R exchange is set to normal for transmittance, while for reflectance it is set to inverse. Prior to data acquisition, a baseline correction scan is performed within the designated wavelength range for measurements. As depicted in Figure 3.6, two white reference plates containing barium sulfate BaSO_4 are essential during the baseline correction scan. During the direct transmission (DT) data acquisition, no external items are adjusted, the measurement is conducted initially without the silica aerogel (SA) sample for the baseline scan and then performed with the SA sample for the actual data recording. The same process is followed for hemispherical transmittance (HT) measurements. However, when recording the total reflectance (TR), the baseline scan involves both reference plates in place. Subsequently, the reference plate at position 2 is replaced with the SA sample for the measurement. After each baseline correction scan, data acquisition was performed using UVProbe, the software integrated with the Shimadzu UV-2600 instrument, enabling the processing and storage of data for further analysis.

3.3.2 Fourier Transform Infrared Spectroscopy

The methods used to attain the FTIR measurements closely paralleled those used to acquire the UV-Vis measurements, utilizing an identical setup with the same number of samples, resulting in 30 measurements. FTIR measurements of the samples are taken before and

after thermal imaging to determine the emissivity. The Bruker Vertex 70 spectrophotometer was employed to attain the direct transmittance of the infrared spectrum of the SA samples. Data acquisition was realized using OPUS, a state-of-the-art measurement, processing, and evaluation software for measuring the spectra. The near-infrared (NIR) and mid-infrared (MIR) spectra measured ranged from 1000 nm to 2500 nm and 2000 to 25000 nm, respectively. All experiments, including NIR and MIR measurements, were conducted employing the same detector (Deuterated Lanthanum- α -Alanine doped TriGlycine Sulfate (DLaTGS)).

A quartz beamsplitter was utilized for NIR measurements, while a potassium bromide (KBr) beamsplitter was employed for MIR measurements. To maintain consistency for repeatability and data reliability, key parameters, including scan resolution, sample scan time, background scan time, and aperture setting, are meticulously configured for optimal performance. The scan resolution is fixed at 8 cm^{-1} , with both sample and background scan times set to 1024 scans. Additionally, the aperture setting, which impacts the amount of information gathered, is set to 8 mm. A narrower aperture improves the resolution by allowing a smaller range of wavelengths to pass through, leading to a sharper and more detailed spectral output. On the other hand, a wider aperture decreases the resolution but allows more light to pass through, thereby enhancing the signal-to-noise ratio. Therefore, keeping the aperture setting aligned with the resolution number yields less noisy results.

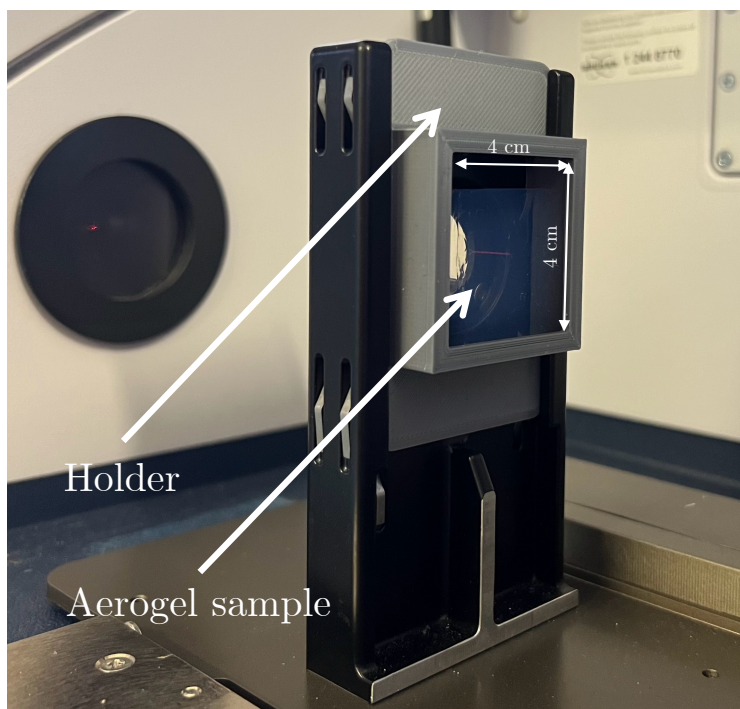


Figure 3.7: Silica aerogel sample placed within the 4.0 cm by 4.0 cm holder, situated inside of the Bruker Vertex 70 machine, used to facilitate direct transmission FTIR measurements.

In order to ensure the reliable and precise collection of data, the aerogel specimen is positioned within a simple 3D printed holder, intercepting the path of the parallel light beam, prompting interactions between the incident light and the aerogel's surface and volume. This holder can be seen in Figure 3.7. Crafted from polylactic acid (PLA), the holder was 3D printed using a Prusa i3 MK3S+. The holder, procured by a previous colleague, provides a placement window measuring 4.0 cm by 4.0 cm, and its backing seamlessly aligns with the equipment accompanying the FTIR machine. Utilizing this holder facilitates convenient adjustments and enhances the flexibility of sample placement.

3.4 Thermal Imaging Characterization

The photothermal effect is a phenomenon where light energy is converted into heat energy. This effect is commonly observed in materials that absorb light which subsequently raises their temperature as a result. When light is absorbed by a material, the energy of the photons is converted into thermal energy, leading to an increase in the material's temperature. Consequently, a fourth batch of silica aerogel samples prepared similarly to the preceding three batches, was designated for photothermal imaging experiments using a Teledyne thermal imaging camera (FLIR A6750sc MWIR) that operates in the waveband range of 3000 nm to 5000 nm. The experimental setup employs a xenon (550 W) arc lamp solar simulator (Sciencetech SF300-C), positioned directly above the samples which is supported by a scissor lift, enabling the distance between the lamp and the sample to be adjusted, as illustrated in Figure 3.8. The solar simulator, which illuminates a circular area with a diameter of about 5.1 cm (2 inches), is accompanied by a 300 W adjustable power supply.

Positioned beneath the silica aerogel samples on the small scissor lift was a reflective, white, PTFE microporous filter sheet, which was placed to minimize heat absorption into the surface. This precautionary measure aimed to prevent any interference from the background, ensuring that the plane on which the aerogel sample rested did not overheat and compromise the accuracy of the results. Throughout all experiments, the lamp irradiated 100 mW/cm^2 (1 Sun) of power which is set by the user. The sample surface remained at a fixed distance of 24 cm away from the lamp to ensure that the irradiated power as depicted in Figure 3.8B, remained at 1 Sun. The IR camera was positioned in a lateral orientation to capture results from the side of the samples. In Figure 3.9 the IR camera is situated to capture side-view images. The imaging cycle extended over a total of 26 minutes, including an initial image captured 1 minute after the lamp was turned on, as well as a final image taken after the lamp was turned off. Between these two points, five separate images were captured at 5-minute intervals (5 min, 10 min, 15 min, 20 min, 25 min).

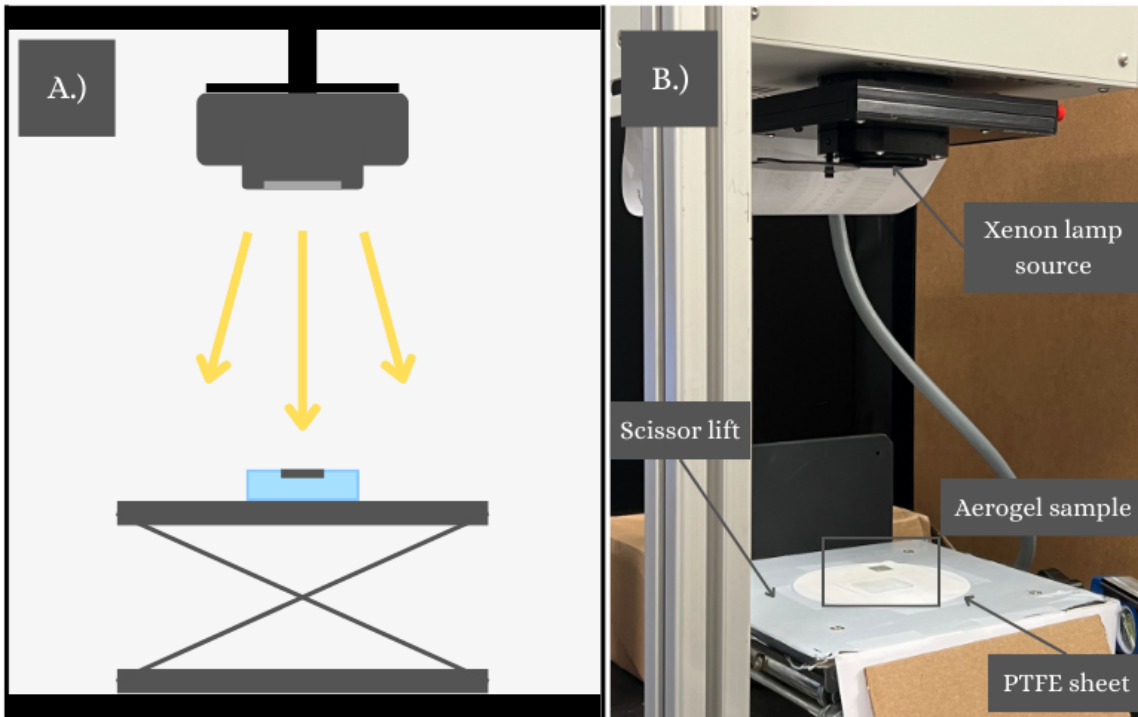


Figure 3.8: Experimental setup of Xenon arc lamp. A schematic of the layout is depicted in A.) while B.) represents the physical laboratory setup, including labels.

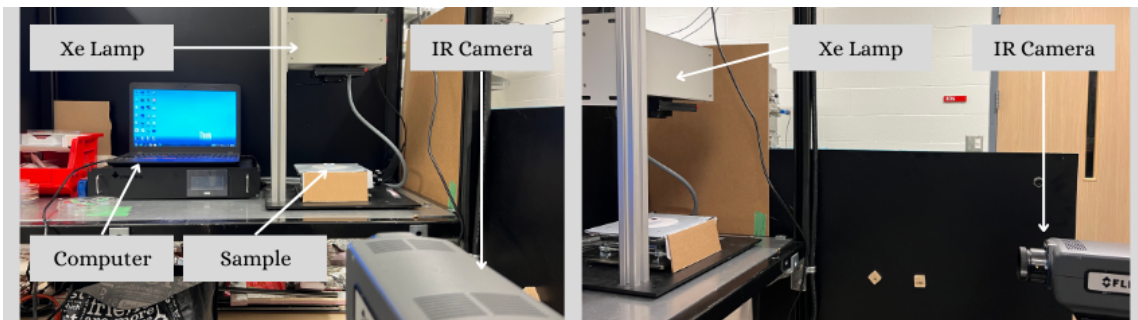


Figure 3.9: Lateral positioning of the thermal imaging camera including experimental laboratory setup of the Xenon arc lamp.

Chapter 4

Experimental Results

Following the completion of the experimental methodologies, the corresponding results were obtained and will be discussed in this Chapter. It was found immediately that the integration of thin Cu films deposited onto the silica aerogel substrate had impacted the structure. This proved particularly advantageous when the particles were finely dispersed and adhered to the aerogel surface and within the aerogel matrix itself. The incorporation of the Cu-sputtered thin films resulted in the emergence of distinctive surface features, a critical aspect that will be expounded upon in this Chapter, providing valuable qualitative and quantitative insights.

4.1 Physical Appearance of Silica Aerogels with Copper Thin Films

Upon immediate inspection, the Cu films generally exhibit a matte-black appearance. However, when viewed from different angles, the Cu appears lustrous, albeit retaining shades of grey and, in certain instances, black. This black appearance is more prevalent in samples with thicker Cu layers deposited on their surface, while those with less Cu deposited onto

their surface tend to appear grey and dull. This phenomenon occurred immediately after sputtering. It is found that Cu and its crystal structure, which, like other noble metals (e.g., Ag and Au), exhibits unconventional characteristics at the nanoscale [49]. Some crystals will appear dark when they strongly diffract, e.g., when the incident light beam is nearly parallel to the so-called (low-index) zone axis of the imaged crystal. This holds for several particularly black clusters (with a nearly cubic shape). The manifestation of surface plasmon resonance (SPR) in copper when reduced to a few nanometers in size contributes to the observed black color, as demonstrated in the spectrophotometric results. However, other factors also play a role, as indicated by Pana et al. [95], who provided an in-depth analysis of the optical properties of Cu thin films. They noted that prolonged exposure to external elements, such as atmospheric air, humidity, and temperature, can lead to surface damage. The contact with air can result in surface oxidation. In the specific context of this work, the Cu-sputtered SA samples were stored in Petri dishes for a duration ranging from weeks to months after their preparation, before optical and thermal measurements were conducted.

4.2 Morphological Characterization Results

A compilation of images depicting both Cu-sputtered and bare Silica aerogels reveals a consistent challenge in imaging. The images display varying degrees of charging and instability, attributed to the inherent difficulty in imaging aerogel materials. Being exceptionally light and absorptive, aerogels exhibit significant vibrations within the SEM imaging chamber. The use of electrically conductive carbon liquid adhesive proved more effective than conductive liquid silver paint. However, both adhesives caused damage to the sample surfaces they contacted, securing the samples with limited effectiveness. Excessive adhesive application rendered the surface unworkable in some cases. The aerogel material absorbs any liquid, impacting its structural integrity upon contact. Even a droplet of water on its surface leads to an immediate collapse of the internal structure, as illustrated in Figure 4.1. Despite these

challenges, careful placement and patience allowed the samples to remain intact on the pin holder with minimal rigidity.



Figure 4.1: Cylindrical Silica aerogel sample (1.5 cm in diameter) displaying internal structural collapse from a droplet of water placed atop its surface.

4.2.1 Top-View SEM Results

Figure 4.2 reveals the nanostructure of the bare silica aerogel with 5 nm of Pt coated on its surface at a magnification of 100,000x. The intricate web-like pattern in the image is characteristic of silica bonds formed after supercritical drying of the wet gel, clearly highlighting the structural composition. The darker regions in the image correspond to voids or pores within the aerogel structure. A closer examination of these darker areas reveals additional silica bonding in the background. The porous scaffolding structure is a common feature observed in SEM images of silica aerogels. Utilizing image processing software, such as ImageJ from the National Institutes of Health, the average pore diameter is determined to be 26.4 nm, aligning with the data provided by Aerogel Technologies LLC, which claims the silica aerogel bars contain a mean pore diameter of 20 nm. Top-view images captured at a magnification of 10,000x, 25,000x, 50,000x, and 100,000x showcase the structure of the Cu thin film, as depicted in Figure 4.3. Some of the images exhibit subtle signs of charging, resulting in the appearance of streaks across the image, which is a common occurrence when imaging aerogel materials because they are highly insulative.

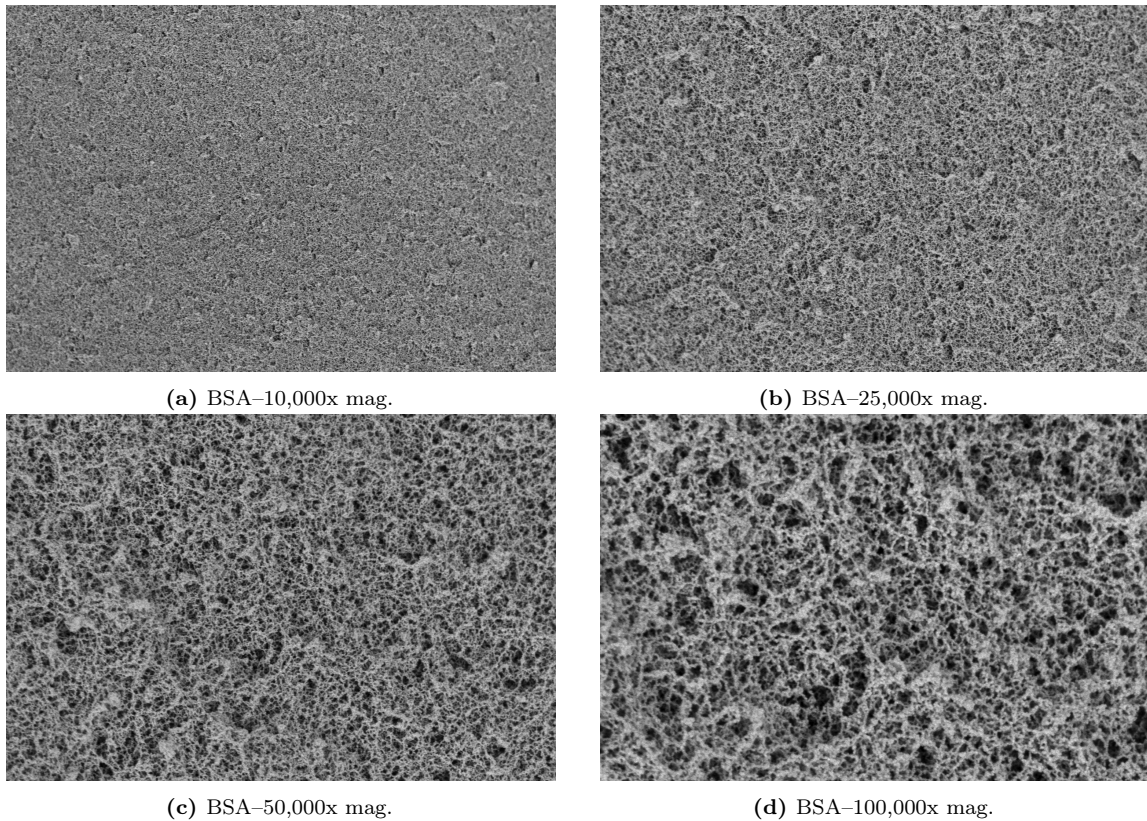


Figure 4.2: SEM images of a BSA sample taken at 2.00 kV and varying magnifications. The image seen at (a) is taken at 10,000x magnification with a scale of $10\ \mu\text{m}$, (b) is taken at 25,000x magnification with a scale of $4\ \mu\text{m}$, (c) is taken at 50,000x magnification with a scale of $2\ \mu\text{m}$, and (d) is taken at 100,000x magnification with a scale of $500\ \text{nm}$.

The top-view images reveal valleys and cracks in the deposited Cu film, particularly evident in Figure 4.3(a)–(c) at 10,000x magnification. A closer examination of the surface in Figure 4.3(j) exposes multiple discontinuities in the Cu deposition. This unevenness may be attributed to heating within the chamber, leading certain Cu clusters to coalesce and solidify faster than other areas. Additionally, it is essential to highlight the brittle nature of the Cu thin film, as any form of stress or rough handling can result in cracking. This could be attributed to the inherently brittle structure of the SA support. At 100,000x magnification, much of the surface features of Cu become clear. At the scale of $500\ \text{nm}$, the images reveal several larger clusters resembling a "cauliflower-like" structure. As the

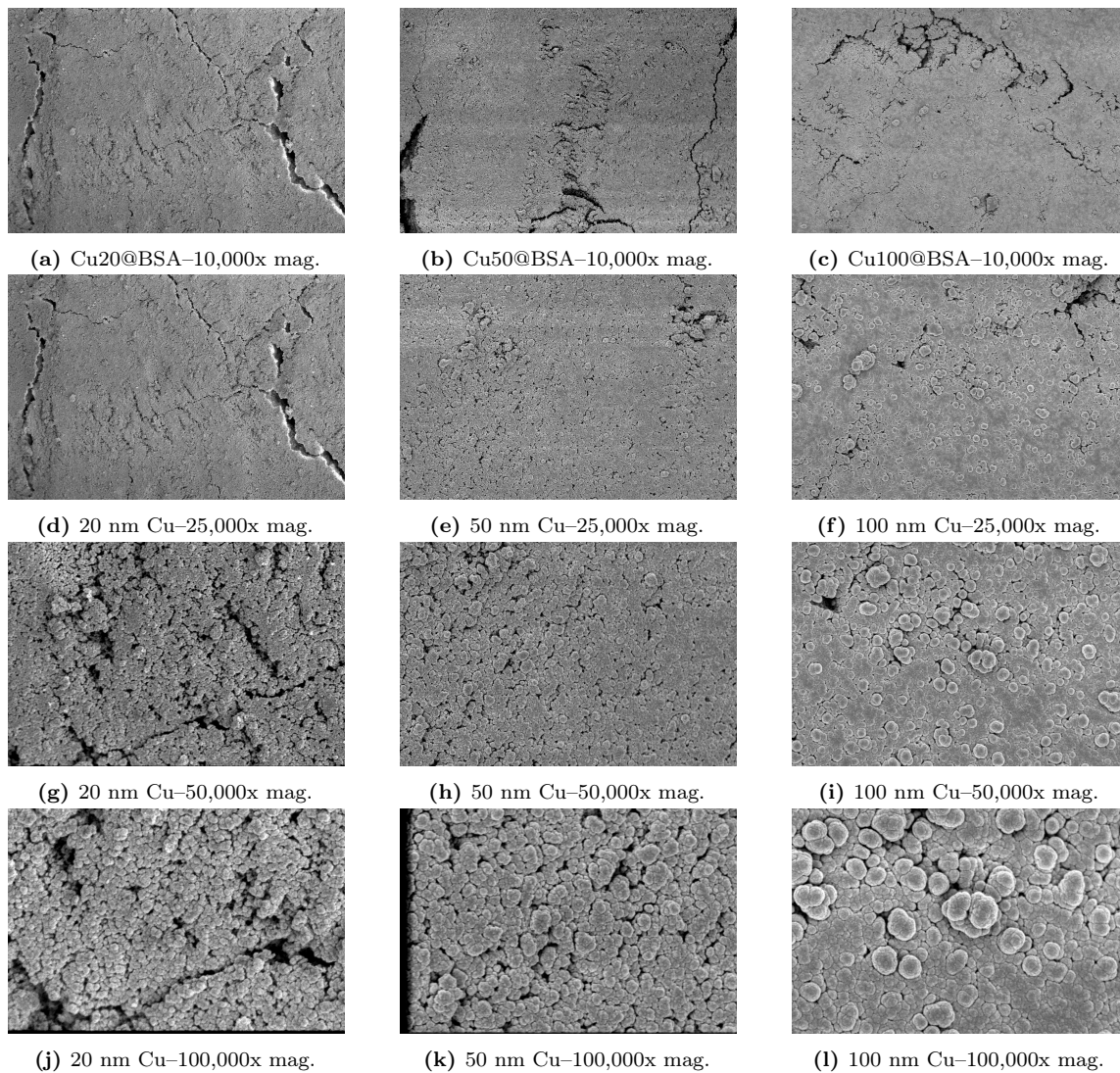


Figure 4.3: SEM images taken at 2.00 kV. Images seen at (a)–(c) are taken at 10,000x magnification with a scale of 10 μm . Images seen at (d)–(f) are taken at 25,000x magnification with a scale of 4 μm . Images seen at (g)–(i) are taken at 50,000x magnification with a scale of 2 μm . Finally, images seen at (j)–(l) are taken at 100,000x magnification with a scale of 500 nm.

thickness of Cu deposition increases, there is a reduction in cracks and voids, accompanied by substantial growth in the size of Cu clusters, as depicted in Figure 4.3(l). Furthermore, with the increment in deposition thickness, a more uniform layer of Cu becomes apparent, resulting in diminished void space and enhanced coalescence of Cu particles. Performing post-processing exclusively on the images depicted in Figure 4.3(j)–(l), as these images provide more discernible results, the average diameter sizes of identifiable clustering for 20 nm, 50 nm, and 100 nm Cu depositions were determined to be 119 ± 76 nm, 135 ± 95 nm, and 190 ± 127 nm, respectively. These values, along with their standard deviations, are provided directly by the imaging software. The escalation in clustering could be attributed to the thicker deposition layer, facilitating the clumping and extended growth of Cu particles.

4.2.2 Cross-Sectional SEM Results

While obtaining cross-sectional images posed challenges, the captured images presented a variety of intriguing findings. Obtaining meaningful results proved especially challenging for the 20 nm and 50 nm Cu depositions. Consequently, the analysis of cross-sectional images focused on silica aerogels with 100 nm of Cu deposited on their surface. The cross-sectional images, featured in Figure 4.4, showcase two perspectives. In Figure 4.4(a), two images depict the interweaving of the deposited Cu with the silica aerogel matrix. On the other hand, Figure 4.4(b) includes a side view of the bare silica aerogel on the left and a lateral image of the Cu deposition on the silica aerogel matrix on the right. In Figure 4.4(a), approximate boundaries between the silica aerogel and the deposited Cu are represented by dotted lines. The images reveal distinct, rounded Cu clusters, resembling mountains. There are several large Cu clusters highlighted in Figure 4.4(b) on the right, enclosed within dashed circles for reference. Additionally, the left side of Figure 4.4(b) affirms the uneven, rough texture discussed throughout this study. At a $5 \mu\text{m}$ scale, the bare silica aerogel surface exhibits a soft and fluffy appearance with a repetitive structure of dips and peaks. In contrast, the Cu deposition profile at a $10 \mu\text{m}$ scale appears rigid and flat, except

for the clustering and other anomalies involving larger randomly deposited Cu clusters.

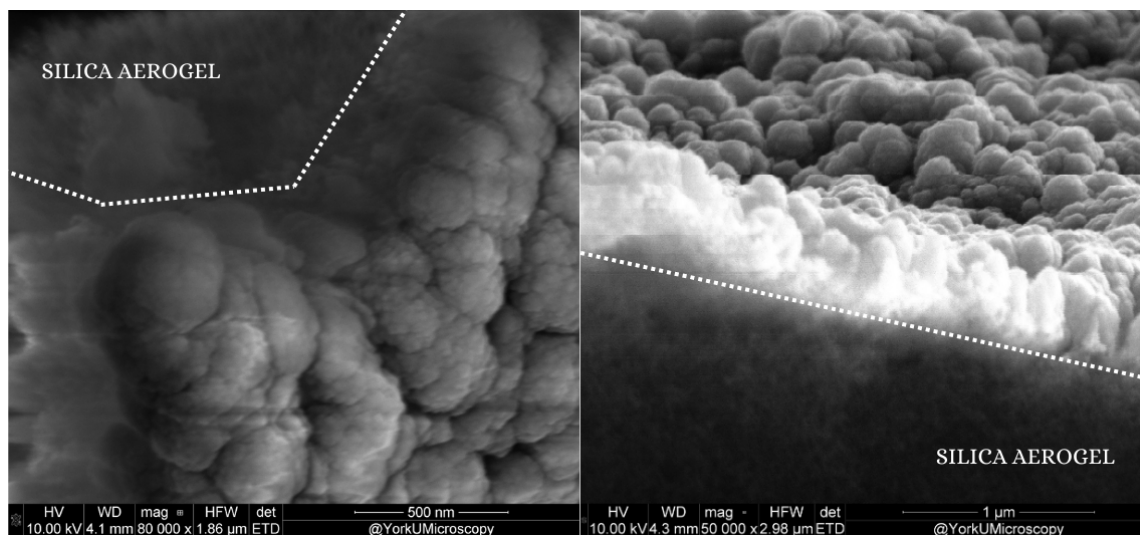
4.2.3 Energy Dispersive Spectroscopy Results

Energy dispersive spectroscopy (EDS) analysis was conducted on Cu100@BSA, as depicted in Figure 4.5. The EDS results conclusively affirmed the penetration of Cu beneath the surface of the BSA and into its nanostructure. Although the precise depth remains unclear, the line scan presented in Figure 4.5D further indicates that trace amounts of Cu deposition have infiltrated about 10 μm beneath the SA matrix. Figure 4.5A displays the original image of the Cu-deposited SA sample, while Figures 4.5B and 4.5C provide detailed views of the Cu deposition within the silica structure. The green coloration signifies Cu, visible even within the nanostructure in Figure 4.5C, while the pink corresponds to Silica.

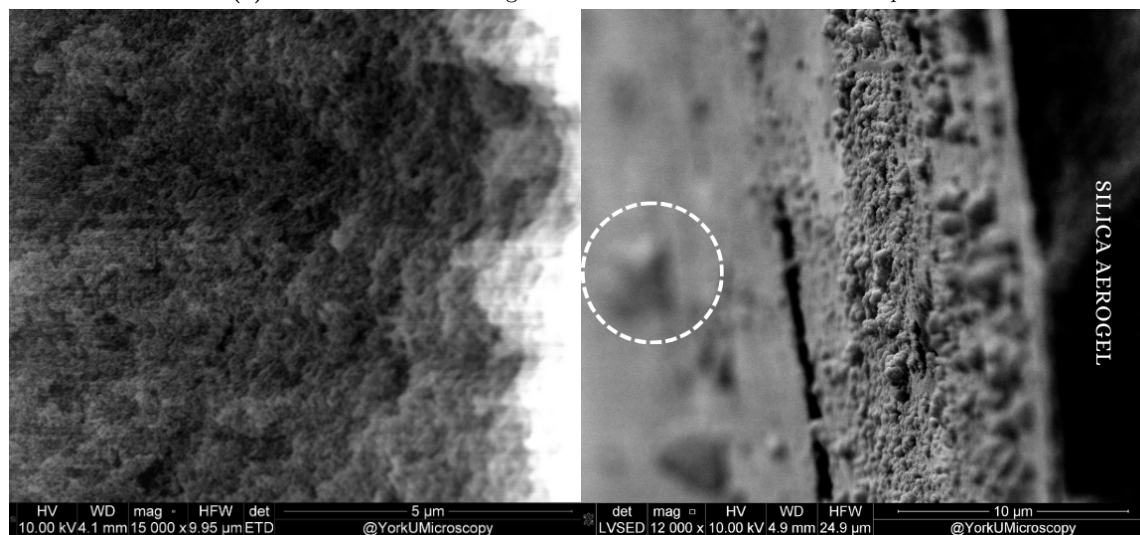
As seen in Figure 4.5D, the point of reference for analysis begins at 100 μm . This corresponds to the uppermost surface of the Cu film on top of the SA sample. Following this point, there is a noticeable peak observed at 98 μm , followed by another at 90 μm . This implies that a 10 μm (from 100 μm to 90 μm) descent into the nanostructure represents the immediate saturation of Cu beneath the surface. At 2 μm below the uppermost surface, the Cu saturation is at its highest point. This is indicative of a distinct layer within the Cu-SA interface. The data for Cu trails into the structure, at smaller concentrations, but still remains present in the Cu-Silica structure. The results of the EDS analysis are summarized in Table 4.1.

Table 4.1: EDS elemental composition results.

Element	Weight %	Atomic %
Oxygen	19.1	35.4
Silica	46.0	48.4
Copper	34.9	16.2



(a) Two cross-sectional images of a small cut-off Cu100@BSA sample.



(b) Two cross-sectional images, with the left one representing the lateral view of the BSA, and on the right another lateral view of a Cu100@BSA sample instead.

Figure 4.4: Cross-sectional images of two different Cu@100BSA samples. In (a), the Cu100@BSA sample displays Cu meshed within the silica aerogel matrix. Whereas (b), represents a lateral view of the BSA on the left, and another Cu100@BSA sample on the right—Cu clustering can be seen.

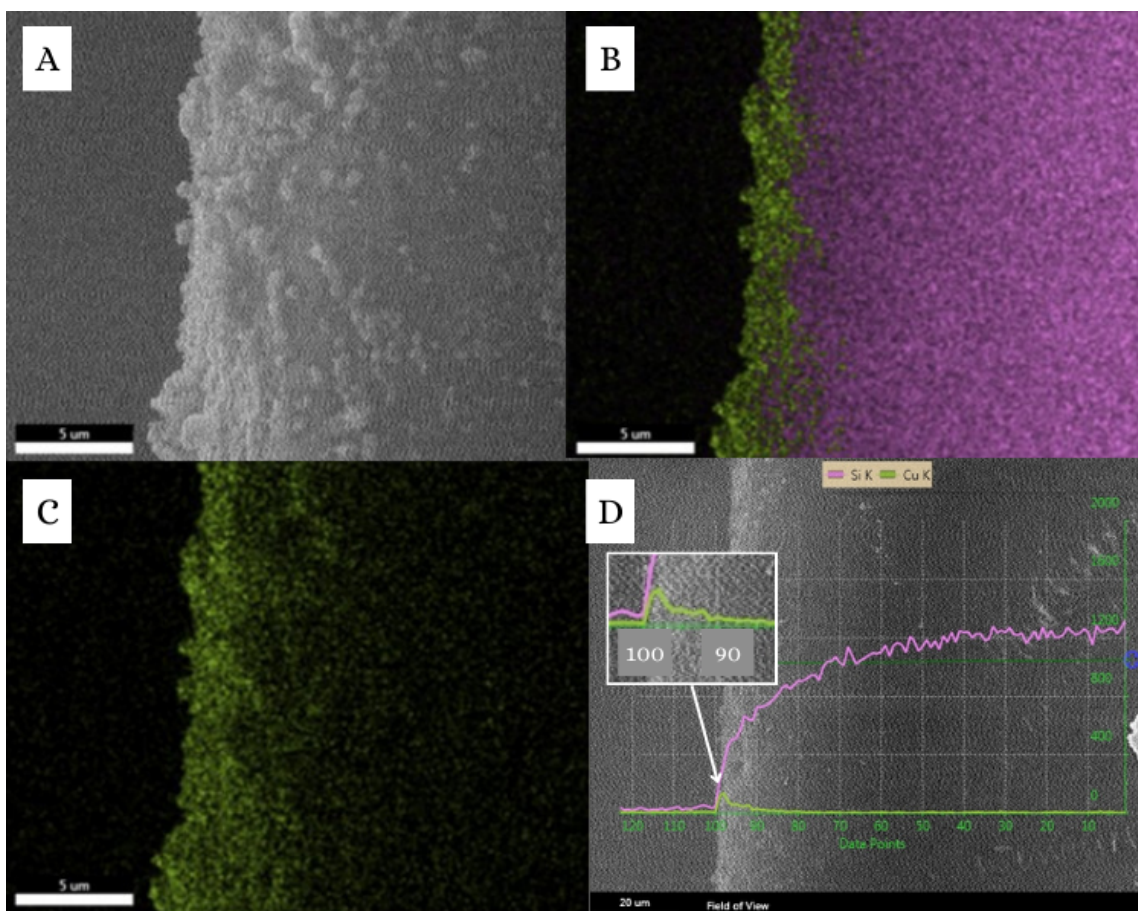


Figure 4.5: EDS images of Cu100@SA sample at a 5 μm scale. A.) Displays the SEM image that was analyzed, B.) and C.) display colorations of the elemental distribution, green referring to Cu and pink to Si. D.) Represents a line scan of the SEM image seen in A.) (the scale is 20 μm).

4.3 Spectrophotometric Characterization Results

The reflectance and transmittance of thin Cu films deposited on silica aerogels were investigated using UV-Vis and FTIR spectroscopy. The characterization aimed to discern the optical behavior of the nanocomposite material. Systematic experiments were conducted to characterize the Cu-deposited silica aerogel composite structures by measuring the transmission and reflection to attain valuable insights into the optical behavior and sensitivity of the Cu-Silica aerogel system.

4.3.1 UV-Visible Spectroscopy

4.3.1.1 Transmission Results

The direct and hemispherical transmission of the bare Silica aerogel (BSA) samples, as well as the Cu-deposited Silica aerogels (Cu20@BSA, Cu50@BSA, and CU100@BSA), are compiled into Figure 4.6 and Figure 4.7, respectively. The transmission spectra of the Cu-deposited SA samples behave similarly, in that, the data displays high values of transmittance in the visible range (400 nm to 750 nm) for the BSA samples while prohibiting the majority of light within the UV regime (220 nm to 400 nm).

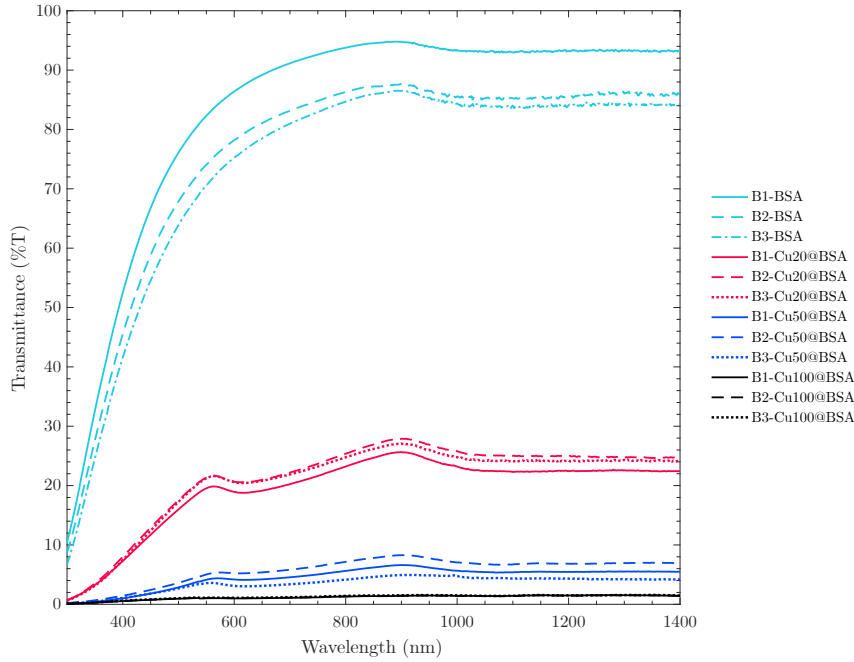


Figure 4.6: Direct percent-transmission (DT) plots of the bare Silica aerogel (BSA), bare Silica aerogel with 20 nm deposited (Cu20@BSA), bare Silica aerogel with 50 nm deposited (Cu50@BSA), and bare Silica aerogel with 100 nm deposited (Cu100@BSA) samples in the UV-Vis-NIR range (220 nm to 1400 nm).

In general, as the amount of Cu increases on the SA surface, the amount of transmitted light decreases, with 100 nm of Cu significantly dropping the transparency of the incoming light.

Preliminary observations suggest that Cu may fill pores at the SA's uppermost surface, impeding light transmission and causing the observed decrease.

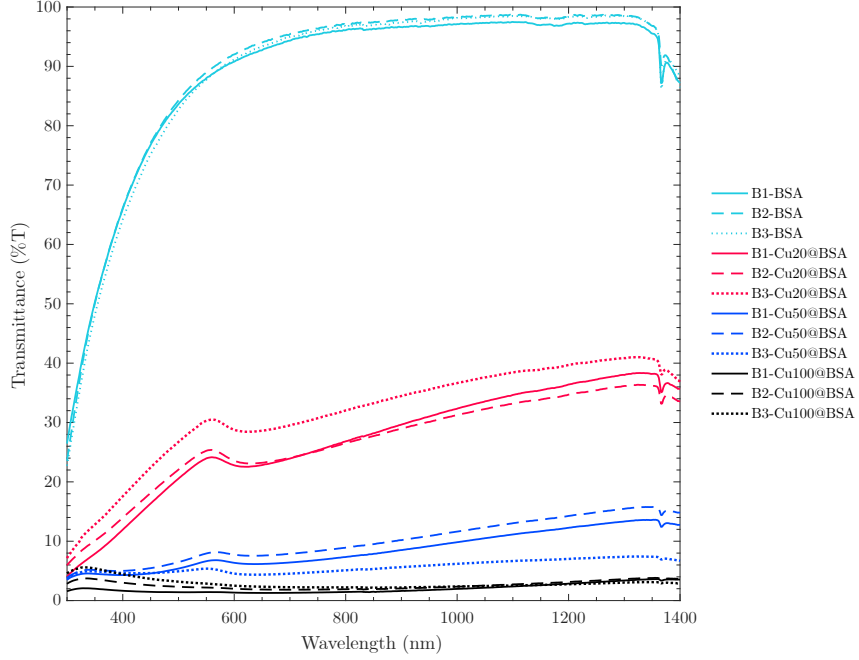


Figure 4.7: Hemispherical percent-transmission (HT) plots of the bare Silica aerogel (BSA), bare Silica aerogel with 20 nm deposited (Cu20@BSA), bare Silica aerogel with 50 nm deposited (Cu50@BSA), and bare Silica aerogel with 20 nm deposited (Cu100@BSA) samples in the UV-Vis-NIR range (220 nm to 1400 nm).

The BSA samples exhibit an average maximum transmittance value of 89.7% through direct transmittance (DT) and 98.3% through hemispherical transmittance (HT). The maximum average transmittance values are calculated and summarized in Table 4.2, for both the DT plot (4.6) and HT plot (4.7). For Cu20@BSA, the maximum average transmittance values are 26.9% (for DT) and 38.6% (for HT). Similarly, for Cu50@BSA and Cu100@BSA the average maximum transmittance values are 6.62% (for DT) and 12.3% (for HT), as well as 1.56% (for DT) and 4.35% (for HT), respectively.

The variation in these values within each thickness category and corresponding batches is

Table 4.2: The calculated average maximum direct transmission and hemispherical transmission across each batch for the BSA, Cu20@BSA, Cu50@BSA, and Cu100@BSA samples.

Sample	Avg. Max DT (%)	Avg. Max HT (%)
BSA	89.7	98.3
Cu20@BSA	26.9	38.6
Cu50@BSA	6.62	12.3
Cu100@BSA	1.56	4.35

generally reasonable, showing no concerning outliers. This prompted a comparison between direct and hemispherical measurements, as seen in Figure 4.8.

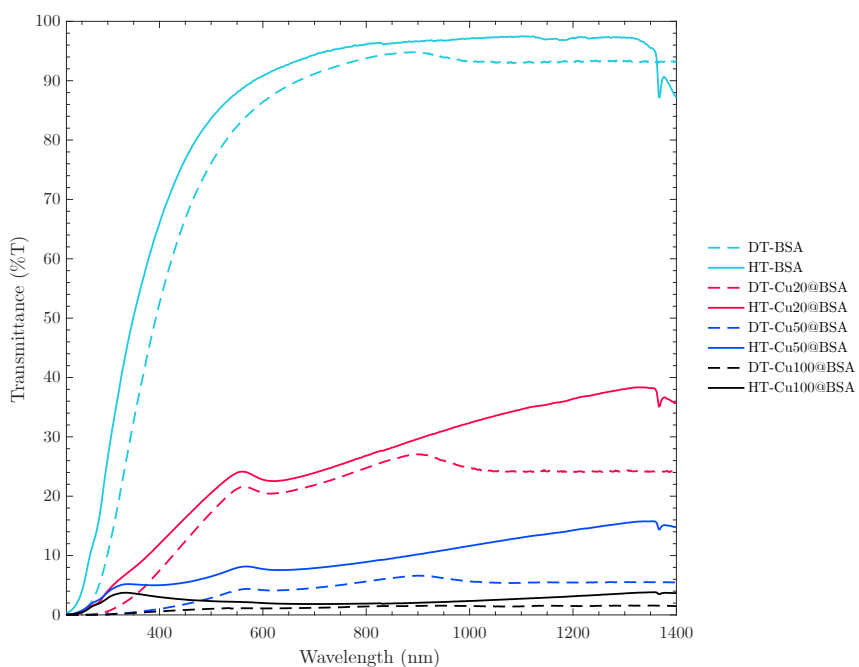


Figure 4.8: Comparison of direct and hemispherical percent-transmission plots of the BSA, Cu20@BSA, Cu50@BSA, and Cu100@BSA samples in the UV-Vis-NIR range (220 nm to 1400 nm).

There is scattering seen in each case. However, it is pronounced in the Cu20@BSA and Cu50@BSA samples, towards the end of the visible range to the beginning of the NIR range (900 nm to 1400 nm). In contrast, the BSA samples and the Cu100@BSA samples show minimal scattering. This observed scattering phenomenon can be attributed to factors such

as polydispersity, sample turbidity, or variations in the composition within the samples. The scattering observed in Figure 4.8 can also be seen in the reflection measurements, seen in Figure 4.9. Furthermore, characteristic peaks in the transmittance spectra can be seen at 550 nm, for all thicknesses, and all batches. The consistent presence of a peak at around 550 nm that the absorption band at 570 nm (green-yellow light) corresponds to the surface plasmon resonance (SPR) resulting from the collective oscillation of the outward valence electrons in Cu, influenced by a resonance interaction with the incident light's oscillating electric field [81].

4.3.1.2 Reflection Results

The percent-reflectance was measured for each batch and each Cu thickness, as seen in Figure 4.9. The data in the plots exhibit small vertical "drops," this is due to the detector being changed at 830 nm. This is present in the transmission results as well, albeit less dramatically apparent. Across the batches and thicknesses, a consistent trend is observed, with the BSA reflecting a significant portion of incident light in the UV range, peaking at 32.3% (measured in batch 2), and reflecting less than 5% in the visible range. In contrast, the Cu20@BSA, Cu50@BSA, and Cu100@BSA samples generally exhibit higher reflectance in the visible range. This can be expected, considering the introduction of the lustrous metallic surface, which imparts a reflective property to the otherwise non-reflective BSA sample. In the UV range, specifically at 250 nm to 300 nm, the bare Silica aerogel (BSA) samples display a sharp peak. However, in line with the BSA reflectance data trend, there is an initial peak followed by a drop, a subsequent shorter peak, and a steady decline. This pattern suggests that, at lower wavelengths, the BSA sample scatters and absorbs more light. The absorption spectra in Figure 4.10 confirm this, and the scattered light, known as Rayleigh scattering [96], is effectively captured by the integrating sphere. Since the integrating sphere measures the total relative reflectance, encompassing both diffuse and specular components, it can capture the significant scattering observed at these wavelengths.

The occurrence of Rayleigh scattering in this region may be attributed to the close refractive index match between the SA samples ($n_{SA} = 1.0 - 1.05$) and air ($n_{Air} = 1.0$).

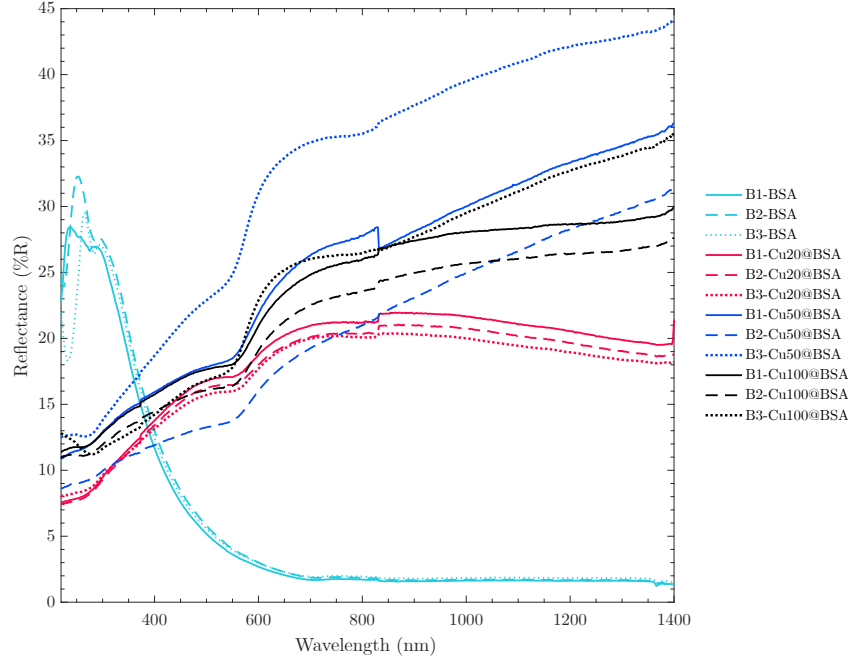


Figure 4.9: Reflection plots in the UV-Vis-NIR range (220 nm to 1400 nm) of the BSA, Cu20@BSA, Cu50@BSA, and Cu100@BSA samples.

The reflectance data presents some variations between batches, particularly evident in the Cu50@BSA samples. For example, the Cu50@BSA sample in batch 3, displays the highest reflection values at 44.2%, with the Cu100@BSA sample in batch 3 being 8.7% lower. This discrepancy can be attributed to the thin film topology, the sizes of the deposited Cu clusters, and scattering. At the nanoscale, this can influence the reflection properties. It could also be the case that the increased scattering observed in Cu20@BSA and Cu50@BSA samples contributes to a subsequent rise in reflection. This kind of scattering can be indicative of Mie scattering, as this becomes less wavelength-dependent and can be more significant for larger Cu particles or clustering [97]. Additionally, each scattering event can lead to increased

absorption, which is seen when comparing the reflection (Figure 4.9) and absorption (Figure 4.10) spectra. Either way, the observed higher reflectance in thinner Cu nanofilms compared to thicker ones is likely a result of complex interactions between light, film thickness, and the unique optical properties of nanoscale materials. It is hypothesized that even though the samples have varying thicknesses, any variations in the material composition or structure might result in similar reflective behaviors at specific wavelengths. However, the occurrence of an anticipated reflection pattern may arise from running experimental tests for prolonged periods and could be revealed to depend on the thickness of the thin film.

4.3.1.3 Absorption Results

UV-Vis spectra of the SA nanocomposite samples revealed distinct absorption features indicative of the SPR effect. The absorption spectra, plotted in Figure 4.10 display the behavior of the spectra for each batch of Cu20@BSA, Cu50@BSA, and Cu100@BSA samples. This data was calculated using the law of conservation of energy (Equation 4.1) in the context of the interaction of light with a material. The scattering phenomena observed in the transmission results, similar to the reflection findings, can impact the absorption. Increased scattering could potentially result in more light being absorbed rather than being reflected or transmitted. The absorption of the BSA samples, as well as the Cu20@BSA, Cu50@BSA, and Cu100@BSA samples, contain high values in the UV range. The BSA samples exhibit a steep, but steady decline in the visible range for absorption, while the Cu20@BSA, Cu50@BSA, and Cu100@BSA samples, remain above 40%. This is indicative of their high transmittance in the visible range, representing a tradeoff between absorption and transmittance.

$$1 = A + T + R \tag{4.1}$$

The prominent peaks observed at 200 to 300 nm and 500 to 600 nm in Figure 4.10 suggest

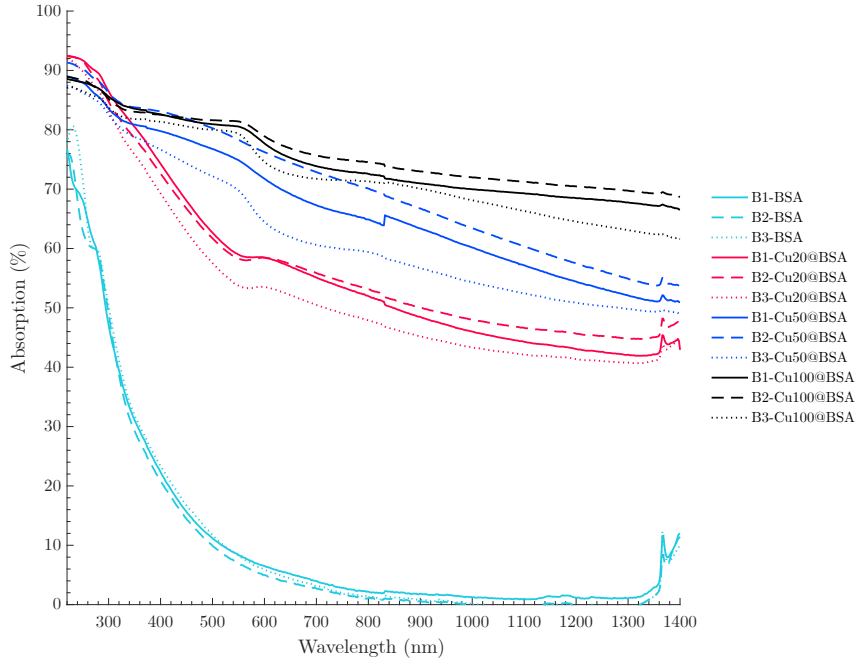


Figure 4.10: Calculated percent-absorption spectra (1-T-R) in the UV-Vis range (220 nm to 1400 nm) of the BSA, Cu20@BSA, Cu50@BSA, and Cu100@BSA samples.

that the presence of thin Cu nanofilms and their interaction with the surrounding silica matrix are undergoing SPR effects. In the UV range, the Cu100@BSA samples consistently exhibit relatively high absorptivity, ranging between 82% and 90%. Throughout the visible to NIR range, the Cu100@BSA samples maintain absorptivity levels above 60%. Conversely, the Cu20@BSA and Cu50@BSA samples follow a similar trend but with lower absorptivity values. This observed behavior suggests strong light absorption by the samples in the UV range, potentially linked to intrinsic electronic transitions or resonance effects associated with the specific properties of the Cu film and the SA matrix. The decline in absorptivity in the visible range implies that the material has a comparatively lower propensity to absorb light within this spectrum. Alternatively, as observed in the reflection spectra, it could be attributed to increased scattered light within the porous matrix, leading to more light being

absorbed instead of exiting the SA.

4.3.2 Fourier Transform Infrared Spectroscopy

The full FTIR wavelength spectra (1000 nm to 25,000 nm) of the BSA, Cu20@BSA, Cu50@BSA, and Cu100@BSA samples are depicted in Figure 4.11.

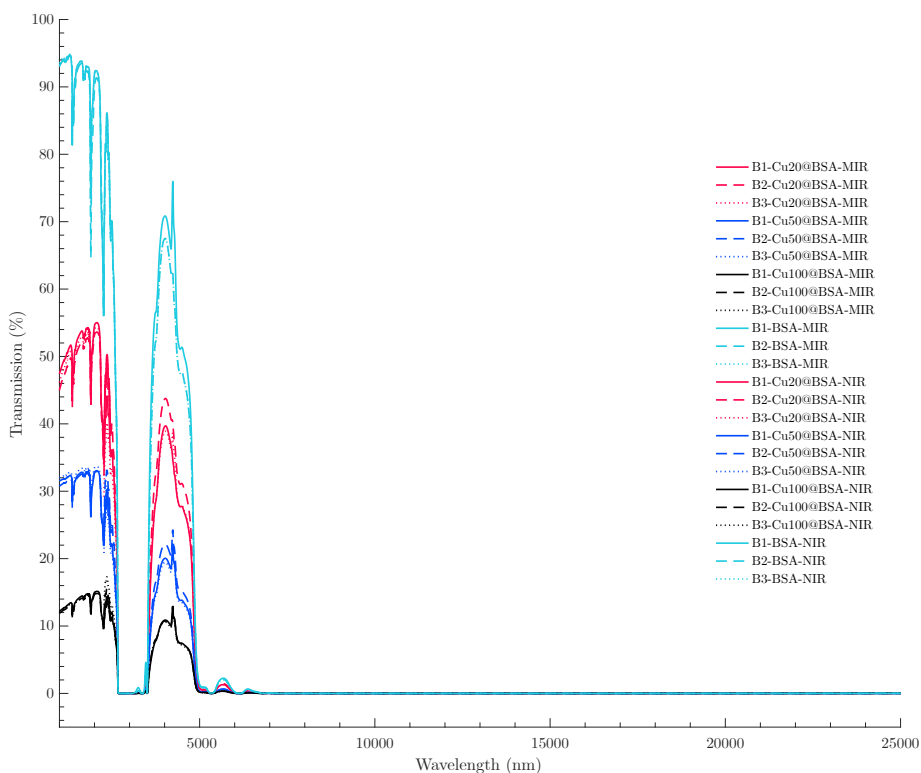


Figure 4.11: FTIR direct transmittance spectra containing plots of the BSA, Cu20@BSA, Cu50@BSA, and Cu100@BSA samples across the full wavelength spectra (1000 nm to 25,000 nm), particularly split into the NIR (1000 nm 2500 nm) region, and MIR to FIR regions (2500 to 25000 nm).

Additionally, depicted in Figure 4.12, features a closer examination (1000 nm to 7000 nm) of the spectra that contains areas of interest, such as various potential absorption dips and

transmission bands. Generally, the data exhibits a consistent behavior in shape across the batches and thicknesses. The data indicates that an increase in the thickness of Cu-sputtered deposition results in a decrease of approximately 20% in direct transmittance, particularly in the NIR range (1000 nm to 2500 nm).

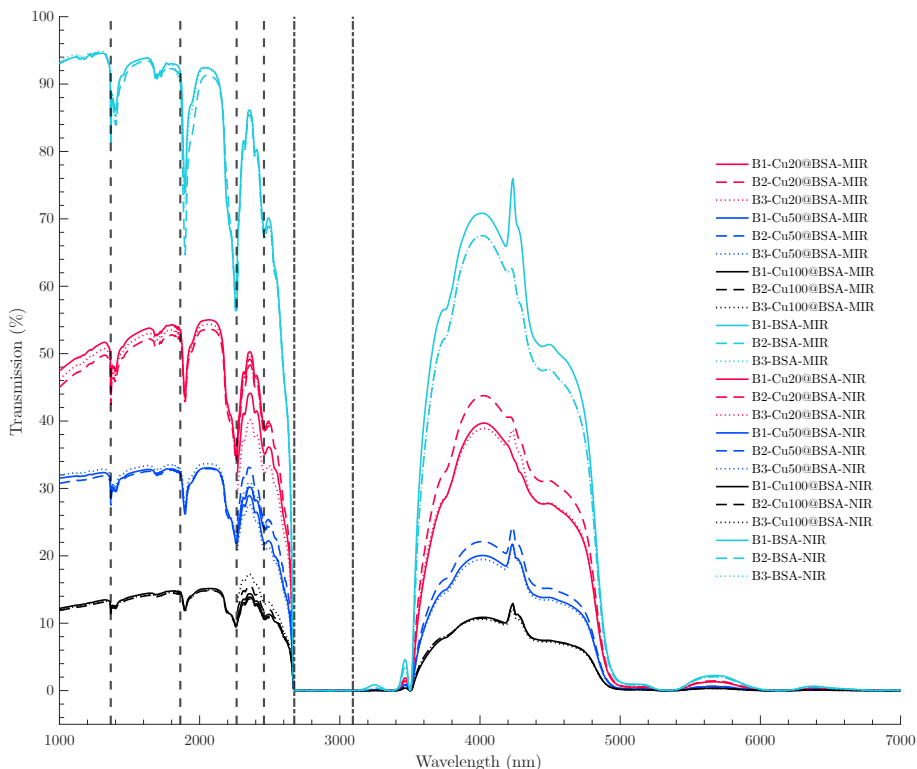


Figure 4.12: Close-up of FTIR direct transmittance spectra containing plots of the BSA, Cu20@BSA, Cu50@BSA, and Cu100@BSA samples in the NIR (1000 nm 2500 nm) and MIR regions (2500 to 7000 nm). Dashed (- -) black lines indicate absorption dips, with the dotted dashed (.-) black lines indicating a transmission band, indicative of water absorption.

For the BSA batch of samples, the maximum NIR transmittance reaches 94.7% (B2). In contrast, the Cu20@BSA, Cu50@BSA, and Cu100@BSA samples exhibit lower maximum NIR transmittance values of 55.0% (B1), 33.7% (B3), and 15.2% (B1), respectively. The average deviation between each sample in each batch of the results was determined to

assess the consistency of the data, which is displayed Table 4.3. The calculation of the average deviation involves determining the mean of each sample within its respective batch, such as averaging 94.6% (B1-Cu@20BSA-NIR), 94.7% (B2-Cu@50BSA-NIR), and 94.5% (B3-Cu@100BSA-NIR) to obtain a mean value of 94.6%. Subsequently, the average deviation is computed using Equation 4.2 for each sample in their given batches.

$$Avg.Deviation = \frac{|B1 - Mean| + |B2 - Mean| + |B3 - Mean|}{3} \quad (4.2)$$

Table 4.3: Average deviation (%) between each batch of measurements in the NIR and MIR range. A smaller average deviation between measurements implies experimental reproducibility.

Sample	NIR Avg. Deviation (%)	MIR Avg. Deviation (%)
BSA	0.839	6.23
Cu20@BSA	2.58	2.95
Cu50@BSA	1.43	2.08
Cu100@BSA	0.309	0.999

Across the entire spectra, there appears to be no significant deviation, suggesting an overall coherence in the data, leading to reproducible results in this experimental process. In general, the Cu-sputtered silica aerogel composites exhibit increased light transmission in the UV-vis-NIR range and higher absorption in the MIR to far-infrared (FIR) range. When examining Figure 4.12, there is a distinctive transmission band from 2675 nm to 3000 nm that is found in each plot, denoted by the dashed-dotted lines (-.). The near-zero transmittance in this specified wavelength range typically implies a significant degree of absorption or reflection occurring within the material. When compared to FTIR spectra for water and SiO₂-glass, the identified bands in the spectra align. This suggests the potential presence of water, particularly given that the silica aerogel samples are hydrophilic and susceptible to moisture absorption [98, 99].

Furthermore, the dashed, black lines (- -) at approximately 1365 nm, 1865 nm, 2265 nm, and 2460 nm signify distinct absorption dips. A basic chemical composition analysis reveals various stretching and bending vibrations. Two hydroxyl (-OH) absorption bands are

discernible, with the more prominent one spanning from 2675 nm to 3000 nm and the other at 2265 nm. The latter hydroxyl stretching and bending vibrations suggest the presence of water. Absorption bands around 1365 nm and 1865 nm are significant, representing Silicon-Oxygen vibrations indicative of the SiO_2 (Silica) structure in the SA samples. Identifying absorption features associated with Cu or Cu-Oxides in the NIR and MIR region (at 2460 nm) can be challenging due to the general lack of strong absorption bands for metals in this range.

4.4 Thermal Imaging Results

The photothermal response of BSA and Cu-sputtered SA samples is qualitatively explored to understand temperature variations with different Cu thicknesses on the SA surfaces. This can be qualitatively observed in Figure 4.13 and Figure 4.14 for the BSA and BSA@BSA samples, as well as in Figure 4.15 and Figure 4.16 for the Cu100@BSA and BSA@Cu100@BSA samples, respectively. This investigation aims to identify the maximum temperatures at each thickness. The 26-minute imaging cycle reveals an expected temperature rise followed by a decline post-solar simulator deactivation (see Figure 4.17). The recorded temperatures are along a defined line specified in the IR camera software, which, is set by the user, and is seen in Figure 4.13, 4.14, 4.15, and 4.16, passing through the center of each sample undergoing analysis. A consistent pattern is observed across the different experimental setups, indicating a temperature increase when a BSA sample was placed on top of the Cu-sputtered SA samples.

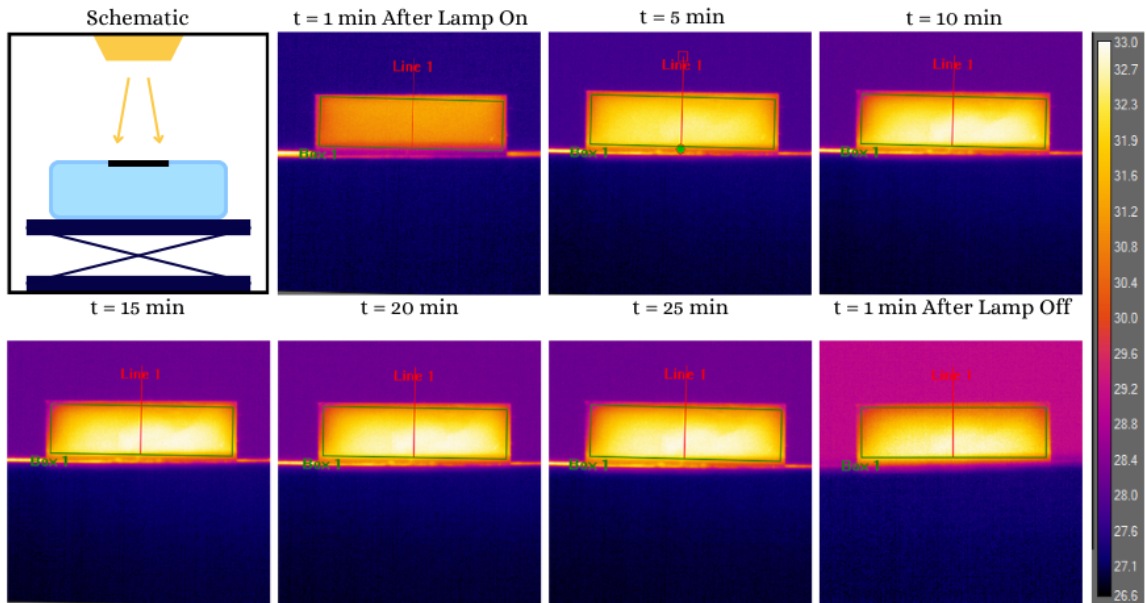


Figure 4.13: Lateral infrared images of BSA sample at 1 minute after the solar simulator is turned on, followed by images taken at five 5-minute intervals from 1 to 26 minutes after the solar simulator was turned on. A schematic of the setup is seen in the top right corner.

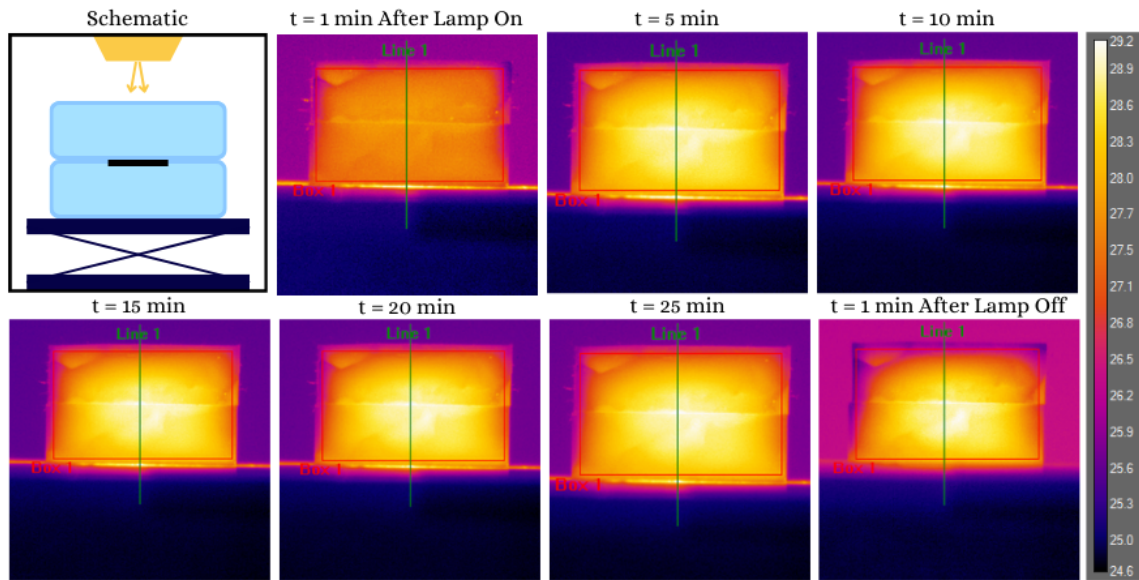


Figure 4.14: Lateral infrared images of a BSA sample, with another BSA placed on, at 1 minute after the solar simulator is turned on, followed by images taken at five 5-minute intervals from 1 to 26 minutes after the solar simulator was turned on. A schematic of the setup is seen in the top right corner.

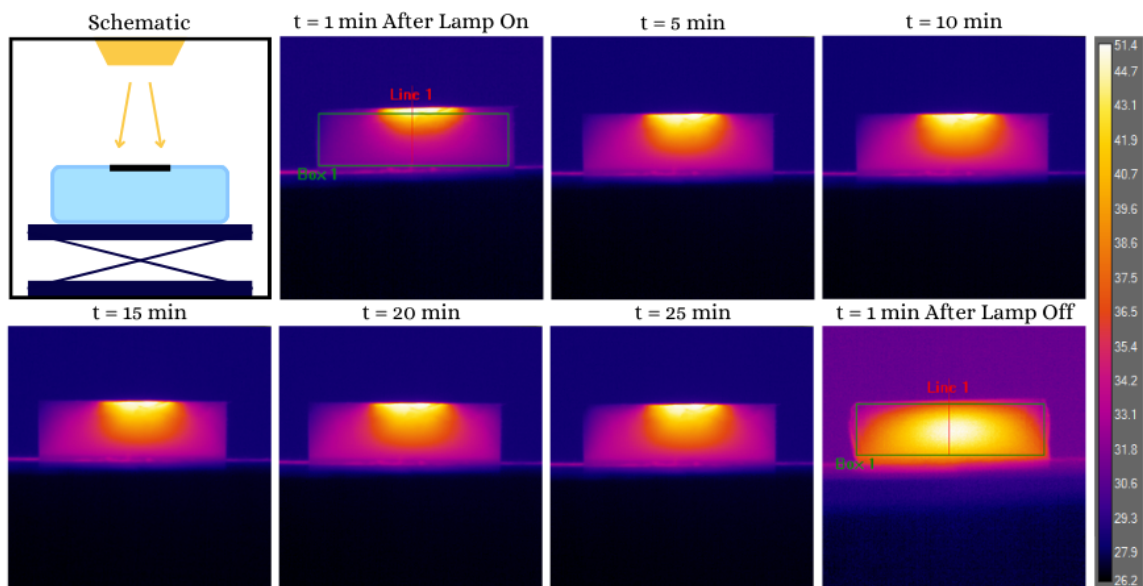


Figure 4.15: Lateral infrared images of a Cu100@BSA sample at 1 minute after the solar simulator is turned on, followed by images taken at five 5-minute intervals from 1 to 26 minutes after the solar simulator was turned on. A schematic of the setup is seen in the top right corner.

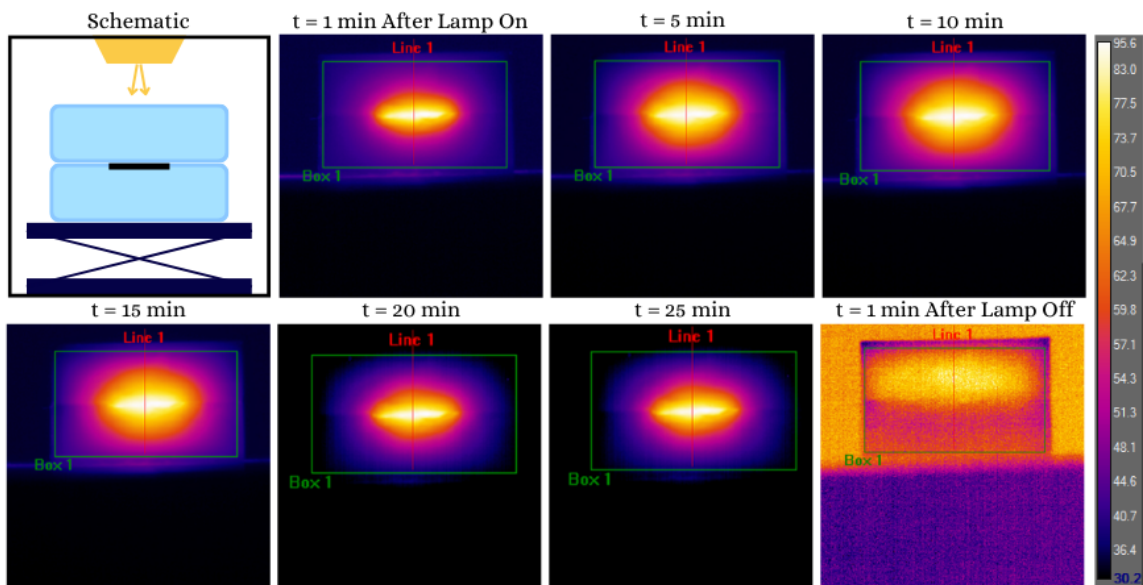


Figure 4.16: Lateral infrared images of a BSA@Cu100@BSA sample, at 1 minute after the solar simulator is turned on, followed by images taken at five 5-minute intervals from 1 to 26 minutes after the solar simulator was turned on. A schematic of the setup is seen in the top right corner.

The thermal saturation of the samples is noticeable, with the temperature reaching a specific value merely 1 minute after the lamp is turned on, and remaining stable for the duration of the 25-minute period with the lamp on, as seen in Figures 4.13, 4.14, 4.15, and 4.16. After the lamp is turned off, the heat dissipates fairly quickly, returning the temperature to its initial value 1 minute after the lamp was turned on. A discrepancy exists between assumed and actual emissivity for Cu-coated samples, impacting thermal imaging accuracy. Emissivity represents the efficiency with which an object emits thermal radiation compared to a perfect blackbody. Therefore, the amount of radiation emitted at a given temperature is affected by the emissivity value. The temperature measurements obtained during this experimental process are considered relative and do not represent the actual temperature due to this reason.

4.4.1 Lateral Imaging Results

As can be seen in the plot in Figure 4.17, that by placing a BSA sample on top demonstrates a nearly twofold temperature rise. The observed temperature increase can be attributed to the enhanced heat retention, analogous to the effect of adding a secondary insulating layer. Specifically, in the Cu100@BSA sample without the BSA sample (Figure 4.15, a temperature recording of 50°C was recorded at 5 minutes, whereas the addition of the BSA (Figure 4.16) resulted in a temperature of 90°C at the same time point. In addition to the data presented in Figure 4.17, there is a noticeable correlation between the thickness of the Cu sputtered on the surface and the resulting temperature. By the 15-minute mark, it is clear that the temperature in the SA samples has reached saturation, making it a point of interest for further study. Therefore, Figure 4.18 and Figure 4.19 focus on displaying only the 15-minute cases, effectively conveying the observed behavior in each case. To generate the plots seen in these Figures, some adjustments to the data were necessary. The IR camera reads the line, set by the user, as pixels and creates a temperature distribution based on the position of the line.

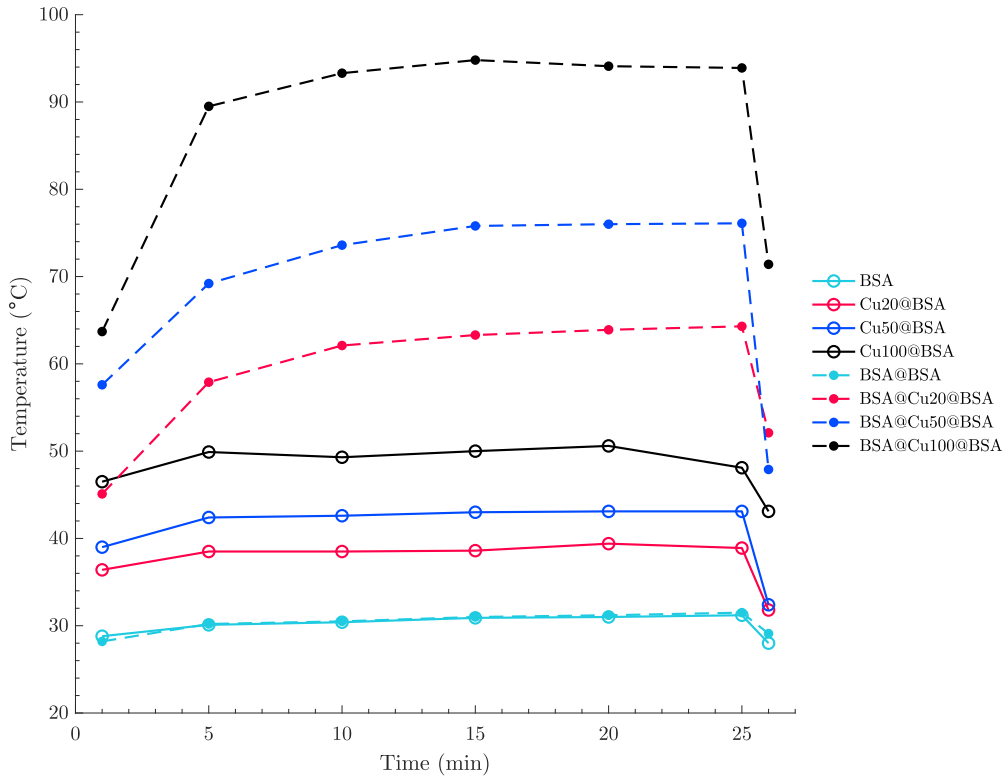


Figure 4.17: Plots of the BSA, Cu20@BSA, Cu50@BSA, and Cu100@BSA samples recorded temperature versus time of irradiation period. Samples with Cu are placed down with the deposition side facing the solar simulator. Dashed lines represent temperature values that were recorded with a BSA placed on top of the Cu-sputtered sample, and solid lines represent temperatures recorded with no BSA on top.

The schematic in Figure 4.18A illustrates the experimental setup, enabling the derivation of a scaling factor (SF), as shown in Equation 4.3.

$$\text{Scale Factor (SF)} = \frac{\text{Thickness in cm}}{\text{Thickness in pixels}} \quad (4.3)$$

As a result, all pixel values are converted into centimeters and observed on the x-axis of Figure 4.18 and Figure 4.19. This provides a convenient method for analyzing the depth of the temperature profile.

In both Figures 4.18 and 4.19, it is evident that the behavior of each plot is similar. For the BSA temperature profiles, seen in Figure 4.18, the maximum temperature occurs at a depth of 0.1 cm into the sample, with a temperature value of 29.9°C. The BSA@BSA measurement shows a slight increase, with a maximum temperature of 30.6°C at a depth of 1.6 cm.

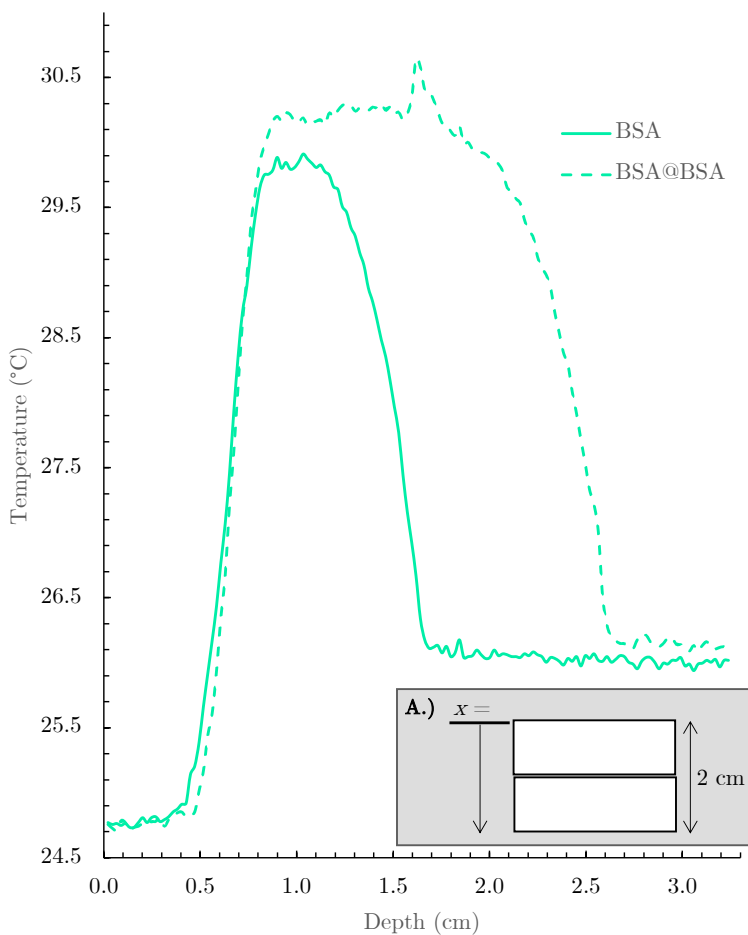


Figure 4.18: The temperature profiles with depth are illustrated for bare Silica aerogel (BSA), depicted by the solid line, and BSA@BSA, shown by the dashed line. Panel A.) presents a schematic of BSA@BSA, where a datum reference point establishes that the top of the SA sample is x equal to 0 cm, with the value increasing as one progresses through the depth of the SA, reaching the bottom at x equal to 1 cm.

Figure 4.19 displays data for the Cu20@BSA, Cu50@BSA, and Cu100@BSA samples. The Cu20@BSA sample reaches a maximum recorded temperature of 38.2°C at a depth of 0.6

cm, while the BSA@Cu20@BSA records a maximum temperature value of 69.6°C at a depth of 1.7 cm. Similar increasing trends are observed in the 50 nm and 100 nm samples. The Cu50@BSA sample achieves a maximum recorded temperature of 38.7°C at a depth of 0.6 cm, while the BSA@Cu50@BSA sample reaches a maximum temperature of 73.4°C at 1.6 cm. Finally, in the Cu100@BSA and the BSA@Cu100@BSA samples, the maximum recorded temperatures are 47.1°C at a depth of 0.7 cm, and 94.8°C at a depth of 1.6 cm, respectively.

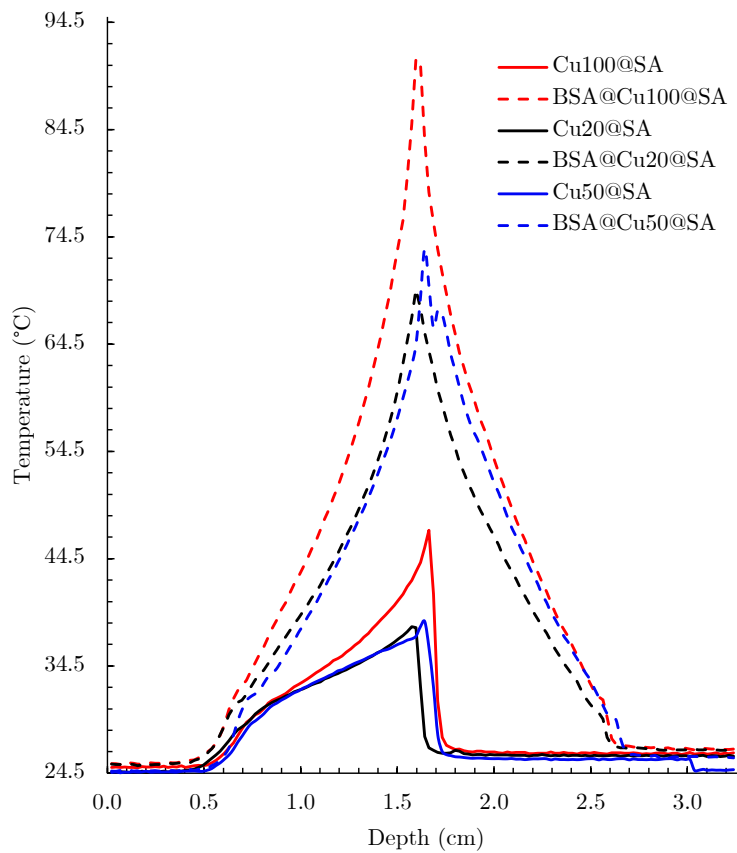


Figure 4.19: The temperature profiles with depth, recorded at 15 minutes, are presented for Cu20@BSA, Cu50@BSA, and Cu100@BSA samples, alongside an identical set of measurements for each case with a BSA on top.

4.4.2 Thermal Imaging Summary of Results

In general, it is important to keep in mind that the thermal camera's reliance on emissivity values for temperature calculations, combined with the reflective properties of the Cu layer and potential emissivity variations with thickness, may lead to inaccurate temperature measurements. The presence of Cu could lower the perceived emissivity, affecting temperature readings. However, the main observations from the plots reveal the maximum temperatures and their corresponding occurrences. Specifically, without a BSA positioned atop the Cu20@BSA, Cu50@BSA, and Cu100@BSA samples, the temperature values reach their peaks at 39.4°C, 43.1°C, and 50.6°C, respectively, after 20 minutes, 25 minutes, and 20 minutes. On the other hand, when a BSA is placed over the samples, the temperature values reach their peaks at 64.3°C, 71.6°C, and 94.8°C, respectively, after 25 minutes for both the 20 nm and 50 nm cases, and after 15 minutes for the 100 nm case. Based on these temperature recordings, it is evident that the highest temperature values are observed with the Cu100@BSA samples, while the lowest values are associated with the Cu20@BSA, and the Cu50@BSA samples exhibit temperatures in between the two. SA substrates with Cu sputtered on the surface are a straightforward concept, serving as an alternative to carbon aerogels that rely on the photothermal effect in various applications [41, 81–83]. In summary, as the thickness increases, so does the temperature.

Chapter 5

Conclusion

5.1 Discussion of Results

5.1.1 Morphology of Nanocomposite Silica Aerogel Samples

The initial objective of this research was to investigate the morphological intricacies of nanocomposite materials formed by depositing thin metal films onto SAs through magnetron sputtering. Top-down SEM images of the Cu20@BSA, Cu50@BSA, and Cu100@BSA samples revealed the structural variations in the Cu films atop the BSA samples. These images provided insights into the structure of the deposited Cu films, revealing features such as cracks, valleys, and Cu clustering at various magnifications. While utilizing image processing tools, the average diameter sizes of identifiable clustering for 20 nm, 50 nm, and 100 nm Cu depositions were determined to be 119 ± 76 nm, 135 ± 95 nm, and 190 ± 127 nm, respectively. Thin film cracks, valleys, and other discontinuities within the film could be ascribed to several factors, including uneven heating in the chamber, the inherent brittleness of the Cu film atop an already fragile support, or potential issues during storage and material handling. To investigate the hypothesis of Cu penetration into SA samples, cross-sectional SEM-EDS images were specifically conducted for Cu100@BSA samples. EDS line scan

results for Cu100@BSA samples revealed that Cu infiltrated the uppermost SA surface by 2 μm and extended up to 10 μm into the substrate before gradually diminishing. Although the confirmation of Cu beneath the SA surface was established, the precise depth of Cu penetration remained unknown.

5.1.2 Metallic-Coating Thickness & Silica Aerogel Properties

The second objective of this study was to investigate the influence of varying metallic coating thickness on the transmittance, reflectance, absorption, and photothermal properties of nanocomposite SA samples. Optical characterization spanning the UV-Vis, NIR, and MIR spectra (220 nm to 25,000 nm) was conducted. UV-Vis measurements of the nanocomposite SA samples revealed high transmittance, with the average maximum direct transmission (DT) and hemispherical transmission (HT) of BSA at 89.7% and 96.3%, respectively. However, Cu20@BSA, Cu50@BSA, and Cu100@BSA samples showed lower DT and HT, indicating reduced transparency as Cu thickness increased. Reflection measurements demonstrated significant scattering in Cu20@BSA and Cu50@BSA in the visible-NIR range. In the UV range, specifically around 250 nm to 300 nm, reflectance measurements of the BSA samples suggested increased scattering and absorption at lower wavelengths. SPR absorption features, specifically at 550 nm, were observed in UV-Vis measurements. While BSA samples exhibited a rapid drop in absorption, Cu-containing samples maintained over 40% absorption into the visible-NIR range.

Further infrared optical characterization revealed distinct transmission bands and absorption dips in the nanocomposite SA samples. A transmission gap between 2675 nm to 3000 nm, consistent across all batches, suggested moisture absorption, aligning with the characteristics of water. Absorption dips at 1365 nm, 1865 nm, 2265 nm, and 2460 nm indicated the presence of hydroxyl ($-\text{OH}$) bonds, silicon-oxygen (aligning with SiO_2 -glass) vibrations, and a potentially quite weak Cu-Oxide(s) absorption dip, respectively. Notably, as Cu thickness increased, there was a noticeable decrease in transmittance across the samples. A

qualitative exploration of the photothermal response involved lateral imaging under a solar simulator for BSA and Cu-sputtered SA samples over a 26-minute session. Results indicated a temperature increase when a BSA sample was placed on top of Cu-sputtered SA samples, attributing to enhanced heat retention. Specifically, in the Cu100@BSA sample without the BSA sample, a temperature recording of 50°C was recorded at 5 minutes, whereas the addition of the BSA resulted in a temperature of 90°C at the same time point. The observed rise was consistent across setups, demonstrating a nearly twofold temperature increase in Cu100@BSA samples with the addition of BSA, emphasizing the correlation between thickness and temperature.

5.1.3 Computational Model for Aerogels

The third objective involved establishing a foundational computational model for aerogels. This model incorporated essential parameters, such as the fractal dimension and aerogel properties, to create a basis for future, more sophisticated simulations. The study aspired to furnish researchers with a tool that enabled precise representation and prediction of aerogel behaviors, thereby fostering innovative computational applications in the future. The complexities of aerogel behavior in computational simulations presented a prospect for further exploration and refinement in subsequent studies. Although this objective remained unfinished, it laid the groundwork for future exploration in establishing a practical model. This model, once completed, has the potential to serve as a valuable tool for computational studies, offering a theoretical foundation that complements experimental work. The tools and methodologies developed for this objective provided a robust framework for subsequent research endeavors aimed at achieving a comprehensive and realistic SA model.

5.2 Thesis Summary Statement

This thesis embarks on a systematic exploration with three distinct objectives, each contributing to the overarching goal of advancing our knowledge and capabilities in aerogel

research. Aligned with the broader objective of enhancing the understanding of Silica aerogels (SAs) and their multifaceted potential. In this study, hydrophilic SA samples were utilized to conduct a comprehensive investigation involving the deposition of 20 nm, 50 nm, and 100 nm of Copper (Cu) using magnetron sputtering. The objective was to examine the intricate interplay between the thin Cu film and the highly porous SA matrix. The resulting physical appearance of the Cu-sputtered thin film on the SAs appeared in shades of black and grey, influenced by surface plasmon resonance. Throughout this thesis work, it was affirmed that SA supports with deposited layers of metallic material via magnetron sputtering, are a new type of nanocomposite material that can contain different types of material at varying thicknesses on different surfaces of the SA.

5.3 Future Work

While this work sheds light on the unknowns associated with thin film deposition using magnetron sputtering techniques onto porous substrates such as Silica aerogels, there remains a gap in the field that necessitates further comprehensive investigations. Utilizing additional characterization techniques, such as atomic force microscopy, to study the topology of both BSAs and metallic-deposited composite aerogels can provide a better understanding of surface morphology. It is emphasized that this work recommends exploring different types of metals, such as gold, silver, tungsten, etc., and thoroughly characterizing their morphological, optical, and thermal properties. Cross-sectional SA supports with metallic thin films on their surfaces still necessitate further research and investigation. Although the EDS spectra analyzed in this study indicate the penetration of Cu into the SA, the precise quantity remains uncharted territory.

The thermal measurements, reflecting only a temperature increase with growing film thickness, rely on the provided emissivity from the IR camera rather than determining the actual emissivity, introducing a potential source of inaccuracy. Correcting these measurements

becomes crucial, and one approach is to determine the emissivity of the samples through further FTIR analysis post-initial thermal measurements. Although FTIR may not directly yield emissivity values, it can identify characteristic absorption bands and features relevant to emissivity upon analysis. Understanding the reflection and absorption spectra of the samples after thermal imaging is essential for leveraging silica aerogel supports with catalytic metal-oxide materials, particularly in applications like air and water purification.

To advance the understanding of these nanocomposites, a deeper exploration of the mechanisms of magnetron sputtering or experimentation with other forms of physical vapor deposition is proposed. This could involve developing a multidisciplinary optimization study considering crucial factors influencing the thin film deposition process, aiding in the penetration of deposited material into the SA nanostructure. Consideration should also be given to sample preparation and the strict monitoring of sample environments to understand the effects of ambient conditions on various samples sputtered with different metal or metal oxide materials. Lastly, while this work establishes a proof of concept, further experimental investigations in areas such as solar-driven water heating or air and water purification are suggested to pave the way for environmental remediation with nanocomposite aerogels created via SA supports with deposited material at the nanoscale. Given the environmentally benign and safer nature of magnetron sputtering, this method could potentially become a more popular avenue for creating such non-homogenous nanocomposite aerogels. This research aspires to contribute not only to the academic understanding of aerogels but also to the practical implementation of these materials in various technological industries.

Bibliography

- [1] Chin-Yun Lee et al. “Vapor Sublimation and Deposition to Fabricate a Porous Methyl Propiolate-Functionalized Poly-p-xylylene Material for Copper-Free Click Chemistry”. In: *Polymers* 13.5 (Mar. 4, 2021), p. 786. ISSN: 2073-4360. DOI: 10.3390/polym13050786. URL: <https://www.mdpi.com/2073-4360/13/5/786>.
- [2] Alexander I. Chernov et al. “Optical properties of silica aerogels with embedded multiwalled carbon nanotubes”. en. In: *physica status solidi (b)* 253.12 (Dec. 2016), pp. 2440–2445. ISSN: 0370-1972, 1521-3951. DOI: 10.1002/pssb.201600326. URL: <https://onlinelibrary.wiley.com/doi/10.1002/pssb.201600326>.
- [3] Gabrijela Horvat et al. “A Brief Evaluation of Pore Structure Determination for Bioaerogels”. In: *Gels* 8.7 (July 13, 2022), p. 438. ISSN: 2310-2861. DOI: 10.3390/gels8070438. URL: <https://www.mdpi.com/2310-2861/8/7/438>.
- [4] Peter M. Martin. *Handbook of deposition technologies for films and coatings: science, applications and technology*. 3rd ed. Amsterdam: Elsevier, 2010. ISBN: 978-0-8155-2031-3.
- [5] S. Alwin and X. Sahaya Shajan. “Aerogels: promising nanostructured materials for energy conversion and storage applications”. In: *Materials for Renewable and Sustainable Energy* 9.2 (July 2020), p. 7. ISSN: 2194-1459, 2194-1467. DOI: 10.1007/s40243-020-00168-4. URL: <http://link.springer.com/10.1007/s40243-020-00168-4>.
- [6] Michel A. Aegerter, Nicholas Leventis, and Matthias M. Koebel, eds. *Aerogels Handbook*. New York, NY: Springer New York, 2011. ISBN: 978-1-4419-7477-8. DOI: 10.1007/978-1-4419-7589-8. URL: <http://link.springer.com/10.1007/978-1-4419-7589-8>.
- [7] Hideaki Adachi and Kiyotaka Wasa. “Thin Films and Nanomaterials”. In: *Handbook of Sputtering Technology*. Elsevier, 2012, pp. 3–39. ISBN: 978-1-4377-3483-6. DOI:

- 10.1016/B978-1-4377-3483-6.00001-2. URL: <https://linkinghub.elsevier.com/retrieve/pii/B9781437734836000012>.
- [8] N. Serpone and A. V. Emeline. “Semiconductor Photocatalysis — Past, Present, and Future Outlook”. In: *The Journal of Physical Chemistry Letters* 3.5 (Mar. 1, 2012), pp. 673–677. ISSN: 1948-7185, 1948-7185. DOI: 10.1021/jz300071j. URL: <https://pubs.acs.org/doi/10.1021/jz300071j>.
- [9] Tânia Ferreira-Gonçalves et al. “Biological Thermal Performance of Organic and Inorganic Aerogels as Patches for Photothermal Therapy”. en. In: *Gels* 8.8 (Aug. 2022), p. 485. ISSN: 2310-2861. DOI: 10.3390/gels8080485. URL: <https://www.mdpi.com/2310-2861/8/8/485>.
- [10] Xinxin Liu et al. “Photothermal effect of infrared light to enhance solar catalytic hydrogen generation”. In: *Catalysis Communications* 102 (Dec. 2017), pp. 13–16. ISSN: 15667367. DOI: 10.1016/j.catcom.2017.08.014. URL: <https://linkinghub.elsevier.com/retrieve/pii/S156673671730345X>.
- [11] Yuan Zhao et al. “Photothermal Effect of Nanomaterials for Efficient Energy Applications”. In: *Novel Nanomaterials for Biomedical, Environmental and Energy Applications*. Elsevier, 2019, pp. 415–434. ISBN: 978-0-12-814497-8. DOI: 10.1016/B978-0-12-814497-8.00013-8. URL: <https://linkinghub.elsevier.com/retrieve/pii/B9780128144978000138>.
- [12] Elias Paiva Ferreira-Neto, Marcus Andre Worsley, and Ubirajara Pereira Rodrigues-Filho. “Towards thermally stable aerogel photocatalysts: TiCl₄-based sol-gel routes for the design of nanostructured silica-titania aerogel with high photocatalytic activity and outstanding thermal stability”. In: *Journal of Environmental Chemical Engineering* 7.5 (Oct. 2019), p. 103425. ISSN: 22133437. DOI: 10.1016/j.jece.2019.103425. URL: <https://linkinghub.elsevier.com/retrieve/pii/S2213343719305482>.
- [13] D. Amaranatha Reddy et al. “Self-assembled macro porous ZnS–graphene aerogels for photocatalytic degradation of contaminants in water”. In: *RSC Advances* 5.24 (2015), pp. 18342–18351. ISSN: 2046-2069. DOI: 10.1039/C4RA16494F. URL: <http://xlink.rsc.org/?DOI=C4RA16494F>.
- [14] Xia Shao et al. “Enhanced photocatalytic activity of TiO₂-C hybrid aerogels for methylene blue degradation”. In: *Scientific Reports* 3.1 (Oct. 22, 2013), p. 3018. ISSN: 2045-2322. DOI: 10.1038/srep03018. URL: <https://www.nature.com/articles/srep03018>.

- [15] Paola Franco et al. “Porous Aerogels and Adsorption of Pollutants from Water and Air: A Review”. In: *Molecules* 26.15 (July 23, 2021), p. 4440. ISSN: 1420-3049. DOI: 10.3390/molecules26154440. URL: <https://www.mdpi.com/1420-3049/26/15/4440>.
- [16] Maryam Hasanpour and Mohammad Hatami. “Photocatalytic performance of aerogels for organic dyes removal from wastewaters: Review study”. In: *Journal of Molecular Liquids* 309 (July 2020), p. 113094. ISSN: 01677322. DOI: 10.1016/j.molliq.2020.113094. URL: <https://linkinghub.elsevier.com/retrieve/pii/S0167732220308011>.
- [17] Yuan Zhao et al. “Photothermal Effect of Nanomaterials for Efficient Energy Applications”. In: *Novel Nanomaterials for Biomedical, Environmental and Energy Applications*. Elsevier, 2019, pp. 415–434. ISBN: 978-0-12-814497-8. DOI: 10.1016/B978-0-12-814497-8.00013-8. URL: <https://linkinghub.elsevier.com/retrieve/pii/B9780128144978000138>.
- [18] Sung Jun Kim, George Chase, and Sadhan C. Jana. “The role of mesopores in achieving high efficiency airborne nanoparticle filtration using aerogel monoliths”. In: *Separation and Purification Technology* 166 (June 2016), pp. 48–54. ISSN: 13835866. DOI: 10.1016/j.seppur.2016.04.017. URL: <https://linkinghub.elsevier.com/retrieve/pii/S1383586616301927>.
- [19] Changwook Kim et al. “Large-scale nanoporous metal-coated silica aerogels for high SERS effect improvement”. In: *Scientific Reports* 8.1 (Oct. 11, 2018), p. 15144. ISSN: 2045-2322. DOI: 10.1038/s41598-018-33539-z. URL: <https://www.nature.com/articles/s41598-018-33539-z>.
- [20] Sung Jun Kim, George Chase, and Sadhan C. Jana. “Polymer aerogels for efficient removal of airborne nanoparticles”. In: *Separation and Purification Technology* 156 (Dec. 2015), pp. 803–808. ISSN: 13835866. DOI: 10.1016/j.seppur.2015.11.005. URL: <https://linkinghub.elsevier.com/retrieve/pii/S1383586615303294>.
- [21] Devon T. McGrath et al. “Selective decontamination of the reactive air pollutant nitrous acid via node-linker cooperativity in a metal–organic framework”. In: *Chem. Sci.* 10 (21 2019), pp. 5576–5581. DOI: 10.1039/C9SC01357A. URL: <http://dx.doi.org/10.1039/C9SC01357A>.
- [22] Guangyao Li et al. “Superhydrophobic Surface-modified zeolite to regulate the migration of nonadsorbed liquid water in an Open-loop adsorption heat pump”. In: *Applied Thermal Engineering* 215 (Oct. 2022), p. 118929. ISSN: 13594311. DOI:

- 10.1016/j.applthermaleng.2022.118929. URL: <https://linkinghub.elsevier.com/retrieve/pii/S1359431122008687>.
- [23] Junggou Kwon et al. “Gas-Phase Nitrogen Doping of Monolithic TiO₂ Nanoparticle-Based Aerogels for Efficient Visible Light-Driven Photocatalytic H₂ Production”. In: *ACS Applied Materials & Interfaces* 13.45 (Nov. 17, 2021), pp. 53691–53701. ISSN: 1944-8244, 1944-8252. DOI: 10.1021/acsami.1c12579. URL: <https://pubs.acs.org/doi/10.1021/acsami.1c12579>.
- [24] Geula Dagan and Micha Tomkiewicz. “Titanium dioxide aerogels for photocatalytic decontamination of aquatic environments”. In: *The Journal of Physical Chemistry* 97.49 (Dec. 1993), pp. 12651–12655. ISSN: 0022-3654, 1541-5740. DOI: 10.1021/j100151a001. URL: <https://pubs.acs.org/doi/abs/10.1021/j100151a001>.
- [25] Hande Gunes et al. “A Remarkable Class of Nanocomposites: Aerogel Supported Bimetallic Nanoparticles”. In: *Frontiers in Materials* 7 (Feb. 6, 2020), p. 18. ISSN: 2296-8016. DOI: 10.3389/fmats.2020.00018. URL: <https://www.frontiersin.org/article/10.3389/fmats.2020.00018/full>.
- [26] Mingjia Zhi et al. “Synthesis and Photocatalysis of Metal Oxide Aerogels: A Review”. In: *Energy & Fuels* 36.19 (Oct. 6, 2022), pp. 11359–11379. ISSN: 0887-0624, 1520-5029. DOI: 10.1021/acs.energyfuels.2c01049. URL: <https://pubs.acs.org/doi/10.1021/acs.energyfuels.2c01049>.
- [27] Thokozane Justin Kunene et al. “Molecular Dynamics of Atomic Layer Deposition: Sticking Coefficient Investigation”. In: *Applied Sciences* 12.4 (Feb. 19, 2022), p. 2188. ISSN: 2076-3417. DOI: 10.3390/app12042188. URL: <https://www.mdpi.com/2076-3417/12/4/2188>.
- [28] Raul Zazpe et al. “Atomic Layer Deposition for Coating of High Aspect Ratio TiO₂ Nanotube Layers”. In: *Langmuir* 32.41 (Oct. 18, 2016), pp. 10551–10558. ISSN: 0743-7463, 1520-5827. DOI: 10.1021/acs.langmuir.6b03119. URL: <https://pubs.acs.org/doi/10.1021/acs.langmuir.6b03119>.
- [29] Se-Yong Park et al. “Fabrication of Highly Porous and Pure Zinc Oxide Films Using Modified DC Magnetron Sputtering and Post-Oxidation”. In: *Materials* 14.20 (Oct. 15, 2021), p. 6112. ISSN: 1996-1944. DOI: 10.3390/ma14206112. URL: <https://www.mdpi.com/1996-1944/14/20/6112>.
- [30] Hao Yuan et al. “4D Imaging of ZnO-Coated Nanoporous Al₂O₃ Aerogels by Chemically Sensitive Ptychographic Tomography: Implications for Designer Catalysts”. In: *ACS Applied Nano Materials* 4.1 (Jan. 22, 2021), pp. 621–632. ISSN: 2574-0970,

- 2574-0970. DOI: 10.1021/acsanm.0c02924. URL: <https://pubs.acs.org/doi/10.1021/acsanm.0c02924>.
- [31] László Péter Bakos et al. “Nitrogen doped carbon aerogel composites with TiO₂ and ZnO prepared by atomic layer deposition”. In: *Journal of Materials Chemistry C* 8.20 (2020), pp. 6891–6899. ISSN: 2050-7526, 2050-7534. DOI: 10.1039/C9TC05953A. URL: <http://xlink.rsc.org/?DOI=C9TC05953A>.
- [32] Laura Juhász et al. “False Morphology of Aerogels Caused by Gold Coating for SEM Imaging”. In: *Polymers* 13.4 (Feb. 16, 2021), p. 588. ISSN: 2073-4360. DOI: 10.3390/polym13040588. URL: <https://www.mdpi.com/2073-4360/13/4/588>.
- [33] Muralidhar Singh M et al. “Studies on Nanostructure Aluminium Thin Film Coatings Deposited using DC magnetron Sputtering Process”. In: *IOP Conference Series: Materials Science and Engineering* 149 (Sept. 2016), p. 012071. ISSN: 1757-8981, 1757-899X. DOI: 10.1088/1757-899X/149/1/012071. URL: <https://iopscience.iop.org/article/10.1088/1757-899X/149/1/012071>.
- [34] Dongge Ma et al. “Carbon Gels-Modified TiO₂: Promising Materials for Photocatalysis Applications”. In: *Materials* 13.7 (Apr. 8, 2020), p. 1734. ISSN: 1996-1944. DOI: 10.3390/ma13071734. URL: <https://www.mdpi.com/1996-1944/13/7/1734>.
- [35] Shuai Li et al. “Multifunction Hybrid Aerogel Capable of Reducing Silver Ions during Solar-Driven Interfacial Evaporation”. In: *ACS Sustainable Chemistry & Engineering* 10.23 (June 13, 2022), pp. 7463–7472. ISSN: 2168-0485, 2168-0485. DOI: 10.1021/acssuschemeng.1c08702. URL: <https://pubs.acs.org/doi/10.1021/acssuschemeng.1c08702>.
- [36] S. S. KISTLER. “Coherent Expanded Aerogels and Jellies”. In: *Nature* 127.3211 (May 1, 1931), pp. 741–741. ISSN: 1476-4687. DOI: 10.1038/127741a0. URL: <https://doi.org/10.1038/127741a0>.
- [37] Sun et al. “Multifunctional, Ultra-Flyweight, Synergistically Assembled Carbon Aerogels”. In: *Advanced Materials* 25.18 (May 14, 2013), pp. 2554–2560. ISSN: 0935-9648, 1521-4095. DOI: 10.1002/adma.201204576. URL: <https://onlinelibrary.wiley.com/doi/10.1002/adma.201204576>.
- [38] Ruben Baetens, Bjørn Petter Jelle, and Arild Gustavsen. “Aerogel insulation for building applications: A state-of-the-art review”. In: *Energy and Buildings* 43.4 (Apr. 2011), pp. 761–769. ISSN: 03787788. DOI: 10.1016/j.enbuild.2010.12.012. URL: <https://linkinghub.elsevier.com/retrieve/pii/S0378778810004329>.

- [39] H Li, S G Sunol, and A K Sunol. “Development of titanium-dioxide-based aerogel catalyst with tunable nanoporosity and photocatalytic activity”. In: *Nanotechnology* 23.29 (July 27, 2012), p. 294012. ISSN: 0957-4484, 1361-6528. DOI: 10.1088/0957-4484/23/29/294012. URL: <https://iopscience.iop.org/article/10.1088/0957-4484/23/29/294012>.
- [40] Ghafar et al. “Synchrotron Microtomography Reveals the Fine Three-Dimensional Porosity of Composite Polysaccharide Aerogels”. In: *Materials* 10.8 (July 28, 2017), p. 871. ISSN: 1996-1944. DOI: 10.3390/ma10080871. URL: <http://www.mdpi.com/1996-1944/10/8/871>.
- [41] Hongqiang Wang et al. “Enhanced Photothermal Conversion by Hot-Electron Effect in Ultrablack Carbon Aerogel for Solar Steam Generation”. In: *ACS Applied Materials & Interfaces* 11.45 (2019). PMID: 31631656, pp. 42057–42065. DOI: 10.1021/acsami.9b12918. eprint: <https://doi.org/10.1021/acsami.9b12918>. URL: <https://doi.org/10.1021/acsami.9b12918>.
- [42] *Precision Silica Aerogel Bar*. <http://www.buyaerogel.com/product/precision-silica-aerogel-bar/>.
- [43] Cinzia Buratti et al. “Aerogel glazing systems for building applications: A review”. In: *Energy and Buildings* 231 (2021), p. 110587. ISSN: 0378-7788. DOI: <https://doi.org/10.1016/j.enbuild.2020.110587>. URL: <https://www.sciencedirect.com/science/article/pii/S0378778820333739>.
- [44] D’Arienzo et al. “Synthesis and Characterization of Morphology-Controlled TiO₂ Nanocrystals”. In: *Studies in Surface Science and Catalysis*. Vol. 177. Dec. 2017, pp. 477–540. ISBN: 9780128050903. DOI: 10.1016/B978-0-12-805090-3.00013-9.
- [45] G. M. Pajonk et al. “Microstructural characterization of silica aerogels using scanning electron microscopy”. In: *Journal of Materials Science* 31.21 (1996), pp. 5683–5689. ISSN: 0022-2461, 1573-4803. DOI: 10.1007/BF01160815. URL: <http://link.springer.com/10.1007/BF01160815>.
- [46] R Rodriguez et al. “Fractal Characterization of Silica Sol Prepared by the Sol-Gel Method: From the Sol Formation to the Flocculation Process”. In: *Journal of Sol-Gel Science and Technology* 23 (July 2, 2001), pp. 99–105.
- [47] Dan Wen et al. “Gold Aerogels: Three-Dimensional Assembly of Nanoparticles and Their Use as Electrocatalytic Interfaces”. In: *ACS Nano* 10.2 (Feb. 23, 2016), pp. 2559–2567. ISSN: 1936-0851, 1936-086X. DOI: 10.1021/acsnano.5b07505. URL: <https://pubs.acs.org/doi/10.1021/acsnano.5b07505>.

- [48] Siris Laursen and Samiksha Poudyal. “Photo- and Electro-Catalysis”. In: Dec. 2015, pp. 233–268. ISBN: 9780444632593. DOI: 10.1016/B978-0-444-63259-3.00008-2.
- [49] István Lázár and Hanna Judit Szabó. “Prevention of the Aggregation of Nanoparticles during the Synthesis of Nanogold-Containing Silica Aerogels”. In: *Gels* 4.2 (2018). ISSN: 2310-2861. URL: <https://www.mdpi.com/2310-2861/4/2/55>.
- [50] R. Alan McCoy and Yuefan Deng. “Parallel Particle Simulations of Thin-Film Deposition”. In: *The International Journal of High Performance Computing Applications* 13.1 (1999), pp. 16–32. DOI: 10.1177/109434209901300102. URL: <https://doi.org/10.1177/109434209901300102>.
- [51] Arjan Bijlsma. “Characterizing copper nanoparticle DC sputtering with oxygen interference”. In: (Dec. 2011).
- [52] Vincent Le Houérou, Christian Gauthier, and Robert Schirrer. “Mechanical analysis of the blistering of a thin film deposited on a glassy polymer”. In: *Tribology International* 43.1 (2010), pp. 129–135. ISSN: 0301-679X. DOI: <https://doi.org/10.1016/j.triboint.2009.05.011>. URL: <https://www.sciencedirect.com/science/article/pii/S0301679X09001388>.
- [53] Peter Hatton et al. “Inert gas bubble formation in magnetron sputtered thin-film CdTe solar cells”. In: *Proceedings of the Royal Society A: Mathematical, Physical and Engineering Sciences* 476.2239 (July 2020), p. 20200056. ISSN: 1364-5021, 1471-2946. DOI: 10.1098/rspa.2020.0056. URL: <https://royalsocietypublishing.org/doi/10.1098/rspa.2020.0056>.
- [54] Handan Huang et al. “Controlling Film Thickness Distribution by Magnetron Sputtering with Rotation and Revolution”. In: *Coatings* 11.5 (May 19, 2021), p. 599. ISSN: 2079-6412. DOI: 10.3390/coatings11050599. URL: <https://www.mdpi.com/2079-6412/11/5/599>.
- [55] Iveta Tomcikova. “MODELING OF MAGNETIC FIELD DISTRIBUTION IN MAGNETOELASTIC FORCE SENSOR”. In: *Electromechanical and energy saving systems* 1 (Mar. 2018). DOI: 10.30929/2072-2052.2018.1.41.38-45.
- [56] Andrew H. Simon. “Sputter Processing”. In: *Handbook of Thin Film Deposition*. Elsevier, 2012, pp. 55–88. ISBN: 978-1-4377-7873-1. DOI: 10.1016/B978-1-4377-7873-1.00004-8. URL: <https://linkinghub.elsevier.com/retrieve/pii/B9781437778731000048>.
- [57] E. John Mahan. *Physical Vapor Deposition of Thin Films*. City: Wiley-VCH, 2000, p. 336. ISBN: 978-0471330011.

- [58] Alberto Pimpinelli, Levent Tumbek, and Adolf Winkler. “Scaling and Exponent Equalities in Island Nucleation: Novel Results and Application to Organic Films”. In: *The Journal of Physical Chemistry Letters* 5.6 (2014). PMID: 24660052, pp. 995–998. DOI: 10.1021/jz500282t. eprint: <https://doi.org/10.1021/jz500282t>. URL: <https://doi.org/10.1021/jz500282t>.
- [59] P. B. Barna and M. Adamik. “Fundamental structure forming phenomena of polycrystalline films and the structure zone models”. In: *Thin Solid Films* 317.1 (1998), pp. 27–33. ISSN: 0040-6090. DOI: [https://doi.org/10.1016/S0040-6090\(97\)00503-8](https://doi.org/10.1016/S0040-6090(97)00503-8). URL: <https://www.sciencedirect.com/science/article/pii/S0040609097005038>.
- [60] D. Depla et al. “Rotating cylindrical magnetron sputtering: Simulation of the reactive process”. In: *Journal of Applied Physics* 107.11 (June 2010), p. 113307. ISSN: 0021-8979, 1089-7550. DOI: 10.1063/1.3415550. URL: <http://aip.scitation.org/doi/10.1063/1.3415550>.
- [61] Tadayoshi Ono, Takahiro Kenmotsu, and Tetsuya Muramoto. “Simulation of the Sputtering Process”. In: *Reactive Sputter Deposition*. Ed. by Diederik Depla and Stijn Mahieu. Red. by Robert Hull et al. Vol. 109. Series Title: Springer Series in Materials Science. Berlin, Heidelberg: Springer Berlin Heidelberg, 2008, pp. 1–42. ISBN: 978-3-540-76662-9. DOI: 10.1007/978-3-540-76664-3_1. URL: http://link.springer.com/10.1007/978-3-540-76664-3_1.
- [62] Angstrom Engineering. *Facing Target / Low Damage Sputtering*. 2023. URL: <https://angstromengineering.com/tech/magnetron-sputtering/facing-target-low-damage-sputtering/>.
- [63] Yichen Zhang, Qingzhu Song, and Zhulai Sun. “Research on Thin Film Thickness Uniformity for Deposition of Rectangular Planar Sputtering Target”. In: *Physics Procedia* 32 (2012), pp. 903–913. ISSN: 18753892. DOI: 10.1016/j.phpro.2012.03.655. URL: <https://linkinghub.elsevier.com/retrieve/pii/S1875389212010723>.
- [64] Peter Panjan et al. “Review of Growth Defects in Thin Films Prepared by PVD Techniques”. In: *Coatings* 10.5 (2020). ISSN: 2079-6412. DOI: 10.3390/coatings10050447. URL: <https://www.mdpi.com/2079-6412/10/5/447>.
- [65] Hong-Ryul Kim and Hyung-Ho Park. “The Effect of Ar⁺ Ion Bombardment on SiO₂ Aerogel Film”. In: *Japanese Journal of Applied Physics* 37.12S (Dec. 1998), p. 6955. DOI: 10.1143/JJAP.37.6955. URL: <https://dx.doi.org/10.1143/JJAP.37.6955>.

- [66] Francisco Javier Jimenez. *Comprehensive Simulation of Sputter Deposition*. OCLC: 1019490824. Ottawa: Library and Archives Canada = Bibliothèque et Archives Canada, 2013. ISBN: 978-0-494-89218-3.
- [67] Abdelkader Bouazza and Abderrahmane Settaouti. “Understanding the contribution of energy and angular distribution in the morphology of thin films using Monte Carlo simulation”. In: *Monte Carlo Methods and Applications* 24.3 (Sept. 1, 2018), pp. 215–224. ISSN: 0929-9629, 1569-3961. DOI: 10.1515/mcma-2018-0019. URL: <https://www.degruyter.com/document/doi/10.1515/mcma-2018-0019/html>.
- [68] Ben Wang and Fu. “Simulation and Optimization of Film Thickness Uniformity in Physical Vapor Deposition”. In: *Coatings* 8.9 (Sept. 16, 2018), p. 325. ISSN: 2079-6412. DOI: 10.3390/coatings8090325. URL: <http://www.mdpi.com/2079-6412/8/9/325>.
- [69] M. P. Seah et al. “An accurate semi-empirical equation for sputtering yields I: for argon ions”. In: *Surface and Interface Analysis* 37.5 (May 2005), pp. 444–458. ISSN: 0142-2421, 1096-9918. DOI: 10.1002/sia.2032. URL: <https://onlinelibrary.wiley.com/doi/10.1002/sia.2032>.
- [70] M. P. Seah. “Universal Equation for Argon Gas Cluster Sputtering Yields”. In: *The Journal of Physical Chemistry C* 117.24 (June 20, 2013), pp. 12622–12632. ISSN: 1932-7447, 1932-7455. DOI: 10.1021/jp402684c. URL: <https://pubs.acs.org/doi/10.1021/jp402684c>.
- [71] S. Mahieu et al. “Monte Carlo simulation of the transport of atoms in DC magnetron sputtering”. In: *Nuclear Instruments and Methods in Physics Research Section B: Beam Interactions with Materials and Atoms* 243.2 (Feb. 2006), pp. 313–319. ISSN: 0168583X. DOI: 10.1016/j.nimb.2005.09.018. URL: <https://linkinghub.elsevier.com/retrieve/pii/S0168583X05017544>.
- [72] D. Depla and W.P. Leroy. “Magnetron sputter deposition as visualized by Monte Carlo modeling”. In: *Thin Solid Films* 520.20 (Aug. 2012), pp. 6337–6354. ISSN: 00406090. DOI: 10.1016/j.tsf.2012.06.032. URL: <https://linkinghub.elsevier.com/retrieve/pii/S0040609012007419>.
- [73] Dale W. Schaefer and Keith D. Keefer. “Structure of Random Porous Materials: Silica Aerogel”. In: *Physical Review Letters* 56.20 (May 19, 1986), pp. 2199–2202. ISSN: 0031-9007. DOI: 10.1103/PhysRevLett.56.2199. URL: <https://link.aps.org/doi/10.1103/PhysRevLett.56.2199>.

- [74] M. Freire-Gormaly et al. “Comparing Thresholding Techniques for Quantifying the Dual Porosity of Indiana Limestone and Pink Dolomite”. In: *Microporous and Mesoporous Materials* 207 (2015), pp. 84–89.
- [75] M. Freire-Gormaly. “The Pore Structure of Indiana Limestone and Pink Dolomite for the Modeling of Carbon Dioxide in Geologic Carbonate Rock Formations”. MASC. Thesis. 2013, p. 85.
- [76] M. Freire-Gormaly et al. “Pore Structure Characterization of Indiana Limestone and Pink Dolomite from Pore Network Reconstructions”. In: *Oil & Gas Science and Technology–Revue d’IFP Energies nouvelles* 71.3 (2016), pp. 33–46.
- [77] Rasul Abdusalamov et al. “Modeling and Simulation of the Aggregation and the Structural and Mechanical Properties of Silica Aerogels”. In: *The Journal of Physical Chemistry B* 125.7 (Feb. 25, 2021), pp. 1944–1950. ISSN: 1520-6106, 1520-5207. DOI: 10.1021/acs.jpcc.0c10311. URL: <https://pubs.acs.org/doi/10.1021/acs.jpcc.0c10311>.
- [78] S. Babu, J. C. Gimel, and T. Nicolai. “Diffusion limited cluster aggregation with irreversible slippery bonds”. In: *The European Physical Journal E* 27.3 (Nov. 2008), pp. 297–308. ISSN: 1292-8941, 1292-895X. DOI: 10.1140/epje/i2008-10381-8. URL: <http://link.springer.com/10.1140/epje/i2008-10381-8>.
- [79] Thierry Woignier et al. “Fractal Structure in Silica and Composites Aerogels”. In: *Gels* 7.1 (Dec. 26, 2020), p. 1. ISSN: 2310-2861. DOI: 10.3390/gels7010001. URL: <https://www.mdpi.com/2310-2861/7/1/1>.
- [80] Helmut Hermann and Antje Elsner. “Geometric Models for Isotropic Random Porous Media: A Review”. In: *Advances in Materials Science and Engineering* 2014 (2014), pp. 1–16. ISSN: 1687-8434, 1687-8442. DOI: 10.1155/2014/562874. URL: <http://www.hindawi.com/journals/amse/2014/562874/>.
- [81] Alexey V. Markin and Natalia E. Markina. “Experimenting with Plasmonic Copper Nanoparticles To Demonstrate Color Changes and Reactivity at the Nanoscale”. In: *Journal of Chemical Education* 96.7 (July 9, 2019), pp. 1438–1442. ISSN: 0021-9584, 1938-1328. DOI: 10.1021/acs.jchemed.8b01050. URL: <https://pubs.acs.org/doi/10.1021/acs.jchemed.8b01050>.
- [82] Shuai Chen et al. “Synthesis of Cu-Nanoparticle Hydrogel with Self-Healing and Photothermal Properties”. In: *ACS Applied Materials & Interfaces* 9.24 (June 21, 2017), pp. 20895–20903. ISSN: 1944-8244, 1944-8252. DOI: 10.1021/acsami.7b04956. URL: <https://pubs.acs.org/doi/10.1021/acsami.7b04956>.

- [83] George H. Chan et al. “Plasmonic Properties of Copper Nanoparticles Fabricated by Nanosphere Lithography”. In: *Nano Letters* 7.7 (July 1, 2007), pp. 1947–1952. ISSN: 1530-6984, 1530-6992. DOI: 10.1021/nl070648a. URL: <https://pubs.acs.org/doi/10.1021/nl070648a>.
- [84] Md Julkarnain et al. “Preparation and Properties of Chemically Reduced Cu and Ag Nanoparticles”. In: (Nov. 2013), pp. 636–640.
- [85] F Solá, F Hurwitz, and J Yang. “A new scanning electron microscopy approach to image aerogels at the nanoscale”. In: *Nanotechnology* 22.17 (Apr. 29, 2011), p. 175704. ISSN: 0957-4484, 1361-6528. DOI: 10.1088/0957-4484/22/17/175704. URL: <https://iopscience.iop.org/article/10.1088/0957-4484/22/17/175704>.
- [86] Nancy W. Stauffer. *Making a Remarkable Material Even Better*. Nov. 2019. URL: <https://energy.mit.edu/news/making-a-remarkable-material-even-better/>.
- [87] M. Freire-Gormaly and A. Bilton. “An Experimental System for Characterization of Membrane Fouling of Solar Photovoltaic Reverse Osmosis Systems under Intermittent Operation”. In: *Desalination and Water Treatment* 73 (2017), pp. 54–63.
- [88] M. Freire-Gormaly and A. Bilton. “Experimental Quantification of the Effect of Intermittent Operation on Membrane Performance of Solar Powered Reverse Osmosis Desalination Systems”. In: *Desalination* 435 (2018), pp. 188–197.
- [89] M. Freire-Gormaly and A. Bilton. “Impact of Intermittent Operation on Reverse Osmosis Membrane Fouling for Brackish Groundwater Desalination Systems”. In: *Journal of Membrane Science* 583 (2019), pp. 220–230.
- [90] M. Freire-Gormaly and A. Bilton. “Design of Solar Powered Reverse Osmosis Desalination Systems Considering Membrane Fouling caused by Intermittent Operation”. In: *Renewable Energy* 135 (2019), pp. 108–121.
- [91] M. R.* Snowdon et al. “Effects of Substituting Activated Carbon with Titanium-Dioxide-Coated Cenospheres in Conventional Aquarium Filters”. In: *Environments* 10.11 (Oct. 2023), p. 188.
- [92] M. Nagi. “Optothermal Characterization of Nanoparticle Infused Aerogels”. MSc. Thesis. Aug. 2023.
- [93] Rod Heu et al. “Target Material Selection for Sputter Coating of SEM Samples”. In: *Microscopy Today* 27.4 (July 2019), pp. 32–36. ISSN: 1551-9295, 2150-3583. DOI: 10.1017/S1551929519000610. URL: <https://academic.oup.com/mt/article/27/4/32/6813463>.

- [94] A. S. Kashin and V. P. Ananikov. “A SEM study of nanosized metal films and metal nanoparticles obtained by magnetron sputtering”. In: *Russian Chemical Bulletin* 60.12 (Dec. 2011), pp. 2602–2607. ISSN: 1066-5285, 1573-9171. DOI: 10.1007/s11172-011-0399-x. URL: <http://link.springer.com/10.1007/s11172-011-0399-x>.
- [95] Iulian Pana et al. “Optical Properties and Stability of Copper Thin Films for Transparent Thermal Heat Reflectors”. In: *Metals* 12.2 (Jan. 30, 2022), p. 262. ISSN: 2075-4701. DOI: 10.3390/met12020262. URL: <https://www.mdpi.com/2075-4701/12/2/262>.
- [96] K. Kamiuto, S. Saitoh, and Y. Tokita. “Scattering phase function of a silica aerogel at 450 nm wavelength”. In: *Journal of Quantitative Spectroscopy and Radiative Transfer* 50.3 (1993), pp. 293–299. ISSN: 0022-4073. DOI: [https://doi.org/10.1016/0022-4073\(93\)90079-W](https://doi.org/10.1016/0022-4073(93)90079-W). URL: <https://www.sciencedirect.com/science/article/pii/S002240739390079W>.
- [97] Jun-Jie Zhao et al. “Optical and radiative properties of infrared opacifier particles loaded in silica aerogels for high temperature thermal insulation”. en. In: *International Journal of Thermal Sciences* 70 (Aug. 2013), pp. 54–64. ISSN: 12900729. DOI: 10.1016/j.ijthermalsci.2013.03.020. URL: <https://linkinghub.elsevier.com/retrieve/pii/S1290072913000641>.
- [98] Barbara Mojet, Sune Ebbesen, and Leon Lefferts. “ChemInform Abstract: Light at the Interface: The Potential of Attenuated Total Reflection Infrared Spectroscopy for Understanding Heterogeneous Catalysis in Water”. In: *Chemical Society reviews* 39 (Dec. 2010), pp. 4643–55. DOI: 10.1039/c0cs00014k.
- [99] Thanh Tran et al. “Synthesis of amorphous silica and sulfonic acid functionalized silica used as reinforced phase for polymer electrolyte membrane”. In: *Adv. Nat. Sci.: Nanosci. Nanotechnol.* 4 (Dec. 2013), p. 045007. DOI: 10.1088/2043-6262/4/4/045007.

Appendix

A. Langevin & Brownian Motion

The Matlab script provided in the section below first generates initial random positions and radii for the particles, then repeatedly selects a random particle and updates its position and radius according to the Langevin equation and the growth rate. The new position of the particle is also checked against the positions of the other particles and the boundaries of the cube to ensure that it is not too close to other particles or out of bounds. The Langevin equation is a stochastic differential equation that describes the motion of a particle under the influence of random forces.

$$dx = F(x, t)dt + \sqrt{2D}dW \quad (\text{A.1})$$

Where x is the position of the particle, t is the time, $F(x, t)$ is the deterministic force acting on the particle, D is the diffusion constant, and dW is a random Wiener process. The Wiener process represents the random forces acting on the particle, and the square root of $2D$ is the amplitude of the random forces, known as the Langevin force. Additionally, the equation can be altered to include thermal fluctuations, collisions with other particles or molecules, and other sources of randomness. The standard, most general class of stochastic differential equations (SDEs) is seen in the equations provided below.

$$\frac{dx(t)}{dt} = F(x(t)) + \sum_{a=1}^n g_a(x(t))\xi^a(t) \quad (\text{A.2})$$

In mathematics, the Langevin equations of motion for the Brownian particle motion are as

follows.

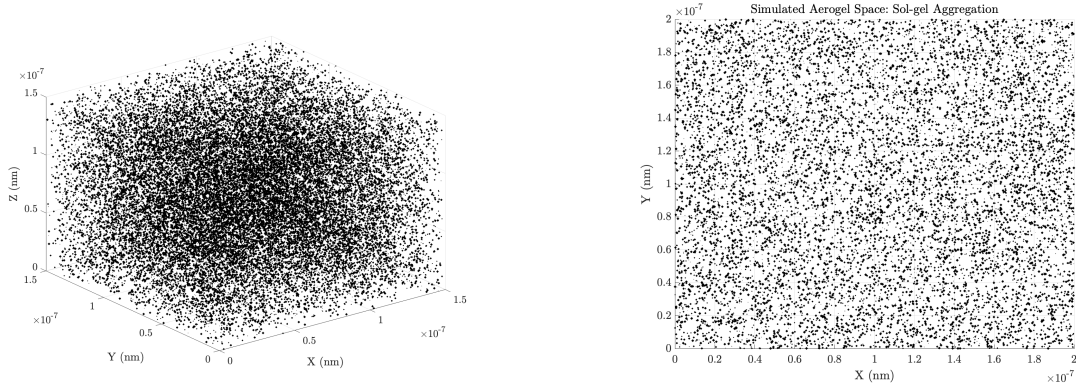
$$\frac{dx(t)}{dt} = v(t) \quad (\text{A.3})$$

$$\frac{dv(t)}{dt} = -\frac{\gamma}{m}v(t) + \frac{1}{m}\xi(t) \quad (\text{A.4})$$

Where the random force, $\xi(t)$, is a stochastic variable giving the effect of background noise due to the fluid on the Brownian particle. In many scenarios, this force is neglected to attain familiar solutions, however, here the force is not neglected, and Equation A.4 is derived.

$$F_d = \frac{1}{2}\rho v^2 C_d A \quad (\text{A.5})$$

In the Matlab code developed in this thesis work, the Langevin equation is used to update the position of the particle in each iteration of the DLCA algorithm. The deterministic force acting on the particle is the drag force (F_d), which is calculated using the drag coefficient (C_d), the viscosity of the solvent, and the particle radius. The random force is the thermal fluctuations, which are calculated using the temperature and the Boltzmann constant.



(a) Generated pore space in 3D of SA nanostructure.

(b) XY-slice from generated nanostructure of SA.

Figure A.1: 3D (a) and 2D (b) DLCA simulation results, which are used to simulate the sol-gel mechanisms of creating a silica aerogel.

B. Matlab Simulation: Sol-gel Aggregation

```
% Define parameters
num_particles = 10000; % Number of particles
min_radius = 5e-9; % Minimum radius of each particle (in m)
max_radius = 200e-9; % Maximum radius of each particle (in m)
particle_spacing = 0.2e-6; % Spacing between particles (in m)
iteration_number = 1500; % Number of iterations to run the DLCA
    algorithm
growth_rate = 1e-17; % Base growth rate of the particles (in m/
    s)
cube_size = 1e-6; % Size of the cube
concentration = 1.5; % Particle concentration
fractal_dimension = 2.4; % Fractal dimension parameter
boltzmann_constant = 1.38064852e-23; % Boltzmann constant (J/K)
temperature = 300; % Temperature (K)
particle_shape = 1; % Particle shape factor
particle_density = 2e3; % Particle density (kg/m^3)
viscosity = 1e-3; % Viscosity of the solvent (Pa*s)
mean_pore_diameter = 20e-9; % Mean pore diameter (in m)

% Generate initial particle positions and radii
particle_positions = zeros(num_particles, 3); % Initialize
    matrix to store particle positions
particle_radii = (max_radius - min_radius).*rand(num_particles
    ,1) + min_radius; % Generate random radii
for i = 1:num_particles
    particle_positions(i, :) = [rand()*particle_spacing, rand()
        *particle_spacing, rand()*particle_spacing]; % Generate
        random positions
end

% Run DLCA to generate final particle positions
for i = 1:iteration_number
```

```

particle_index = randi(num_particles); % Select a random
particle
% Scale the growth rate by the fractal dimension and mean
pore diameter
scaled_growth_rate = growth_rate * particle_radii(
particle_index)^(2-fractal_dimension) * (particle_radii(
particle_index) / mean_pore_diameter);
% Calculate the drag coefficient
drag_coefficient = 6*pi*viscosity*particle_radii(
particle_index)*particle_shape;
mass = (4/3)*pi*(particle_radii(particle_index)^3)*
particle_density;
dt = 0.001; % time step

% Update the position of the particle using the Langevin
equation
d_x = (-drag_coefficient/mass)*particle_positions(
particle_index,:)*dt + sqrt((2*boltzmann_constant*
temperature*dt)/mass)*randn(1,3);
new_position = particle_positions(particle_index,:) + d_x;
particle_radii(particle_index) = particle_radii(
particle_index) + scaled_growth_rate*dt*i*concentration;
% Check if the new position is far enough from other
particles and is within the bounding box
distance = pdist2(new_position, particle_positions) -
particle_radii(particle_index) - particle_radii;

if min(distance) <= 2*particle_radii(particle_index)
% do not update the position or radius of the particle
else
if all(new_position > 0) && all(new_position <
cube_size)
particle_positions(particle_index,:) = new_position;
particle_radii(particle_index) = particle_radii(

```

```

        particle_index) + growth_rate*i*concentration;
    end
end
end

% Create a binary 3D matrix of the particles
cube = zeros(round(cube_size*1e9), round(cube_size*1e9),round(
    cube_size*1e9));
for i = 1:num_particles
    x_center = particle_positions(i, 1)*1e9;
    y_center = particle_positions(i, 2)*1e9;
    z_center = particle_positions(i, 3)*1e9;
    x_min = max(round(x_center - particle_radii(i)*1e9),1);
    x_max = min(round(x_center + particle_radii(i)*1e9),size(
        cube,1));
    y_min = max(round(y_center - particle_radii(i)*1e9),1);
    y_max = min(round(y_center + particle_radii(i)*1e9),size(
        cube,2));
    z_min = max(round(z_center - particle_radii(i)*1e9),1);
    z_max = min(round(z_center + particle_radii(i)*1e9),size(
        cube,3));
    cube(x_min:x_max, y_min:y_max, z_min:z_max) = 1;
end

% Calculate the porosity
porosity = sum(cube(:)==0) / numel(cube);
disp(porosity);

figure(1);
scatter3(particle_positions(:,1), particle_positions(:,2),
    particle_positions(:,3), particle_radii*1e9, '.', 'k');
xlabel('X (nm)');
ylabel('Y (nm)');
zlabel('Z (nm)');

```

```
title('Simulated Aerogel Space: Sol-gel Aggregation');  
set(gca, 'FontName', 'CMU Serif', 'FontSize', 14);
```